Real–Time Imaging of Decimetre–Resolution 3D Seismic Volumes

Mark E. Vardy

School of Ocean and Earth Science

University of Southampton

A thesis submitted for the degree of

Doctor of Philosophy

July 2009

To my loving parents.

University of Southampton

Abstract

Faculty of Engineering, Science and Mathematics
School of Ocean and Earth Science

Doctor of Philosophy

Real–Time Imaging of Decimetre–Resolution 3D Seismic Volumes

by Mark E. Vardy

The 3D Chirp sub–bottom profiler acquires a true 3D seismic volume with decimetric horizontal and centimetric vertical resolutions, providing an ideal platform for shallow–water engineering, archaeology, military, and geological studies. In this thesis, I show how simple processing flows built around a combination of standard Chirp/Vibroseis techniques and well known industry methods produce effective and impressive results by considering an object identification case study in a shallow–water, harbour setting (Vardy et al., 2008). Both stacked and migrated volumes are used to identify 89 individual buried targets that are correlated with coincident objects. Through subsequent dredging, a 100 % detection success is demonstrated, along with the strong similarity between the migrated reflector morphology and co–incident object shape. However, this processing approach requires extensive manual input and very long processing times ($\geq$ 1 month).

For this reason, a new method for pre–stack 3D Kirchhoff imaging is developed. Correlation with a series of bandwidth limited theoretical source sweeps is used to frequency decompose the raw traces for pre–stack time migration using a constant velocity. By accommodating dispersion through imaging a series of band limited traces, rather than through Fourier Transform, processing times are reduced from $\geq$ 1 month to c. two days for the object detection volume (i.e., approaching real–time application). The effectiveness of this new algorithm is examined using several synthetic volumes, allowing the degenerative effects of gaps in the fold to be explored. Finally, the application of the 3D Chirp system to geological cases is demonstrated through the geomorphological mapping of a sequence of mass movement events in Windermere, UK Lake District. Three mass movement deposits are identified in a 100 m by 400 m survey area. Through mapping of the package distributions and their interaction with the pre–existing sediments stratigraphy, they are identified as Younger Dryas climate amelioration deposits, resulting from the rapid deposition of gravitationally unstable, unconsolidated sediments. A metre–scale structural interpretation allows the depositional regimes (two being debris flow and the third a mass flow deposit) and dominant transport directions to be inferred.

Contents

List of Figures

List of Tables

Mathematical Nomenclature

Co–ordinate Systems

x, y, z	Trace mid–point location.
X, Y, Z	3D Chirp mat location.
x', y', z'	Location of a point on the mat measured relative to the RTK–GPS antenna.
$X_{COG}, Y_{COG}, Z_{COG}$	Location for centre–of–gravity of 3D Chirp mat.
$\mathbf{c}, \mathbf{b}, \mathbf{k}$	Unit vectors for 3D Chirp array position relative to (x', y', z').
x_s, y_s, z_s	Source array location.
x_g, y_g, z_g	Receiver group location.
$x1, x2, t$	Location in migration aperture.
x_ξ, y_ξ, z_ξ	Location in image space.
x_{ZO}, y_{ZO}, t_{ZO}	Zero–offset location and time for DMO.

Migration Parameters

$p(x, y, z, t)$	Pre–migrated wavefield in Cartesian co–ordinates.
$p(r, t)$	Pre–migrated wavefield in spherical polar co–ordin––ates.
$P(k_x, k_y, k_z, \omega)$	Pre–migrated wavefield after Fourier transform.
$I(x_\xi, y_\xi, z_\xi, t_\xi)$	Post–migrated image.
$W(x, y, z, t)$	Weight function for trace amplitudes during migration.
$H(x, y, z, t)$	Pre–migrated wavefield after Hilbert transform.
G	Greens function for calculating wavefront area.
$\mathbf{G}_s, \mathbf{G}_g$	Source and receiver Greens function amplitudes.
h	Source–receiver offset.
h_s, h_g	Source–to–image location offset, and receiver–to–image location offset.
β	Azimuth of source–receiver pair.
ϕ	Angle between input and output offset vectors during AMO.

A	Migration aperture.
ω_C	Central frequency of band limited trace.
N_ω	Number of band limited traces.
$\Delta\boldsymbol{\tau}_G$	Wavefield directional vector at surface.

Miscellaneous Parameters

M	Number of shots.
N	Number of time samples.
t	Time.
t'	Retardation time; time of wavefield in downward continued reference frame.
t_N	Time after NMO correction.
Δt	Temporal sampling interval .
$\Delta x, \Delta y, \Delta z$	Spatial sampling intervals.
f	Frequency.
ω	Angular frequency.
k	Spatial wavenumber.
f_N, ω_N, k_N	Nyquist limits.
f_{band}	Frequency bandwidth.
s	Amplitude for individual time sample on trace.
S	Amplitude for individual frequency on trace after Fourier transform.
v	Velocity of wavefield host medium.
v_N	Velocity for NMO correction.
c	Half velocity.
ρ	Density of wavefield host medium.
κ	Bulk modulus of host medium.
$\mathbf{u}$	Host medium displacement vector.
θ	Dip angle of wavefront or reflector (they are equivalent).
d	Dip gradient of wavefront or reflector.
RI	Repeatability Index.
$\phi(\tau)$	Cross–correlated value at time τ.
σ	Standard deviation.
Q	Quality factor of RTK–GPS string.
$LPME$	Line of Position Mean Error for RTK–GPS string.

Glossary of Terms

Aliasing:

Data	Aliasing due to undersampling in the acquisition space.
Image	Aliasing due to undersampling in image space.
Operator	Aliasing due to undersampling of the imaging operator.
Amelioration	Climatic improvement (warming) from stadial to interstadial conditions.
AMO	Azimuthal Move–Out.
API	Application Program Interface, used to call specific library functions during programming.
AUV	Autonomous Underwater Vehicle.
Bandwidth	Theoretical frequency bandwidth of the sweep. For the broadband Chirp sweeps this is -13.0 – 13.0 kHz.
BIIS	British and Irish Ice Sheet.
Chirp	Marine seismic source emitting a frequency modulated source waveform several ms in length.
CMP	Common Mid–Point between source and receiver.
CRP	Common Reflection Point.
D–GPS	Differential GPS.
Devensian	Also called Weichselian. Quaternary time period running between 116 ka BP and 11.5 ka BP. Normally divided into Early (116 – 58 ka BP), Mid (58 – 31 ka BP), and Late (31 – 11.5 ka BP).
DMO	Dip Move–Out.
Effective Bandwidth	The -3dB (or half–power) bandwidth of the source sweep. For the broadband Chirp sweeps this is 10.0 kHz (2.0–12.0 kHz).

Footprint	Common mid–points sampled by single shot.
Fresnel Zone	The area of a reflector from which energy can reach the hyrdophones within $\lambda/2$ of the first reflected energy. During migration, traces within this area dominate the amplitude reconstruction of the imaged trace.
FPGA	Field–Programmable Gate Array logic.
GPS	Geographical position system.
ISVR	Institute of Sound and Vibration research, University of Southampton.
Klauder Wavelet	Auto–correlated wavelet of Chirp sweep.
LGM	Last Glacial Maximum.
LLR	Loch Lomond Readvance (contemporaneous with Younger Dryas).
MCS	Multi–Channel Seismic.
Migration:	
Pre–Stack	Migration before NMO and stack, using the true source and receiver locations.
Post–Stack	Migration after NMO and stack, using the CMP bin centre co–ordinates.
NMO	Normal Move–Out.
PPS	Pulses Per Second.
RTK–GPS	Real Time Kinematic GPS.
S/N	Signal–to–Noise ratio.
SSS	Seismic Sequence Stratigraphy (notation after Eyles and Mullins (1997)).
STFT	Discrete–time Short–Time Fourier Transform.
TVG	Time varying gain.
TWT	Two–Way Traveltime.
Vibroseis	Land seismic source emitting a frequency modulated source waveform several seconds in length.
WKBJ	Wentzel–Kramers–Brillouin–Jeffreys approximation for the solution of the wavefield.
YD	Younger Dryas period of ice re–advance (11.55 – 12.80 ka BP).

Acknowledgements

"*You can't wait for inspiration. You have to go after it with a club.*"

Jack London (1876–1916)

I believe it is customary to start by thanking those who have contributed most towards this work. So, I'll start with my left and right hands, without whom it would have been impossible to type a document so littered by miss–spellings and grammatical errors (my toes are not nearly so dextrous). Next must come my supervisors: Jon Bull; Justin Dix; and Tim Henstock (in no particular order, so no fighting). Their advise and timely support has always been there when required, and without them I would never have made it through this far. I thank you all, and look forward to working with you more. I must also acknowledge the large contribution made by GeoAcoustics Ltd, particularly: Martin Gutwoski; David Stone; Peter Hogarth; and Tom Hiller. Without their support (both financial and practical) this project would have never taken place.

My family. Not just for the last four years, but also the twenty–two before that. Without your support and encouragement it would not have been possible for me pursue my dreams and to get anywhere near this far. You know I love you, and you know how much all the help means to me.

Then there are the fellow students who have help me (either with advise or simply through listening to my random theorising) during the course of this work. Luke Pinson, Tesmi Jose, Pierre Cazenave, Suzanne MacLachlan, Rebecca Bell, Kirsty Edgar, Bethan Jones, Rich Marsh, John Dinley, Charlie Thompson, Gawen Trathen, and Ruth Plets, have all proved to be able listeners and placaters. Extra thanks must go to Suzie, who somehow manage to survive proof reading most of this document – you're a star! Similarly, Chris Jeffery, Christina Perryman, Peter Comber, Katy Fry, and Dan Summons for having the guts to live with me and put up with my idiosyncrasies. A special mention should also probably go to Lorna McLean and Kat Cox, without whose combined biscuit devouring abilities I would undoubtedly be several stone heavier. Finally I would like to thank all the Post–Grads at NOC with whom I have shared the highs and lows of the last three and a half years. It has been a pleasure (almost).

Declaration of Authorship

I, **Mark E. Vardy**, declare that this thesis and the work presented in it are my own and has been generated by me as the result of my own original research.

Real–Time Imaging of Decimetre–Resolution 3D Seismic Volumes

I confirm that:

1. This work was done wholly or mainly while in candidature for a research degree at this University;
2. Where any part of this thesis has previously been submitted for a degree or any other qualification at this University or any other institution, this has been clearly stated;
3. Where I have consulted the published work of others, this is always clearly attributed;
4. Where I have quoted from the work of others, the source is always given. With the exception of such quotations, this thesis is entirely my own work;
5. I have acknowledged all main sources of help;
6. Where the thesis is based on work done by myself jointly with others, I have made clear exactly what was done by others and what I have contributed myself;
7. Either none of this work has been published before submission, or parts of this work have been published as:

   Decimeter Resolution 3D Seismic Volume in Shallow Water: A Case Study in Small Object Detection, Vardy, Dix, Henstock, Bull, and Gutowski, **Geophysics**, 73(2), B33-B40, 2008.

Signed:

Dated:

"...It ought to be possible, with present refinements in physical apparatus and their use, to construct an instrument what would record the reflections of Earth waves started at the surface, as they encounter such a well–marked plane of difference in hardness and elasticity as that separating the Bend and Ellenberger formations (in north–central Texas)..."

J.A. Udden (1859–1932)

1

Introduction

Sound is a disturbance of the mechanical energy within a system, propagating as waves of alternating pressure that cause localised regions of compression and rarefaction. As such, the propagation of sound is dependant upon the elastic properties of the host medium.

With the development of elastic theory in the 17^{th} and 18^{th} Centuries, experimentalists such as Mallet (1848, 1851), Mallet and Mallet (1859), Rayleigh (1885), Stoneley (1924), and Love (1927), were able to investigate the elastic properties of the Earth. While these early experiments looked at the gross properties of the Earth using surface or refracted waves, it was not until the 1920s that people such as J.A. Udden considered the idea of using reflections from discrete impedance boundaries to map subsurface structures (Sheriff, 1988). In 1921, William P. Haseman, J. Clarence Karcher, Irving Perrine, and Daniel W. Ohern, used a dynamite charge with an early seismograph to collect the first seismic reflection profile by recording reflections from a buried stratigraphic interface in the Vines Branch area

of south–central Oklahoma (Dragoset, 2005).

Seismic imaging is ultimately constrained by the acquisition geometry, and early experiments, such as Vines Branch, suffered from the small number of recording channels causing low signal–to–noise (S/N) ratios. Even when technological advancements permitted multi–receiver arrays, it was not until the advent of digital field systems in the 1960s that seismic reflection imaging became a truly useful tool (Sheriff, 1988). The increased computational power allowed the use of statistically developed filters to clean the recorded wavelets (Wiener, 1950), and geographically coincident traces to be stacked at common mid–points (CMP – originally CRP, Common Reflection Point) (Mayne, 1962).

The very early experiments, such as Vines Branch, although not 3D in the true sense of the word, were acquired in such a manner as to enable the application of 3D processing techniques (referred to as Dip Shooting). However, with the increasing number of channels, and therefore better raw S/N ratios, interpreters moved to using continuous sections rather than an individual cross–spread of geophones for each shot (Sheriff, 1988). While 2D data acquired in this manner is limited to only along–track dips and therefore can only migrate energy correctly in the along–track direction, 3D data volumes contain dipping information for all azimuths. This enables dipping events to be correctly imaged regardless of acquisition direction, and the complex diffraction hyperbolae formed around point sources to be collapsed back to their true location, with the additional benefit of increased S/N.

The early development of 3D seismic acquisition is shrouded in a thick corporate veil; Dragoset (2005) attributes the first 3D survey to Exxon, in 1967, while the first published trial took place at Bell Lake Field, Lea County, New Mexico, in 1972 (Schneider, 1998, 2001). Today, however, 3D surveys have become the norm, particularly in the marine environment, where the first recorded survey was in the North Sea, in 1975 (Davies et al., 2004). Survey ships are capable of towing up to 16 streamers > 10 km in length, providing multi–azimuth

coverage of 1 km wide swaths (Cartwright and Huuse, 2005). The cost–productivity ratio has decreased to such a level that large–scale 2D acquisition, even for reconnaissance surveys, is almost resigned to the history books. It is not uncommon to cover areas $> 10,000$ km^2 in a single survey, while, in the North Sea, a number of smaller volumes have been combined to provide complete 3D coverage over an area in excess of 100,000 km^2 (Edwards, 2005).

1.1 High–Resolution 3D Seismic Detectors

The proliferation of 3D seismic data acquisition on basin–scale surveys has had an enormous impact on our understanding of large–scale tectonics (e.g., Cartwright and Huuse, 2005). For example, fault networks, their linkages and growth patterns (e.g., Rowan et al., 1998), igneous systems (e.g. Planke et al., 2000), and fluid–rock interactions such as blow–out pipes (e.g., Loseth et al., 2001), have all benefited greatly from mapping/imaging in 3D.

However, these systems use sources with a frequency content in the in the 5 Hz to 50 Hz region, and CMP bin spacing of tens to hundreds metres. This provides the several kilometres penetration necessary for petroleum exploration, but at tens metres vertical and several hundred metre horizontal resolution. There have been several attempts to transfer these principles into the shallow–water environment (summarised in Table 1.1), where a frequency content of several kHz, and receiver spacing of tens cm is required to provide the decametre penetration with decimetre vertical and horizontal resolutions. These systems are reviewed in this section:

1.1.1 SEISCAT/Opus3D

The first successful high–resolution 3D seismic system was developed at the Renard Centre of Marine Geology, University of Gent (Henriet

System	Source	No. Receivers	Bin Size (m)	References
SEISCAT	15 in^3 Watergun or Boomer	24	1.0	Henriet et al. (1992) Versteeg et al. (1992) Marsset et al. (1998)
Opus3D	Boomer (1 – 3 kHz)	16	1.0	Marsset (2000) Missiaen et al. (2002) Muller et al. (2002) Missiaen (2005)
BOSS	6 Chirp Transducers (5.0 – 23.0 kHz)	32	-	Schock et al. (2001)
3D Chirp	4 Chirp Transducers (1.5 – 13.0 kHz)	60	0.125	Gutowski et al. (2002) Bull et al. (2005) Gutowski et al. (2008) Vardy et al. (2008)
BOSS (AUV)	Chirp Transducers (2.0 – 12.0 kHz)	252	-	Schock and Wulf (2003)
3D VHR	Airgun (0.4–0.65 kHz)	72	1.25 (inline) 3.73 (xline)	Scheidhauer et al. (2003) Scheidhauer et al. (2005) Hammami and Marillier (2007)
SEAMAP-3D	Boomer (1.0–3.0 kHz)	16	0.25	Muller et al. (2007)

Table 1.1: Summary of past and present high–resolution 3D seismic systems, listed in approximate chronological order.

et al., 1992; Versteeg et al., 1992; Marsset et al., 1998). Designed as a simple down–scaling of industry techniques, SEISCAT was composed of 12 dual channel streamers deployed behind a specially modified catamaran, and acquired data at a 1.0 m bin spacing using either a 15 cubic–inch watergun or boomer source.

Similarly, source–receiver positioning was accomplished using techniques garnered from industry: laser ranging between a Differential–GPS (D–GPS) base station and a catamaran mounted prism provided source X/Y location; first arrival travel–time picks an estimate of the source–receiver offset; while vertical variations could be accommodated through swell filtering in post–processing. However, wind, waves, and currents, particularly in offshore environments, caused the flexible streamer alignments to become unstable, dramatically increas-

ing errors in receiver positioning. This made absolute positioning of each source–receiver pair very difficult, if not impossible, and led to considerable horizontal and vertical smearing in the stacked volume (Marsset et al., 1998). There are no published values for these errors, but one can expect them to be of the order of several 10s cm in very good conditions, extending to > 1.0 m in areas with a strong current and/or swell (i.e., of the order of CMP bin size).

With the addition of an EU grant (MAS3–CT97–0121), groups at the University of Gent and Ifremer built on lessons learned with the SEISCAT proto–type and developed the Opus3D system. Two 6 m long inflatable wings extend out either side of a central 6 m long RIB to deploy eight dual channel streamers, providing a 16 channel sample of the reflected wavefields at 16 kHz sample rate and 1.0 m by 1.0 m horizontal resolution (Missiaen et al., 2002). The whole streamer/wing design is modular, making the inline and cross–line array size adjustable, and allowing the receiver spacing to be varied depending on water depth (Missiaen, 2005).

Theoretical positions for each source/receiver pair are calculated using a Real Time Kinematic GPS (RTK-GPS) antenna mounted on the boomer catamaran and assuming a static geometry. However, as with SEISCAT, the Opus3D system relies heavily on post–processing techniques to remove swell and tidal artefacts (Missiaen, 2005). Inversion of inline consistent vertical anomalies in the first arrival has been used to isolate tidal and swell effects by making the simplifying assumption of a flat seabed within a single acquisition footprint (Wardell et al., 2002). Such a methodology effectively corrects vertical variations, producing dramatic improvements in the quality of the final stack, but cannot accommodate lateral variations. Thereby, the theoretical horizontal resolution post–migration is limited to a complex relationship between the sea state and seabed roughness, rather than half the dominant source wavelength (as would be the case for a perfectly corrected migrated data volume).

1.1.2 BOSS/BOSS AUV

The first iteration of the BOSS (Buried Object Scanning Sonar) system, designed and built jointly by Florida Atlantic University and The Office of Naval Research, consisted of 32 hydrophones arranged in a four row, eight column grid around a six element frequency modulated (Chirp) source array (Schock et al., 2001). Positioning came from a 3–axis motion sensor which allowed the receiver positions to be calculated relative to each source location. This resulted in data being acquired as along–track slices rather than geographically orientated volumes, limiting the absolute positioning of observed targets to triangulation against objects of known location.

The next generation BOSS system (Schock and Wulf, 2003) has been expanded to be capable of both towed deployment, and Autonomous Underwater Vehicle (AUV) mounting. Comprising a 1.5 m diameter disk of 252 hydrophones arranged around a central spherical source, the reflected waveforms are recorded at a sampling rate of 48 kHz. Positioning is still via a motion sensor, meaning that data volumes remain limited to non–geographically referenced 1.5 m wide along–track sections. However, additional multi–aspect processing affords greater resolution within these inline sections (Schock et al., 2005).

A dynamically growing voxel volume of returns is populated with an extra cross–line row of data after each pulse. These new data are generated using the following equation:

$$I(x, y, z, m_2) = \frac{1}{NM} \sum_{n=1}^{N} \sum_{m=m_2-M+1}^{m_2} s_{n,m}(t_{TFn}) R_{TFm} R_{Fn,m}; \quad (1.1)$$

where $I(x, y, z, m_2)$ is the voxel amplitude for location (x, y, z) and shot m_2 calculated over N hydrophones and M shots, while $s_{n,m}(t_{TFn})$ is the recorded signal at hydrophone n for the sample time (t_{TFn}) associated with the path from the source to location (x, y, z), R_{TFm}, and receiver to location (x, y, z), $R_{Fn,m}$.

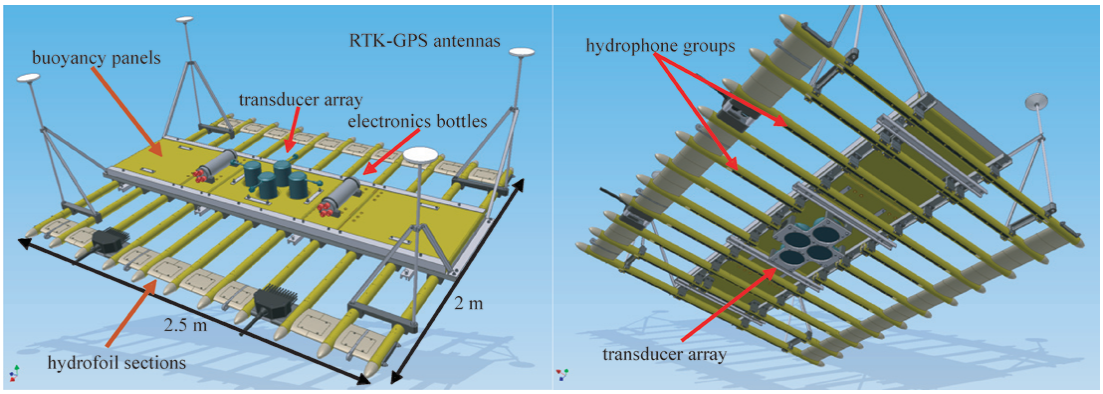

Figure 1.1: Engineering drawing showing top, a), and bottom, b), of 3D Chirp decimetre resolution 3D seismic profiler.

Although Schock et al. (2005) refer to this as 'Synthetic Aperture' processing, it is closer to a real–time application of amplitude summation over equal traveltime hyperbola (whereas, true synthetic aperture processing, as applied to satellite data, involves spectral decomposition based on differential along– and across–track sampling rates (e.g., Chapter 10, Robinson, 2003). While a linear time–varying–gain (TVG) is applied ($R_{TFm}R_{Fn,m}$), and the amplitude is normalised to the number of contributing shot–receiver pairs ($\frac{1}{NM}$), the wave equation is not solved, and therefore there is no dispersion correction (see, **Chapter 4**). As a result, it is most similar to the early Diffraction Migration methods rather than Kirchhoff, but only using the backwards facing half the hyperbola. This results in real–time collapsing of diffraction hyperbola, albeit with poor representation of the higher frequencies.

1.1.3 3D Chirp Decimetre–Resolution Sub–Bottom Profiler

The 3D Chirp system (Figure 1.1) is a rigid–framed high–resolution sub–bottom profiler comprising 60 hydrophone groups arranged in a 25 cm by 25 cm grid around a cross of four GeoAcoustics GeoChirp II transducers, developed at the University of Southampton (Gutowski,

2004). Navigation is provided by four RTK–GPS antennae giving sub–centimetre positioning, along with heading, pitch, and roll information. Due to the rigidity of the mat, this allows the location of a point anywhere on the array to be calculated at a positioning accuracy of $X = \pm 0.46$ cm, $Y = \pm 0.70$ cm, and $Z = \pm 1.82$ cm (Gutowski, 2004; Bull et al., 2005). This permits CMP trace binning onto a 12.5 cm by 12.5 cm grid (assuming one adheres to half receiver separation binning).

High–resolution Chirp sub–bottom profilers use linear electronics to produce a highly repeatable and tuneable swept frequency acoustic signal, capable of providing centimetric vertical resolution and decametric penetration (Schock et al., 1989; Schock and LeBlanc, 1990). These are distinct from marine Vibroseis systems (e.g., Broding et al., 1971), which are lower frequency (< 0.5 kHz) and narrow bandwidth (c. 0.1 kHz) sources, tailored for deep water operation with good penetration. In contrast, the Chirp sonar sources produce a higher frequency impulse in the range 1.0 kHz to 24.0 kHz, and modern broad bandwidth sweeps can span over three octaves, between 1.5 kHz and 13.0 kHz (Gutowski et al., 2002). This broad bandwidth reduces the pre–migration Fresnel zone, and (based on a sensible limiting resolution of $\lambda/2$) post–migration lateral resolution to < 0.1 m.

The tuneable nature of Chirp sources allow the outgoing acoustic sweep to be tailored to the specific survey requirements (Gutowski et al., 2002). For extremely shallow water (2.0 – 10.0 m) surveys (see **Chapter 3**, Plets et al. (2007), and Vardy et al. (2008)) a short, 16 ms long, sweep scanning linearly from 1.5 kHz to 13.0 kHz enables high shot rates of six to eight pulses per second (PPS), in addition to the improved resolution provided by the broad bandwidth. In deeper waters (e.g., **Chapter 6**, Bull et al. (2005), and Gutowski et al. (2008)), a longer pulse length of 32 ms allows more energy to be injected into the subsurface and therefore higher signal–to–noise ratios at depth.

1.1.4 3D VHR

In the 3D VHR system, three, 24 channel solid–state streamers with hydrophones positioned every 2.5 m are deployed 5.0 m or 7.5 m apart, behind a Mini G.I. airgun source (0.40 – 0.65 kHz) (Scheidhauer et al., 2005). D–GPS receivers on the boat and at the end of each streamer provide metre–scale positioning for each source–receiver pair, and trigger the source at regular along–track intervals. Considerable amounts of effort in post–processing are concentrated on regularising the data coverage to account for non–overlapping sail lines and streamer feathering. Linear interpolation of adjacent common–offset traces and/or removal of surplus traces were used as part of a Bin Harmonisation processing step, resulting in a single trace at each offset in each bin. The final volume of data, which is regularly sampled in both acquisition and offset space, is optimised for fast and effective processing.

The 15 cubic–inch airgun generates a strong low frequency source, giving good penetration, even in deep water, allowing the mapping of sub–surface structures to depths of over 100 m below the seabed (Scheidhauer et al., 2005; Hammami and Marillier, 2007). Although the physical size of the array and the limited horizontal resolution (1.25 m inline and 3.25 m cross–line) make it unsuitable for very shallow water surveys in harbour or fluvial environments, the lower frequency source and large source–receiver offsets are excellent for lacustrine or continental shelf applications to image targets that are several 100s metres across and several 10s metres thick (e.g., Scheidhauer et al., 2003, 2005; Hammami and Marillier, 2007). These targets are just below the resolution limits of traditional 3D seismic exploration, whilst simultaneously being too large and deeply buried to be mapped effectively by smaller systems, such as Opus3D, BOSS, SEAMAP–3D, or 3D Chirp.

1.1.5 SEAMAP-3D

Consisting of 16 hydrophones mounted in a pseudo–rigid frame towed behind a catamaran mounted boomer source, the SEAMAP-3D (SEismo

Acoustic Marine Archaeological Prospection in 3D) ultra–high resolution system is being developed by the University of Kiel, Germany (Muller et al., 2007). An RTK–GPS antenna provides centimetric positioning, which, combined with the rigidity of the frame, allows accurate correction for all large–scale tidal and swell positioning variations. The remaining statics can be handled in post–processing through standard common–offset static corrections.

The 0.5 m spaced hydrophones provide a 0.25 m by 0.25 m image of the reflected waveforms at a sample rate of 10.0 kHz. With a shot rate of 3 Hz, and 2.0 m wide single path swath, large areas (60 m by 300 m and 50 m by 120 m) can theoretically be covered in a single day, and migrated over–night using an 8 CPU Linux cluster (Muller et al., 2007). However, to date the system remains unproven, having not acquired a data set capable of demonstrating its theoretical capabilities. All acquired data sets suffer from considerable horizontal and vertical smearing, making the identification of individual targets difficult (e.g., Muller et al., 2007). Given the 2.0 m swath width and assuming a maximum survey speed of 4 knots, areas as large as 60 m by 300 m are unlikely to be suitably spatially sampled for pre–stack migration in a single survey day. Migration of under–sampled data will introduce significant aliasing artefacts, thereby requiring a strong anti–aliasing filter that would result in decreased lateral and vertical resolution. Additionally, in open water where there is a reasonable in–shore swell, one can speculate that there is likely to be strain induced flexure of the pseudo–rigid frame during towing, which would introduce errors to the static correction and therefore vertical smearing.

1.2 Thesis Outline

Despite these developments in data acquisition, there is still a lack of understanding regarding the best way to approach the data processing of 3D seismic volumes on these spatial scales. At the present time, the limiting resolution of high–resolution 3D systems (including 3D

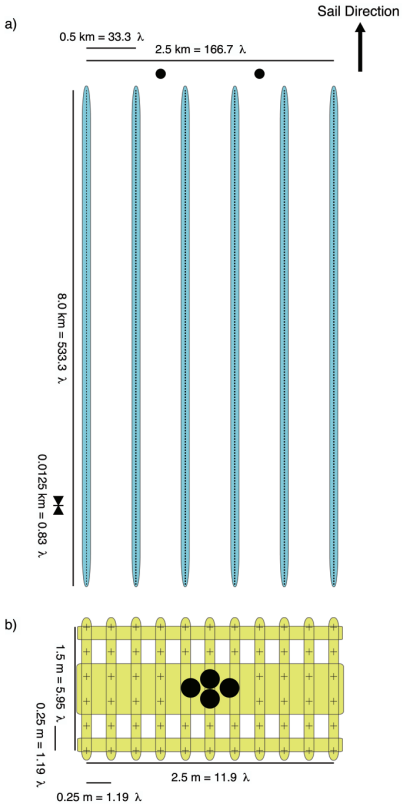

Figure 1.2: Comparison between 3D Chirp and basin–scale marine 3D seismic acquisition geometries. Panel a) illustrates a basin–scale marine 3D seismic array of six streamers (black dashed lines) towed behind the source arrays (black circles) at 500 m intervals, each 8000 m long and containing hydrophone groups at 12.5 m intervals. Panel b) illustrates the 3D Chirp array with 60 hydrophones (black crosses) arranged in a regular 25 cm grid around four central sources (black circles).

Chirp) is still largely controlled by the survey design (i.e., the areal coverage), rather than the acoustic characteristics of the system in question. The extremely high bandwidth (c. three octaves) and small receiver spacing pose significantly more stringent positioning problems compared to standard industry applications.

Receiver footprints for basin–scale marine 3D seismic acquisition and 3D Chirp can be compared by relating hydrophone intervals to source wavelength (calculated using frequency bandwidths of 0.01 – 0.1 kHz and 2.0 – 12.0 kHz, respectively), Figure 1.2. Basin–scale arrays use a single–ended spread geometry to maximise offset sampling (for velocity model picking), typically with hydrophone spacing allowing adequate sampling of the inline direction but under–sampling the cross–line (0.83 λ vs. 33.3 λ). The 3D Chirp sub–bottom profiler uses a centre–spread geometry to acquire multi–azimuth, limited offset data sets, sampling consistently in both inline and cross–line directions (1.19 λ).

During acquisition it is necessary to know where all source–receiver pairs are better than $\lambda/4$ for accurate imaging, and control these position relative to the reflected wavefield sampling footprint (common mid–points sampled by a single shot) in order to ensure complete and regular sampling. For basin–scale applications it is possible to know and control the hydrophone positions relative to ± 4.16 m and 1250 m, respectively (although the positioning can be problematic). For 3D Chirp data, however, this involves knowing the positions to better than ± 2.88 cm, and controlling these positions relative to the 1.25 m footprint width. Using a solid frame and RTK–GPS, the positioning accuracy is attainable, but controlling the position of boat and mat to better than 1.25 m is impossible. This leads to 3D Chirp volumes being irregularly spatially sampled, with lots of small gaps/discontinuities.

We stand at something of a hiatus, where, in order to prove the worth of such complex, time consuming, and expensive shallow–water sub–bottom profilers, we need to develop processing strategies that extract the best possible images from the available data in a time frame suitable for industrial applications ($\leq$ 1 month). No longer can we be happy with small–scale 3D images of volume subsets that have been 6 months to a year in preparation.

In this PhD I intend to tackle this problem from first principles. Starting by considering the fundamental limitations imposed by the system geometry, and through a combination of synthetic 3D forward modelling and applications to real data, I assess the best methods for increasing volume S/N and geometric correction using migration. The outcomes of this will then feed back into future data acquisition, providing guidance on optimum survey methodologies to limit spatial aliasing and enable robust data regularisation. In short, this should enable a more systematic approach to data acquisition and processing, thereby producing better quality and more reliable images on a shorter time scale.

1.2.1 Chapter Synopses

I begin this thesis by examining different aspects of the 3D Chirp sub–bottom profiler to identify the sources of artefacts in the final migrated volume. In **Chapter 2**, I consider the physical properties of the system: limitations in source–receiver positioning; trace–to–trace and channel–to–channel repeatability; and imaging constraints (aliasing) of the source frequency content and receiver geometry. **Chapter 3** follows this with an example data set from an atidal basin on the south coast of the UK. A combination of standard Chirp and industry processing is used to confirm the ability of the system to acquire a coherent, true 3D seismic volume, whilst also highlight deficiencies which require a new approach to data processing.

The next two **Chapters**, **4** and **5**, each tackle the fundamental processing step of imaging. **Chapter 4** theoretically examines different methods for pre– and post–stack imaging 3D seismic volumes to identify an appropriate strategy for 3D Chirp data. The imaging effectiveness and algorithm efficiency of several suitable approaches are then compared using both synthetic and real data. In **Chapter 5** a new approach to pre–stack 3D Kirchhoff migration using a series of band–limited traces is developed, and compared against results from the standard imaging techniques derived in **Chapter 4**.

The final **Chapter**, **6**, takes the processing methodologies developed during **Chapters 4** and **5**, and applies them to another data set. Acquired in Windermere, UK, this geological case study presents an extreme case of the processing problems normally encountered in 3D Chirp volumes, targeting a geologically complex environment with low amplitude, steeply dipping (up to 20°) reflectors and a thick (up to 60 m) sediment over–burden. Application of the developed imaging techniques affords the interpretation of a coherent, geometrically correct volume to complement existing Multi–Channel Seismic (MCS) and core data.

"If you know your enemy and know yourself, you need not fear the result of a hundred battles. If you know yourself but not the enemy, for every victory gained you will also suffer defeat."

Sun Tzu, The Art of War (c. 400-320 BC)

2

System Characterisation

Although the 3D Chirp sub–bottom profiler is, to first principles, a downscaling of standard industry 3D seismic technology, for processing purposes it cannot simply be treated as such. Limited source–receiver offsets and the source directivity make some industry techniques (e.g., tau–p filtering and interval velocity picking) impractical, while irregular spatial coverage, combined with a broad source bandwidth and high temporal sampling rate, make reliable 3D imaging difficult. Neither can it be perceived as a more complex version of a standard 2D Chirp system; sea surface ghosting, interference within the frame, elevation fluctuations, and greater sensitivity to source/receiver repeatability (for volume coherency) pose significantly greater problems during processing.

In this Chapter, the fundamental limitations of the system will be quantified and considered. Initially, the most basic components of 3D seismic surveying, the source–receiver pair positioning and shot timing, will be verified. Thereafter, sources of systematic noise such as

source/receiver repeatability, which contaminate a migrated volume through imperfect summation or cancellation of energy, are discussed. Finally, the physical limitations of the system and the constraints these impose on imaging will be reviewed. Together, this information will provide the theoretical basis from which a suitable approach to the processing and imaging of decimetre resolution 3D seismic volumes can be developed.

2.1 Shot Timing and Positioning

The acquisition of a true 3D seismic volume involves accurately positioning each source–receiver pair in all three dimensions; X, Y, and Z. This allows each seismic trace to be positioned within a geographically orientated grid, resulting in a coherent volume of data that can then be migrated to produce an accurate image of the seabed and subsurface structure. The Reciprocity Theorem states that, from a wavefield perspective, shot (x_s, y_s) and receiver (x_g, y_g) locations are interchangeable (Vermeer, 1990). Therefore, the same positioning requirements apply to both sources and receivers.

In order to adequately constrain the reflected wavefields, the error in horizontal position of each source/receiver pair needs to satisfy the criterion $\pm$ X = $\pm$ Y $\leq \lambda/4$. For the broadband sweeps most used in this thesis (Table 2.2) the bandwidth (upper cutoff frequency) is 13.0 kHz, which equates to a wavelength of 0.115 m, assuming a velocity of 1500 ms^{-1}. This imposes a positioning accuracy of $\pm$2.88 cm. Similarly, to ensure constructive summation of reflectors on coincident traces, the vertical position needs to be known better than the side–lobe to main–peak distance of the auto–correlated Chirp wavelet. For the highest resolution, broad bandwidth sweeps (w13 and w32; Table 2.2) this measures 0.06 ms (Plets, 2007), which equates to $\pm$4.5 cm in a 1500 ms^{-1} velocity field.

To achieve this required positioning accuracy, the 3D Chirp sub–bottom profiler uses a dynamically updated RTK–GPS positioning

string from an antenna, mounted on the rear port side of the mat, and attitude information (heading, pitch, and roll) from three antennae mounted on the other corners of the mat. Due to the rigidity of the frame, this allows accurate positioning of each source–receiver pair, using the transformation (Gutowski, 2004):

$$\begin{bmatrix} X' \\ Y' \\ Z' \end{bmatrix} = \begin{bmatrix} c_1 & b_1 & k_1 \\ c_2 & b_2 & k_2 \\ c_3 & b_3 & k_3 \end{bmatrix} \begin{bmatrix} X - X_{COG} \\ Y - Y_{COG} \\ Z - Z_{COG} \end{bmatrix}; \tag{2.1}$$

where (X', Y', Z') are co-ordinates relative to the known position of the RTK–GPS antenna, $(\overrightarrow{c},\ \overrightarrow{b},\ \overrightarrow{k})$ are unit vectors which define the array co–ordinates for the mat relative to this location using the mat centre–of–gravity location $(X_{COG}, Y_{COG}, Z_{COG})$, and (X, Y, and Z) the source/receiver positions in the reference frame.

Previous static tests (Gutowski, 2004) have estimated the accuracy of resulting positions as $X = \pm 0.46$ cm and $Y = \pm 0.70$ cm, while seabed coherency within a single 12.5 cm bin provides an estimate for vertical positioning accuracy as $Z = \pm 1.82$ cm. This is significantly within the minimum required level of positioning accuracy. Cross–referencing of these locations (which are recorded five times per second) with shots triggered using a GPS clock allows each source–receiver pair to be located geographically and, subsequently, allocated into a CMP bin.

2.1.1 Positioning

Key to this positioning method, is maintaining the appropriate quality of the GPS strings. If the accuracy drops below RTK quality the criterion outlined previously will no longer be satisfied. To define the quality of the GPS data, the Ashtech Sagitta (RTK–GPS system used) allocates a "*Fix Quality Index*" (Thales Navigation, 2002). Each string is assigned a value between 0 and 19 (where 0 is equivalent to

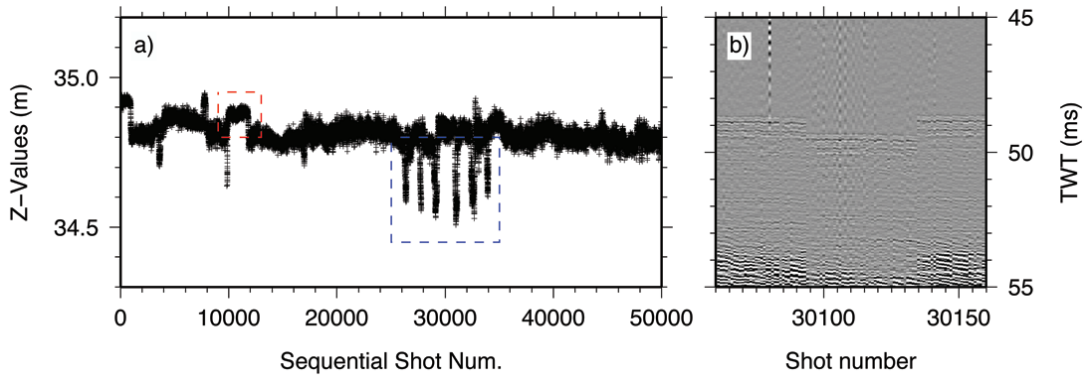

Figure 2.1: Figure showing shot z-value positions over the course of a single survey day, a), highlighting prolonged z-value jumps (red dashed box) and short time period drifts or jumps in the z-values (blue dashed box). Panel b) shows short seismic section, illustrating the effect on seabed continuity of short time period jumps in recorded z–value (shots 30094 to 30140).

no positioning solution, and anything between 14 and 19 it is of RTK–GPS quality), using the formula:

$$Q = 14 + 7\left[1 - \left(\frac{LPME_{measured}}{LPME_{max}}\right)\right]; \tag{2.2}$$

where, $LPME$ stands for the Line of Position Mean Error.

$LPME_{measured}$ is the the quadratic average of the weighted residuals on each positioning solution calculated using the Long–Range Kinematic (LRK®) processing method of the carrier phase signals. While $LPME_{max}$ is defined as:

$$\begin{aligned} &15 + Station - to - mobile\ Distance,\ in\ km \quad (single - frequency)\,, \\ &20 + Station - to - mobile\ Distance,\ in\ km \quad (dual - frequency)\,. \end{aligned}$$

However, in practise we find that sub–RTK quality GPS strings are assigned $Q \geq 14$; Figure 2.1 shows Z–values positions for 50,000 shots, all assigned RTK–GPS quality, together with a subset of example data. The data was acquired in a lake where there were no tides

or currents and little wind to drive wave generation. Despite the calm conditions, there are sudden jumps in Z–value position ≥ 10.0 cm, for both prolonged (e.g., red dashed box) and shorter periods of time (e.g., blue dashed box). The effect on seabed continuity post–geometry compensation can be seen in Figure 2.1b, where there is a distinct change in seabed reflector position between shots 30094 to 30140.

These periods of poor quality GPS positioning require removing from the data volume prior to processing. While positions flagged as non–RTK quality can easily be filtered automatically, it is not possible to be more stringent on $Q \geq 14$ values since the GGA navigation string used for source/receiver position simply flags RTK quality or not, without passing on the specific Quality Index. Therefore, a manual assessment of the GPS data is required.

2.1.2 Timing

Since the system has been designed to trigger the sources at regular time intervals, rather than regular distances, the RTK–GPS derived locations need cross referencing with equally accurate shot times in order to position the source–receiver pair for each trace. As outlined above, for traces to constructively combine during CMP stacking or migration summation, coincident traces need to be consistent within the peak–to–side lobe offset of the auto–correlated Chirp wavelet. For the broad band sweeps w13 and w32 this corresponds to 0.06 ms.

If each sample was being timed individually, then this would be equivalent to the required timing accuracy. However, the time samples on each trace are tagged sequentially from the shot trigger. This makes the timing requirements based on accurate timing of the absolute shot time for cross–referencing with the positioning. Since the RTK–GPS positioning is updated five times per second, and positions linearly interpolated in between, this is significantly less stringent; an error of 1.0 ms would require the mat to be moving at a vertical velocity of 45

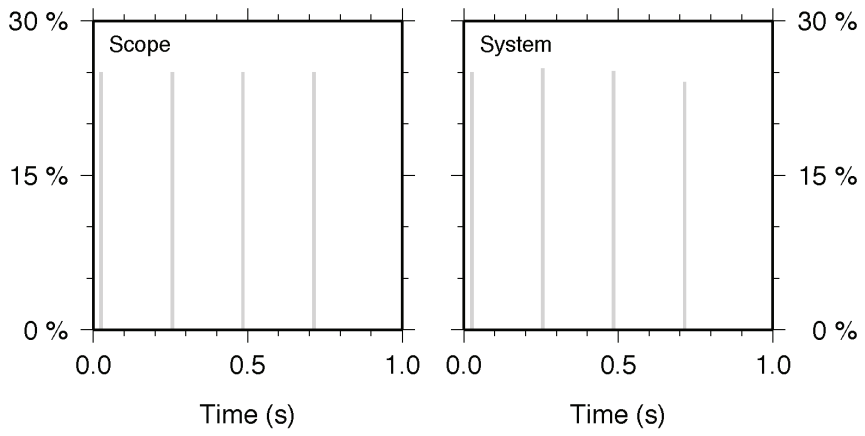

Figure 2.2: Figure showing histograms of shot trigger times as logged by the acquisition system, and separately identified by threshold detection on a signal recorded using a 50 MHz oscilloscope. Difference between two sets of times is < 0.05 ms..

m/s to induce the 4.5 cm change error in positioning for destructive interference between coincident traces.

A GPS clock is used to provide hour, minute, and whole second time flags, from which an internal counter (triggered by a 1 PPS pulse from the GPS clock at the beginning of each second) provides ms times. The 1 PPS pulse also prompts a hardware pulse generator in the Field–Programmable Gate Array (FPGA) logic, which generates a 1 second long pulse train containing the required number of square wave shot triggers. This signal is split two ways to trigger both the Chirp sweep, and the acquisition system, where it is time stamped using the GPS and CPU counter.

This results in shot triggers that are regular within each second, where only the time stamping can be affected by system load. Figure 2.2 compares histograms of shot times as logged by the acquisition system, and separately through threshold identification of the trigger signal recorded on a 50 MHz oscilloscope. The difference in timing between the two recording methods is < 0.05 ms.

Shot timing in marine surveying is, however, complicated by the

sources and receivers being part of a dynamic environment. Whereas, on land, the sources and geophones are secured in fixed locations, during marine acquisition they are (with the exception of ocean bottom cable or seismometer deployments) constantly in motion being towed behind the survey vessel.

To easier see how this affects the final quality of an imaged volume, two example thought experiments will be introduced. These illustrate two different applications of the 3D Chirp sub–bottom profiler, and similar systems:

i) **Inshore Application:** For inshore applications (such as harbour basins, rivers, or estuaries) where the seabed is c. 10.0 m depth, this corresponds to 13.0 ms in a 1500 m/s velocity field. Including 15 ms of subsurface structure, and 2 ms for diffracted energy moved to later times, this equates to a trace length of 30 ms. Pulse rates would be high (six or eight PPS) and lengths short (16.37 ms; Table 2.2) to maximise acquisition efficiency, providing $\geq$ 20 million traces.

ii) **Shelf Application:** Here the survey target could be a slump deposit or slide scarp situated just offshore (or, equally, in a fjord or lake) in c. 50 m of water. Assuming a velocity of 1500 m/s this equates to c. 66 ms TWT to the seabed. Including 20 ms of subsurface structure, and 14 ms for recording diffracted energy moved to later times, meaning a trace length of 100 ms. Pulse rates could never go above four PPS and lengths would be long (32.74 ms; Table 2.2) to maximise energy output, so a survey is likely to contain only c. 15 million traces.

The problems in the accurate timing of energy manifest in two forms: movement within the source sweep time window; and movement within the recording time window. The former results from the source sweep being of finite length, therefore any change in array position will alter the depth and ray path to a reflection point for the different frequency components. Assuming a constant survey speed of 4 knots (2.0 m/s), for the two thought experiments lateral movement during the sweep

window (16.37 ms and 32.74 ms; Table 2.2) is c. 3.27 cm and c. 6.55 cm, respectively. Vertical movement will offset the different frequencies in time, introducing correlation errors and smearing energy into the Klauder wavelet side–lobes and side–tail oscillations. Relative to a CMP bin size of 12.5 cm the horizontal smearing is insignificant, but vertical movement is not. Particularly during shelf applications, where the longer sweeps will be used, there is likely to be reduction in resolution caused by vertical movement during the sweep output window.

The latter form of timing error is caused by the array being towed at an approximately constant speed throughout the trace recording window. Again, assuming a consistent survey speed of 2.0 m/s, it can be seen that for the inshore thought experiment a recording trace length of 47 ms (30 ms of trace plus 16.37 ms long source sweep; Table 2.2) the source/receiver array would move c. 0.094 m during recording, i.e. almost one CMP bin size. Lines acquired with sail directions 180° out of phase will result in reflections from the same location being positioned ≤ 0.188 m apart, i.e., up to two CMP bins apart when binning at 12.5 cm. Given a theoretical horizontal resolution for interpretation of three CMP bin sizes (0.375 m), this is not ideal but within acceptable limits on the positioning of the reflected energy. For the shelf experiment, however, a recording trace length of 133 ms corresponds to 0.266 m of movement between the position associated with the first sample (trigger time) and the last sample, therefore 0.532 m when acquisition direction is 180° out of phase. This maximum error in energy location is within the theoretical resolution limit of the system, and would lead to a significant loss of resolution in the deeper sections of similar volumes, along with artefacts introduced by the incorrect summation and cancellation of energy. Therefore, for long trace lengths where the array moves a significant distance within the recording time of a single shot, assigning source/receiver locations based on the trigger time (start of the trace) is not accurate enough.

If the reduction in data quality due to these timing errors is large, both can be accommodated in post–processing. Temporal offsets between

frequency components could be removed by correlation with a series of band limited sweeps which are then each static shifted to minimise correlation errors. While, the easiest solution to array movement during recording is to apply a static shift to the recorded trigger time prior to assigning receiver positions, thereby moving the point on the trace which is positioned correctly. Given the loss of resolution with depth through attenuation of the higher frequencies, an appropriate time would be an approximate seabed time, thereby preserving the resolution afforded by the higher frequencies. Unless subsurface structure extends ≥ 100 ms below this approximate seabed, the smearing of deeper structure will also be minimised.

2.2 Source Repeatability

Pre–stack, the recorded wavefields are 5D, being dependent upon source and receiver locations (x_s, y_s and x_g, y_g, respectively), together with time, t. Ideally, a survey would completely sample all five of these dimensions across the entire survey area. However, in reality, financial and physical limitations mean that all 5D are never completely sampled. Rather, it is common to selectively sample up to three of the dimensions to the required accuracy, and sub–sample the remaining. This has led some (e.g., Padhi and Holley, 1997) to consider a 3D survey in terms of "*minimal data sets*"; the least amount of data required to adequately image a reflector. However, these minimal data sets are normally of limited spatial extent, meaning that a completely imaged volume is composed from a number of juxtaposed (or, preferably, overlapping) minimal data sets.

The 3D Chirp sub–bottom profiler uses an centre–spread geometry to acquire shot centred minimal data sets, where subsets of the survey area surrounding each source location are densely sampled in the receiver (x_g, y_g) and time dimensions. These sub–volumes are then overlapped with regular, but less densely spaced, shot locations. Superposition of these minimal data sets results in the pre–stack wave-

fields being correctly sampled in the receiver and time dimensions, but under–sampled in the source dimensions.

The coherent migration of 3D seismic data involves the redistribution of reflected energy over a surface of equal travel time. In simple terms; coherent energy will constructively interfere, while incoherent energy (i.e., noise) will destructively interfere. This results in a geometrically correct (for the chosen migration velocity) volume with improved S/N ratio. This reliance on the constructive interference of 'real' reflections, implies an obvious reliance on the consistency in amplitude and phase of the reflected wavelets. If the volume is composed from a number of different shots and receivers, this is then fundamentally dependent on the repeatability of the source and receivers.

I have used two methods to assess the source/receiver repeatability:

2.2.1 Verbeek and McGee Method

Verbeek and McGee (1995) define a method of estimating the source repeatability based on the direct amplitude comparison of two equivalent traces using a Repeatability Index (RI), defined as:

$$RI = min|s\,(k)\,|; \tag{2.3}$$

where

$$s\,(k) = \frac{\sum_{i=0}^{N}|s_{1(i)} - s_{2(i-k)}|}{max|s_{1(i)}| \times N}; \tag{2.4}$$

$s_{1(i)}$ and $s_{2(i-k)}$ are the two equivalent traces digitised into records with samples $i \rightarrow N$. Normalising to the maximum of $s_{1(i)}$, results in large values of RI representing poor repeatability, and zero being perfectly repeatable.

By windowing data to the direct arrival, and subtracting an estimate of the noise contribution extracted from the water column, Verbeek and McGee (1995) compiled repeatability values for eight different

Source	Source depth (cm)	Peak frequency (kHz)	-40 dB bandwidth (kHz)	Repeatability index
Chirp sonar				
5 ms	15	6.5	8.5	0.0048
10 ms	15	6.5	8.5	0.0063
16 ms*	–	5.0	6.0	0.00005
16 ms†	–	7.25	11.5	0.00005
20 ms	15	6.5	8.5	0.0361
32 ms*	–	5.0	6.0	0.00004
32 ms†	–	7.25	11.5	0.00006
Boomer				
105 J	5	10.0	34.5	0.0025
175 J	5	8.0	40.0	0.0020
280 J	5	6.5	45.7	0.0028
350 J	5	5.7	41.4	0.0027

Table 2.1: Summary of relevant source repeatabilities for a number of high–resolution seismic sources, from Verbeek and McGee (1995). Lines shaded grey show data gathered using the 3D Chirp transducer array and an omnidirectional, spherical hydrophone transducer in the ISVR test tank. The lines marked $*$ represent the traditional Blackman–Harris Chirp sweep, while those marked † are linearly swept sweeps with sin squared 8^{th} tapers (Gutowski et al., 2002; Plets et al., 2007).

marine sources (summarised in Table 2.1). They concluded that Chirp sonar had a RI twice that of the more conventional pinger–type sonar and boomer sources.

For comparison, a data set was acquired specifically to asses source repeatability, using the University of Southampton's Institute for Sound and Vibration Research (ISVR) test tank with dimensions of 8.0 m by 8.0 m by 4.0 m. Fixing a 16 mm diameter, omnidirectional (to within 2 dB) spherical hydrophone, mounted in a 20 mm diameter polyurethane cylinder, 1.0 m directly in front of our transducer array, I recorded the outgoing impulse on a LeCroy Oscilloscope with minimal interference from reflections off the bottom and sides of the tank.

Processing of these uncorrelated traces in a similar method to that of Verbeek and McGee (1995), yielded estimates for source repeatability given in Table 2.1. However, instead of comparing the amplitudes of similar traces, each trace was individually compared to an average trace, thereby also including any drifting changes that would not otherwise have been identified using the basic method. Since gradual variations in the source/receiver repeatability are just as damaging to the summation and cancellation during migration, including these effects is important. Thus, Equation 2.4 becomes:

$$s\left(k\right) = \frac{\sum_{i=0}^{N} |s_{1(i)} - \bar{s}_{(i)}|}{max|s_{1(i)}| \times N}. \tag{2.5}$$

The amplitude resolution of the oscilloscope was $\pm 10^{-5}$ V. Using the standard method of error estimation, this allows us to put a value on the limiting resolution of RI:

$$\begin{aligned} \left(\frac{\Delta RI}{RI}\right)^2 &= \left(\frac{\Delta s_1}{s_1}\right)^2 + \left(\frac{\Delta \bar{s}}{\bar{s}}\right)^2, \\ \Delta RI &= \sqrt{\left(\frac{\Delta s_1}{s_1}\right)^2 + \left(\frac{\Delta \bar{s}}{\bar{s}}\right)^2} \times RI; \end{aligned} \tag{2.6}$$

where s_1 is the amplitude of the trace, $\bar{s}$ is the amplitude of the average trace, and ΔRI, Δs_1, $\Delta \bar{s}$ are the associated errors. Using average amplitudes for each trace, the resolution of RI becomes:

$$\Delta RI \sim 3 \times 10^{-11}. \tag{2.7}$$

Therefore, the repeatability indices estimated for our different sweeps (Table 2.1), although small (two orders of magnitude smaller than those of Verbeek and McGee (1995)), are well within the detectable variation. It is, perhaps, to be expected that our source RI values are better than those previously published, the comparison of each trace

with an average trace will dampen the contribution of high–frequency changes between adjacent traces to the overall RI value.

Although this method produces meaningful results that are sensitive to small fluctuations in phase and/or amplitude, it is not possible (without a visual inspection) to actually discern between these two effects. Therefore, it is unclear whether fluctuations in source signal are due to timing offsets, or amplitude variations.

2.2.2 Cross–Correlation Method

The cross–correlation of traces is one of the most basic tools in seismic processing (e.g., Yilmaz, 1987). It is particularly useful for estimating the similarity of two traces, as the peak value represents a measure of their similarity in amplitude, and the sample location of this peak value the phase difference. When using the cross–correlation in this manner, it is common to normalise to the product of the summed magnitudes of each trace; thus meaning a value of one represents perfectly repeatability, and numbers close to zero are highly unrepeatable.

$$\phi_{s_1 s_2}(\tau) =^{limit}_{N\to\infty} \frac{\sum_{k=-N}^{N} s_{1(k)} s_{2(k+\tau)}}{\sqrt{\sum_{k=-N}^{N} s_{1(k)}^2 \sum_{k=-N}^{N} s_{2(k)}^2}} \tag{2.8}$$

where s_1 and s_2, are the two traces being compared, and N the number of samples.

This was used to calculate repeatabilities for 17 Chirp sweeps using data acquired at the ISVR test tank (see, Table 2.2). As before, cross–correlation was between each trace and an average trace to make the experiment sensitive to gradual, as well as sudden, changes in the produced waveform. Errors quoted are the standard error:

$$error_{\bar{x}} = \frac{\sigma}{\sqrt{N}}; \tag{2.9}$$

where $\bar{x}$ is the mean of N values, and σ the standard deviation.

Sweep	Frequency bandwidth (kHz)	Sweep length (ms)	Cross correlated peak	Phase Offset (ms)
w01	Lin. 2.0 – 6.0 Gauss	16.37	0.9939 ± 0.0025	0.0010 ± 0.0050
w02	Lin. 2.5 – 9.0 Gauss	16.37	0.9987 ± 0.0003	0.0000 ± 0.0014
w03	Lin. 2.0 – 6.0 Gauss	32.74	0.9970 ± 0.0005	0.0000 ± 0.0000
w04	Lin. 2.5 – 9.0 Gauss	32.74	0.9940 ± 0.0013	0.0010 ± 0.0017
w05	Lin. 2.0 – 8.0 Gauss	16.37	0.9994 ± 0.0001	0.0000 ± 0.0000
w06	Lin. 2.0 – 8.0 Gauss	32.74	0.9962 ± 0.0007	0.0000 ± 0.0000
w08	Lin. 1.5 – 13.0 Gauss	32.74	0.9590 ± 0.0037	0.0660 ± 0.0301
w09	Quad. 1.5 – 13.0 Gauss	32.74	0.9500 ± 0.0430	-0.1000 ± 0.0965
w10	Log. 1.5 – 13.0 Chi rev.	32.74	0.9870 ± 0.0021	0.1190 ± 0.0807
w11	Lin. 1.5 – 13.0 Chi	32.74	0.9454 ± 0.0015	0.2140 ± 0.0824
w12	Lin. 1.5 – 13.0 Sine sq. 4^{th}	32.74	0.9664 ± 0.0049	0.0750 ± 0.0419
w13	Lin. 1.5 – 13.0 Sine sq. 8^{th}	32.74	0.9928 ± 0.0017	0.0020 ± 0.0013
w25	Lin. 2.5 – 9.0 Sine sq. 8^{th}	32.74	0.9847 ± 0.0023	0.0620 ± 0.0431
w27	Quad. 2.5 – 9.0 Sine sq. 8^{th}	32.74	0.9970 ± 0.0006	0.0020 ± 0.0013
w32	Lin. 1.5 – 13.0 Sine sq. 8^{th}	16.37	0.9977 ± 0.0004	0.0000 ± 0.0014
w33	Lin. 3.0 – 8.0 Sine sq. 8^{th}	16.37	0.9993 ± 0.0002	-0.0020 ± 0.0013
w34	Lin. 2.5 – 9.0 Sine sq. 8^{th}	16.37	0.9985 ± 0.0004	-0.0020 ± 0.0019

Table 2.2: Amplitude and phase repeatabilities for a number of GeoAcoustics Chirp source sweeps calculated using the cross–correlation method. Data was acquired using a 50 MHz oscilloscope in the controlled conditions of the ISVR test tank with a hydrophone positioned 1.0 m directly in front of the four Chirp transducers. Lines shaded grey highlight the two sweeps considered in greater detail.

As with results obtained using the Verbeek and McGee (1995) method, fluctuations in amplitude and phase of the outgoing sweep are extremely small. Of particular interest are sweeps w13 and w32 (shaded grey in Table 2.2), which are the two broadband sweeps most often used in this thesis. These both demonstrate amplitude variations of less than 0.1 %, and phase of less than 0.002 ms.

2.2.3 Reflection Repeatability

Analysis of data acquired to identify variations in the amplitude and phase content of our Chirp source sweeps has been presented, using

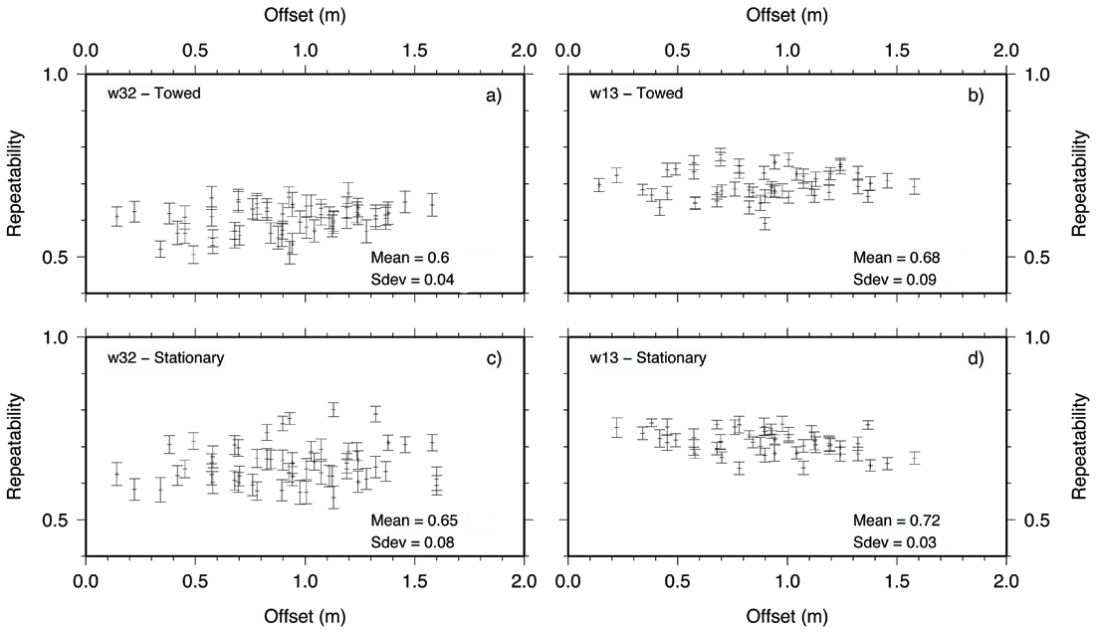

Figure 2.3: Four panels showing channel–to–channel variation, for sweeps w13 and w32, whilst stationary and under tow. Repeatability (cross–correlation method) is decreased c. 5 % by towing noise, but, even when stationary, the repeatability of the reflected waveform is significantly lower than the outgoing sweep (Table 2.2).

two methods to examine the outgoing impulse as recorded in a highly controlled environment. It is equally, if not more, interesting to consider the repeatability of the seabed reflectivity under true survey conditions. As has been demonstrated by Muller et al. (2002), the environmental effects of engine noise, towing, sea state, and sea surface ghosting, can cause the observed reflection stability to be one to two orders of magnitude worse than that of the source alone.

For this reason, these results will be compared and contrasted with the seabed reflector stability for a number of source sweeps recorded whilst stationary in Empress Dock (Southampton) with the boat engine switched off, and whilst towing. This enables an approximate break down of fluctuations in the phase and amplitude of the seabed wavelet into its constituent components, examining the effect of each individually.

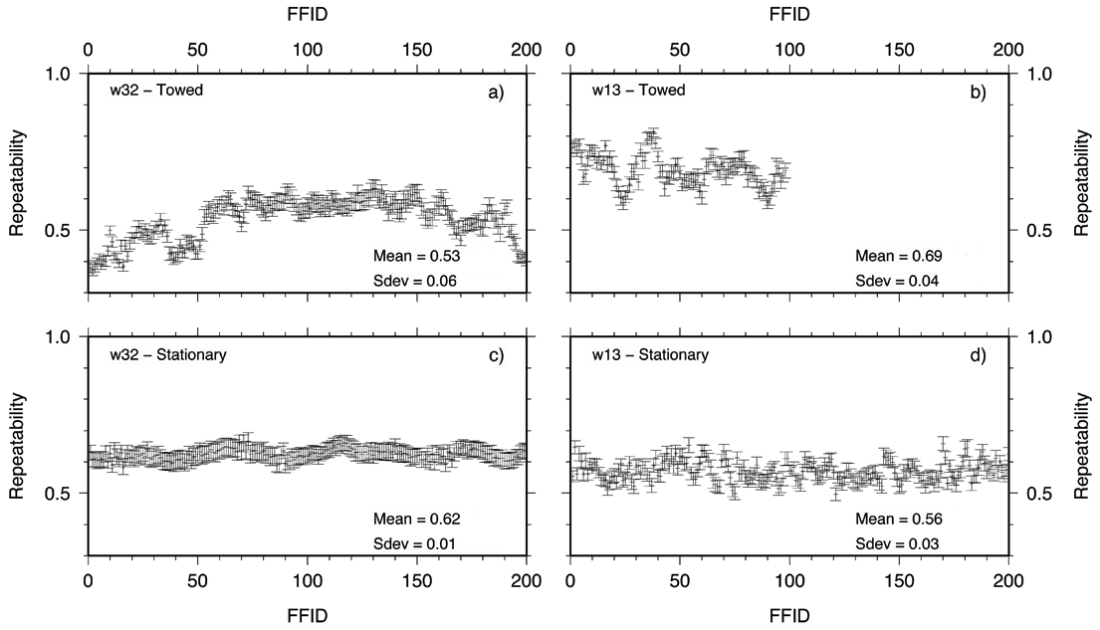

Figure 2.4: Four panels showing shot–to–shot variation, for sweeps w13 and w32, whilst under tow (a and b) and stationary (c and d). Repeatability (cross–correlation method) is decreased c. 5 % by towing noise, but, even when stationary, the repeatability of the reflected waveform is significantly lower than the outgoing sweep (Table 2.2).

Primarily, the cross–correlation method was used in order to separate out the amplitude and phase components. Figure 2.3 shows seabed reflector amplitude repeatability for each channel, averaged over 200 traces, using sweeps w13 and w32, whilst moored and towed. There are fluctuations between channels of ± 0.1, centred about 0.61 (towed) and 0.65 (stationary) for w32, and 0.68 (towed) and 0.72 (stationary) for w13. While there is a clear decrease in repeatability (c. 0.04) between towed and stationary tests, all demonstrate a dramatic difference between source stability, as recorded in the ISVR test tank, and seabed reflector repeatability; decreasing from 0.99 to average values of 0.70 and 0.63 for w13 and w32, respectively.

Similar results can be seen in the shot–to–shot variation (Figure 2.4), where seabed repeatability's vary by ± 0.06, but are consistently 0.37 and 0.42 (on average) lower than the source sweep for w13 and w32,

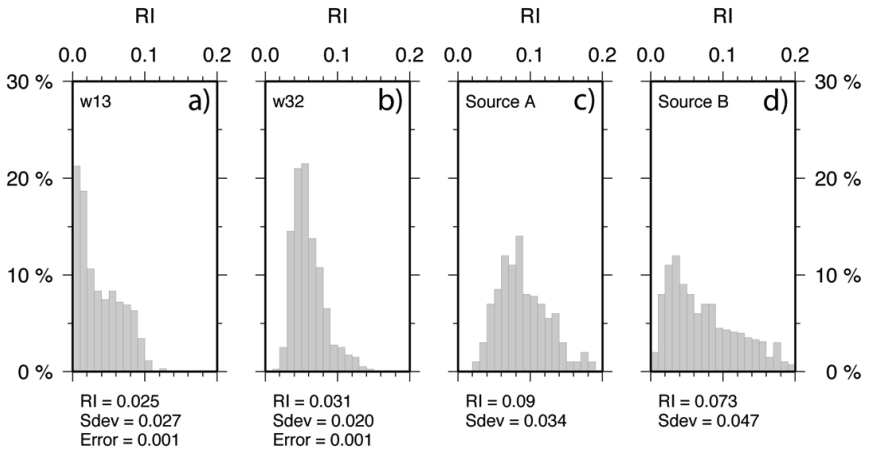

Figure 2.5: Comparison between RI histograms for two 3D Chirp surveys (a and b), and two boomer sources (c and d) from Muller et al. (2002). The Chirp data uses two different source sweeps: a 32.74 ms long 1.5 kHz to 13.0 kHz linear square wave sweep with sine sq. 8^{th} tapers, w13; and its 16.37 ms duration equivalent, w32. Data was correlated and windowed around the seabed arrival. The boomer data was bandpass filtered using frequency gates 100–200–1400-1600 Hz.

respectively. Stratigraphy plays a significant factor in complicating the shot–to–shot repeatability of the towed results, which is why it was possible to use only a 100 shot gather for w13. Similarly, the first 50 and last 10 shots for w32 are also affected by changes in seabed type. The change is, however, consistent; being caused by considering the reflected seabed wavelet.

For comparison with results presented in Table 2.1, and taking care to ensure that geological variations did not dominate the signal, a block of 200 traces from two surveys, using two different sources sweeps (w13 and w32), were processed using the modified method of Verbeek and McGee (1995) (see, Figure 2.5). Amplitudes from a window centred on the seabed reflection (thereby excluding the direct arrival, which is complicated by interactions with the sea surface) were correlated with the source sweep, but not otherwise processed.

Despite being acquired under survey conditions, the results presented in Figure 2.5 are comparable to that of Verbeek and McGee (1995).

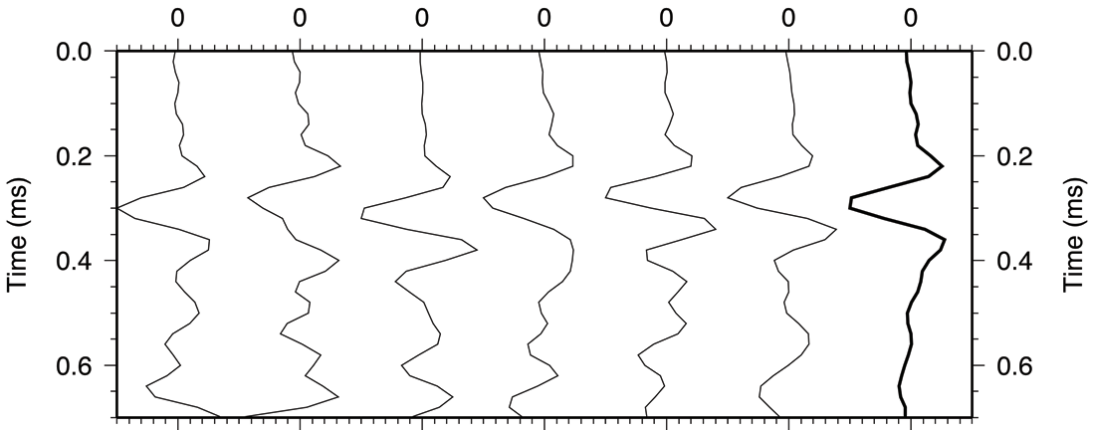

Figure 2.6: Figure comparing seafloor response for six randomly selected individual channels with average trace (thicker black line).

Repeatability indices of 0.031 ± 0.001 and 0.025 ± 0.001 for the 16.37 ms and 32.74 ms sweeps, respectively, are consistent with the 0.0361 observed for the Verbeek and McGee (1995) 20 ms sweep. Although this method does not separate out amplitude and phase influences, it supports the results obtained using the cross–correlation method; the repeatability of the seabed reflection is reduced from the very high source waveform repeatability. This concurs with the observations of Muller et al. (2002).

The cause of such a significant decrease in repeatability between the outgoing and reflected waveforms is likely to be the complicated interaction of a number of different issues. Figure 2.6 shows six randomly selected traces from a single stationary gather acquired using w32, together with the average trace for that gather (darker black line). The peak of the Klauder wavelet corresponding to the seafloor reflection consistently occurs around 0.3 ms, and demonstrates a highly reliable waveform trace–to–trace. However, following the peak, and causing minor distortion of the trailing side–lobe, the individual traces contain a series of relatively high amplitude, highly variable cycles that are not present on the average trace. For both repeatability methods, this difference is a dominant part of the decrease in repeatability, causing a reduction of c. 0.3 in the cross–correlation results.

Bull et al. (1998) have shown that increased energy in trailing side–lobe(s) can be generated by non–white seafloor reflectors (i.e., the presence of a graded transition zone). Undoubtedly, this is a contributing factor, particularly since the stationary data was acquired in a harbour basin where the sedimentary infill consists of very fine, unconsolidated silt. However, this transition zone is unlikely to vary greatly within a single footprint area (1.25×1.00 m), suggesting that the variation between traces is independent from the environmental conditions. Instead, it is thought that the trace–to–trace differences are caused by sea–surface ghosting, along with interaction between the frame and the reflected wavefield. Since the source–receiver offset and orientation of each channel differs, so will the arrival time of the sea surface ghost and any internal reflections from within the frame. Therefore, in order to ensure effective summation of traces during stacking or migration, it is important to repeatedly cover an area, providing dense coverage including contributions from a large number of channels.

2.3 Sampling and Aliasing

Aliasing stems from the quantisation of data from a continuous record into a series of discrete samples. In modern seismic recording methods this can occur both temporally and spatially: the digitisation of the seismic trace means it is recorded as a series of amplitude values; while receiver spacing leads to the seismic wavefield being discretely sampled in the X/Y plane.

If one considers a seismic trace as a 1–dimensional time series, then the temporal sampling is governed by the sampling theorem (Shannon, 1948). By modelling the seismic trace as the convolution between a continuous signal and a series of equidistant delta functions with a spacing interval equal to the sampling interval, the sampled signal, $\hat{s}(t)$, can be written in the time domain as (Robinson and Durrani,

1986):

$$\hat{s}(t) = s(t)\sum_{n=\infty}^{\infty}\delta(t - n\Delta t); \tag{2.10}$$

and in the frequency domain as:

$$S_A(\omega) = S(\omega) * \sum_{k=-\infty}^{\infty}\delta\left(\omega - \frac{k}{\Delta t}\right); \tag{2.11}$$

where $S(\omega)$ is the continuous Fourier transform of $s\,(t)$, and $S_A(\omega)$ the Fourier transform of the discretely sampled data.

This equation tells us that, in convolving the continuous signal with a series of delta function, we map the original signal, $S(\omega)$, onto each delta functions. If this spacing of $1/\Delta t$ is not broad enough to contain all the information in $S(\omega)$, then there will be overlap between neighbouring delta functions at + $1/2\Delta t$ and - $1/2\Delta t$.

This forms the basis of the Nyquist Criterion, or Nyquist frequency, which states that to record unaliased data for a given frequency bandwidth, f_{band}, the sampling interval is:

$$\Delta t \leq \frac{1}{2f_{band}}. \tag{2.12}$$

If we apply this to the 3D Chirp profiler, where f_{band} is 13.0 kHz, the Nyquist frequency is 26 kHz, equivalent to a sampling interval of 38.46 μs. Presently, we record the data at a temporal sampling rate of 50 kHz, equivalent to 20.0 μs, and are therefore considerably oversampling the data relative to the Nyquist Criterion. This is important because, although frequencies $\leq f_N$ will be represented correctly in the data, finer sampling enables accurate representation of the waveform shapes.

Expanding this 1–dimensional approach into 3–dimensions involves including spatial aliasing as well as temporal. Although the two are not entirely independent (spatial is dependent upon frequency content, which is intimately tied to the Nyquist Criterion and temporal

sampling), spatial aliasing is normally considered separately. In part, this is because it is easier to visualise, and therefore comprehend, with just two variables $(\Delta x, \Delta y)$ rather than three $(\Delta x, \Delta y, \Delta t)$, but also because spatial aliasing manifests itself in a number of different ways.

Following the terminology of Biondi (2007), there are three fundamental types of spatial aliasing; data, image, and operator, each corresponding to aliasing in a particular data space. For simplicity, if one considers the process a trace undergoes during a Kirchhoff migration (Yilmaz, 1987): the data is recorded in (x, y, t) space and will be data aliased if trace separation is too large; each trace is then expanded into image space, forming the migration ellipsoid by solving the wave equation, if the sampling of the migration aperture (in x, y, t and offset domains) is too coarse then operator aliasing occurs; finally, the imaged ellipsoids are summed into migrated data space, where over decimation of the spatial or temporal domains will cause image aliasing. Operator aliasing is entirely dependent upon the choice of migration algorithm and will be discussed further in **Chapter 5**. However, data and image aliasing are directly related to the acquisition, and will be discussed further now:

2.3.1 Data Aliasing

Data aliasing is caused by the spatial sampling of the recorded data being too coarse to accurately image the stratigraphy at the recorded frequencies. Knowing the component frequencies of the reflected waveforms and the spatial sampling, one can express this as a limit on the maximum resolvable dip angle. For a constant velocity, this is given by the function (Yilmaz, 1987):

$$sin\ \theta_{max} \leq \frac{v}{2 f_{band} \Delta x}; \tag{2.13}$$

where Δx is the spatial sampling and f_{band} the source frequency bandwidth, while θ_{max} is the corresponding maximum dip angle.

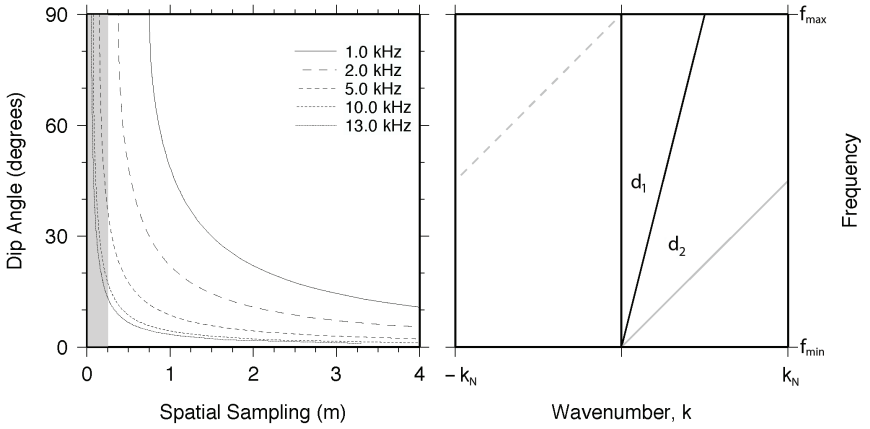

Figure 2.7: Panel a) showing spatial sampling (m) at which data aliasing occurs for a range of dip angles and frequencies, calculated using Equation 2.13 (Yilmaz, 1987). Grey shaded region denotes angles and frequencies aliased in volumes acquired using 3D Chirp sub–bottom profiler. Panel b) shows a diagrammatical representation of the wavenumber domain equivalent. The black line with slope d_1 remains unaliased for all frequencies. The grey line, however, has a larger dip of d_2, leading to some of the higher frequencies becoming aliased (represented by the dashed grey line).

Assuming a velocity of 1500 ms^{-1}, for 3D Chirp this produces the results shown in Panel a) of Figure 2.7. The highest frequency content (13.0 kHz) of our source sweeps become spatially aliased at dip angles $\geq 13°$, angles $\geq 25°$ for the central frequency of 7.25 kHz, and data remains unaliased at all angles less than 90° for the lowest frequency of 1.5 kHz. However, the source array of four transducers act to beam form the downgoing wavetrain to -3 dB limits of 15° from normal in the cross–track direction, and 30° along–track (Figure 2.8) (Gutowski, 2004). Hence, the steeper dip angles at which the reflected wavefield would become aliased are not illuminated by the source.

Alternatively, it is perhaps more useful to think in terms of the wavenumber domain. Considering a plane wave the gradient of slope d, angular frequency, ω, and wavenumber, k, can be related by the expression

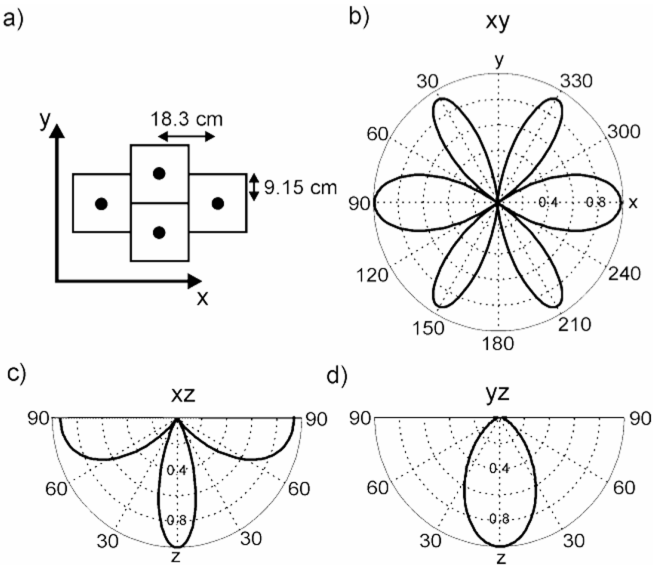

Figure 2.8: Source array directivity calculated for the central frequency of sweeps w13 and w32 (Gutowski, 2004). Panel a) shows the source array configuration, while b), c), and d) the radial dependant amplitude of the downgoing sweep in the horizontal and two orthogonal vertical planes, respectively.

(Biondi, 2007):

$$d = \frac{k}{\omega}. \tag{2.14}$$

Data remains unaliased while $k \leq k_N$, where k_N is the Nyquist wavenumber. Since the Nyquist wavenumber can be defined as $|k_N| = \frac{\pi}{\Delta x}$, Equation 2.14 becomes:

$$|d| \leq \frac{\pi}{\omega_d \Delta x}; \tag{2.15}$$

for given frequency ω_d.

Panel b) of Figure 2.7 shows a diagrammatical representation of aliasing in the wavenumber domain. While the black line, representing data with a dip of d_1, remains unaliased for all frequencies between ω_{min} and ω_{max}, the grey line, representing data with dip d_2, becomes aliased when it moves beyond the Nyquist wavenumber, k_N. Energy in frequencies beyond this, represented by the dashed grey line, is wrapped around to start at $-k_N$, and therefore has an apparent dip of $180 + d_2$ (although, strictly, this energy will not cause aliasing until it overlaps unaliased data).

Data aliasing is the most fundamental type of aliasing, as, if the data is spatially aliased during recording, all subsequent types of spatial

aliasing will be present. This is a particular problem for 3D Chirp data sets, where the limited lateral extent of the mat causes sampling to be highly irregular with lots of small gaps in the coverage, leading to discontinuous spatial sampling. However, as shall be discussed further in **Chapter 4**, small discontinuities in the spatial sampling can be accommodated easily during the imaging process.

2.3.2 Image Aliasing

Image aliasing occurs when the migrated traces in image space are too coarsely sampled in time and/or space to accommodate the imaged stratigraphy. The migration ellipsoid is aliased, leading to gaps appearing in the data, and/or whole wavelets being smoothed over. As the level of image aliasing increases, sections become more ambiguous and harder to interpret, even without the addition of extra noise.

Using the same principles as for Equation 2.15, it is possible to define a similar equation for relating dip, frequency, and spatial sampling in image space for a time migration (Biondi, 2001, 2007):

$$\omega_{\tau}^{\xi} \leq \frac{\pi}{\Delta x_{\xi} \left| d_{x}^{\xi} \right|} \quad , \quad \omega_{\tau}^{\xi} \leq \frac{\pi}{\Delta y_{\xi} \left| d_{y}^{\xi} \right|}. \tag{2.16}$$

where, image space $\xi = (x_{\xi}, y_{\xi}, \tau_{\xi})$, and Δx_{ξ}, Δy_{ξ} and d_{x}^{ξ}, d_{y}^{ξ} are the sample spacing and dip in image space, respectively.

It is important to note that $\omega_{\tau}^{\xi} \neq \omega_{t}$. The seismic wavelet is compressed by some imaging operators (such as Dip Move Out, DMO, and Azimuthal Move Out, AMO), while during the migration process it is stretched. This stretching factor can be defined as $\frac{dt_D}{d\tau_{\xi}}$, where t_D is the time co–ordinate. Thus, Equations 2.16 become:

$$\omega_{t}^{x} < \frac{\pi}{\Delta x_{\xi} \left| d_{x}^{\xi} \right| \frac{dt_D}{dt_{\xi}}} \quad , \quad \omega_{t}^{y} < \frac{\pi}{\Delta y_{\xi} \left| d_{y}^{\xi} \right| \frac{dt_D}{dt_{\xi}}}. \tag{2.17}$$

The choice of sampling parameters in image space are independent of the acquisition geometry, being set arbitrarily as part of the migration algorithm. Therefore, where no data aliasing is observed, image aliasing can be easily avoided by increasing the density of sampling of the migrated ellipsoid. However, higher sampling in image space results in a significant computational cost for the migration operation, meaning that it is often better to limit the dip operators by low–pass filtering during the input phase (Gray, 1992; Claerbout, 2005). Equation array 2.17 allows the apparent dips and sampling intervals in image space to be related to frequencies in the recorded data space, permitting an appropriate filter to be designed.

2.4 Conclusions

In this Chapter, some of the fundamental system parameters have been examined to identify problems and how they may affect data quality. The main findings of this investigation are:

- Erroneous positions, originating from poor quality RTK–GPS strings or bad shot time stamps, will result in vertical and horizontal smearing. These must be removed prior to CMP stack or migration summation.
- Variations in seabed reflector repeatability, due to sea surface ghosts and/or reflections within the frame, may result in problems during migration summation between minimal data sets.
- Irregularities in the spatial coverage result in spatial aliasing of the 3D waveform.

Of all the system characteristics discussed during the course of this Chapter, the problem of spatial aliasing and its subsequent effects on migration is the most important. Data volumes acquired using the 3D Chirp sub–bottom profiler will always suffer from being irregularly sampled in the X,Y plane, and contain large numbers of small gaps in coverage. Traditionally, spatial aliasing effects are removed by careful low–pass filtering, but this results in a rapid decrease in image

resolution (e.g., Yilmaz, 1987). A careful consideration of data regularisation techniques is required in order to reliably migrate 3D Chirp data sets without introducing large numbers of migration artefacts.

In **Chapter 3**, traditional Chirp processing techniques are combined with standard industry approaches for handling irregularly sampled data to process an example volume, providing a baseline of what can be achieved. This is followed in **Chapter 4** with an assessment of the available regularisation methods, and followed by the development of an optimal approach in **Chapter 5**.

"The future is here. It's just not widely distributed yet."

William Gibson (1948–present)

3

Case Study in Small Object Detection

[1] In this chapter I present the results of a survey acquired in an atidal basin on the south coast of England, early 2006.

3.1 Introduction

Detailed (decimetric scale) imaging of the seabed and sub–seabed morphology is crucial in the marine construction industry and homeland defence. Preliminary surveys to identify hazards, such as sudden changes in geology or discrete obstructions, traditionally combine acoustic seabed mapping and divers with sounding poles. Divers are

[1] Chapter published as (author list reflective of relative contributions): Decimeter Resolution 3D Seismic Volume in Shallow Water: A Case Study in Small Object Detection, M.E. Vardy, J.K. Dix, T.J. Henstock, J.M. Bull, and M. Gutowski, **Geophysics**, 73(2), B33-B40, 2008.

heavily constrained by environmental conditions such as water temperature, site depth, currents, tides, and particulate suspension levels (visibility), while even in perfect conditions they can only cover ~ 10 m^2/day and can sample only the top 1.0 m of subsurface. Consequently, there has been much recent work to develop high–frequency surface–scanning acoustics, such as side–scan sonar, sector scanning sonar, and swath bathymetry, for object detection on the seabed (e.g., Simms and Albertson, 2000; Quinn et al., 2002). By comparison there has been limited success in replicating this level of resolution in the sub–surface (Schock et al., 2001; Bull et al., 2005)

Chirp or Boomer sub–bottom profilers (operating in the 0.4 kHz to 24.0 kHz range) are capable of imaging completely buried structures, but they collapse responses from a 3D environment into 2D vertical slices and therefore provide no cross–dip information. Even after migration, the results are imperfect and confusing sections, commonly degenerated by out–of–plane reflections, especially in areas with rapid structural variations. Because of that and the poor ground coverage afforded by a sparse mesh of 2D lines (commonly $\geq$ 10 m spacing), they can do little more than indicate zones with a higher risk. However, when Chirp or Boomer sources are combined with an array of hydrophones to record the reflected waveforms in 3D (Missiaen, 2005; Scheidhauer et al., 2005), it is possible to image buried objects, as shown within along–track sections by Schock et al. (2001).

Sampling the reflected waveform in true 3D and with RTK–GPS positioning, 3D Chirp allows traces to be binned into a geographically orientated 12.5 cm by 12.5 cm grid, forming a high–resolution 3D seismic volume with dip information for all azimuths, and reflections from completely buried structures (Bull et al., 2005). Previous publications have discussed geological (Bull et al., 2005) and engineering (Gutowski et al., 2008) applications. Here, I present the results from a survey acquired in a man–made atidal basin on the south coast of the UK, comparing seismic object identification with comprehensive post–survey dredging.

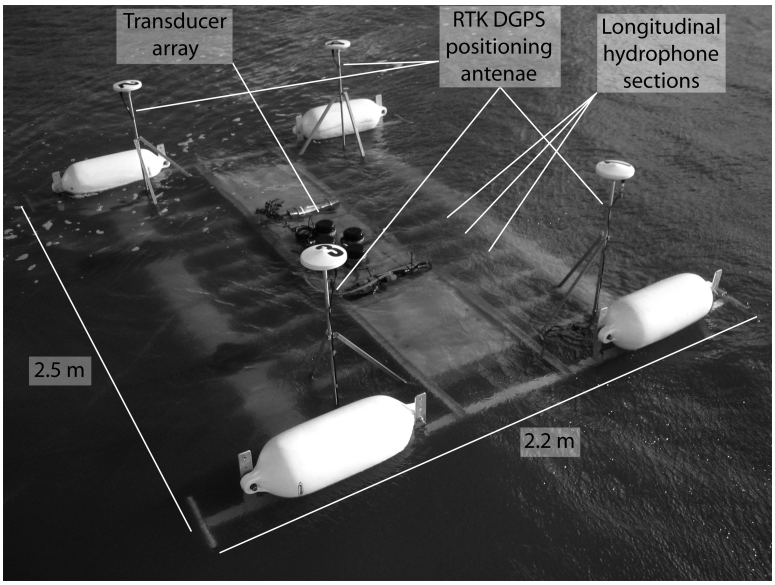

Figure 3.1: Annotated photograph of 3D Chirp sub–bottom profiler. The 60 hydrophone groups, housed in 11 longitudinal sections, are arranged in a 0.25 m by 0.25 m grid around four central transducers. RTK–GPS positioning of each source–receiver pair permits accurate trace binning onto a 12.5 cm by 12.5 cm CMP grid.

3.2 Methodology

The 3D Chirp is a rigid framed high resolution sub–bottom profiler comprising 60 hydrophone groups arranged in a 25 cm by 25 cm grid around a cross of four GeoAcoustics GeoChirp II transducers (Figure 3.1). Navigation is provided by four RTK–DGPS antennae giving positioning accurate to $X = \pm 0.46$ cm, $Y = \pm 0.70$ cm, and $Z = \pm 1.82$ cm (Bull et al., 2005). The waveforms were recorded at a 0.02 ms sampling interval and a horizontal resolution of 12.5 cm by 12.5 cm (Bull et al., 2005). High resolution Chirp sub–bottom profilers use linear electronics to produce a highly repeatable and tuneable swept frequency acoustic impulse capable of providing centimetric vertical resolution and decametric penetration (Schock and LeBlanc, 1990). This allows the source sweep to be tailored to the specific survey requirements (Gutowski et al., 2002). For this survey we used a 16.37

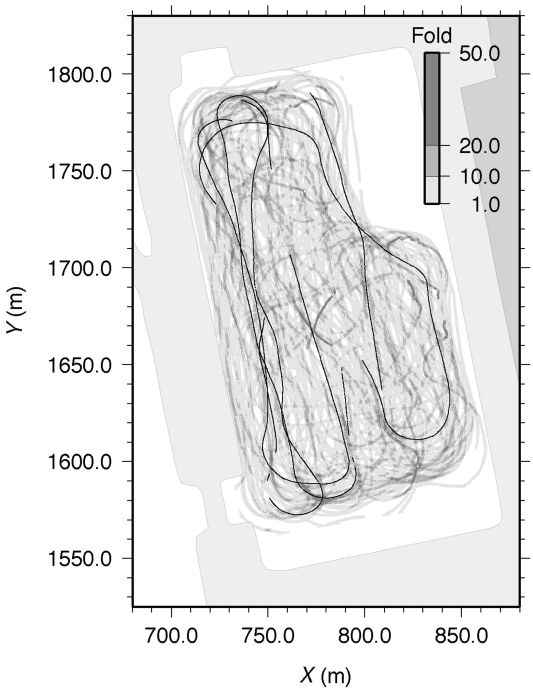

Figure 3.2: Plot of fold coverage, darker colours indicating a greater number of traces in the CMP bin. Overlain black line shows a 5 minute subset of GPS locations, highlighting how the acquisition methodology involves strafing an area repeatedly at various different sail angles. Gaps in line are caused by drops in GPS quality, while shaded grey areas surrounding acquired volume denote the quayside and a nearby building. Distances in X and Y are projected on the WGS84 ellipsoid from an arbitrary local zero.

ms long sweep scanning linearly from 1.5 kHz to 13.0 kHz with a square envelope (see, Table 2.2). The broader bandwidth than traditional sweeps gives improved resolution, while the short sweep length permits high shot rates of six to eight pulses per second.

Bordered by a harbour wall and caisson, the site was 250 m long by 150 m wide and infilled by a thin veneer of fine grained sediment that overlay a bedrock surface composed of middle or upper Devonian slate. At the time of the survey, obstructions in the north–east corner and southern quarter restricted the accessible area to $\sim 23,000$ m^2. However, because the area was closed to all traffic except the survey vessel, sea state conditions were excellent, and the tight space provided few problems.

The 3D Chirp profiler collected more than 20 million traces over two survey days, at a tow distance of 5.0 m behind a small, slow moving (3 knots), vessel while pulsing at six times per second. Lines were acquired at 1.0 m line spacing, providing 95 % ground coverage with no gaps larger than 3.0 m by 3.0 m, and multiple sampling of each grid bin (Figure 3.2). The average fold was 15 traces per 12.5 cm by

12.5 cm bin, but when the system was temporarily stationary, this rose to > 200.

These data were recorded in a raw, uncorrelated format, allowing for a later, more flexible processing strategy. I used a simple processing flow to limit the number of potential processing artefacts which might confuse or disrupt the reflections from discrete targets of particular interest for this application:

i) Correlation of the raw data with the source sweep, thereby reducing all reflections to the Klauder wavelet.

ii) Clean the data by removing any traces with anomalously low S/N caused by bubbles in the water column and/or flotsam caught on system. Using amplitudes extracted from a two–way–traveltime (TWT) window centred on the bedrock horizon, it was possible to automatically scan through the volume removing poor quality traces. In total approximately 8 % of the original data volume was removed.

iii) Deconvolution using a predictive Weiner filter to remove sea surface ghosting of the bedrock reflector (c. 13.9 ms TWT; Figure 3.3). Although, it has previously been argued that the optimum processing of high–resolution Chirp data involves a source signature deconvolution (Quinn et al., 1998), I found a simple predictive Weiner filter to be more effective with this source sweep, without damaging the wavelet.

iv) Filtering using a bandpass filter (0–1500–13,000–15,000 Hz) was employed to remove unwanted high– and low–frequency noise.

v) A 3D pre–stack Kirchhoff time migration implemented by ProMAX was used to move energy back to its correct locations using a velocity of 1400 ms^{-1}, determined as the lower limit of velocities estimated using diffraction hyperbola curvature. That improved the S/N by strengthening the amplitudes of coherent reflectors, and it optimised horizontal resolution to half the receiver spacing (larger than the theoretical limit of $\lambda/4$). Use of the Kirchhoff algorithm also resampled the irregularly positioned data onto a

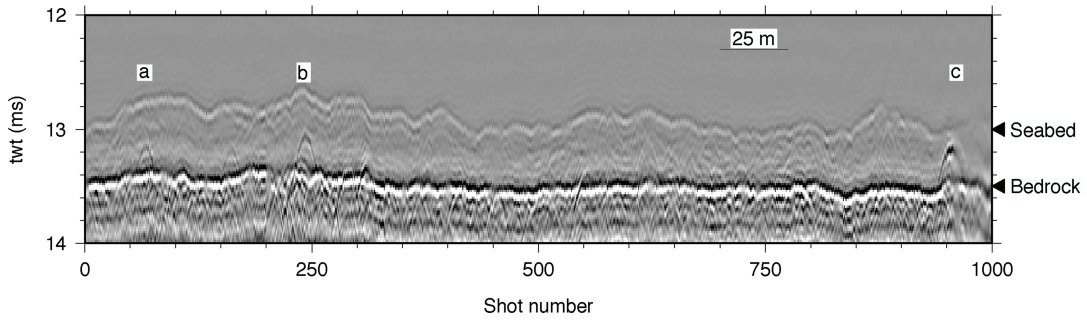

Figure 3.3: Data recorded using channel 23 for an arbitrary section of 1000 shots. Using no processing other than a standard correlation to collapse the swept frequency waveform back to a Klauder wavelet, the seabed and bedrock appear as clean, crisp horizons, and three diffraction hyperbola (labelled a to c) clearly visible in the sediment cover.

regular volume. Given the limited source–receiver offsets of the array and the small thickness of the objects relative to the source wavelength, the migration has a low sensitivity to small–scale fluctuations in the velocity model. Therefore, I made no attempt to account for the objects within the velocity model; rather, a homogeneous velocity was preferred, even when migrating small cubes that included clearly identifiable targets.

Traditional processing of Chirp sub–bottom profiler data involves applying an envelope function as the last processing stage. This removes all phase and polarity information and can cause some vertical smearing, but improves the S/N, especially for weaker horizons. Given the naturally high S/N of these data (Figure 3.3), I chose not to apply the envelope function. This representation of results in their true form and polarity, provides useful discrimination between degraded and non–degraded reflecting objects.

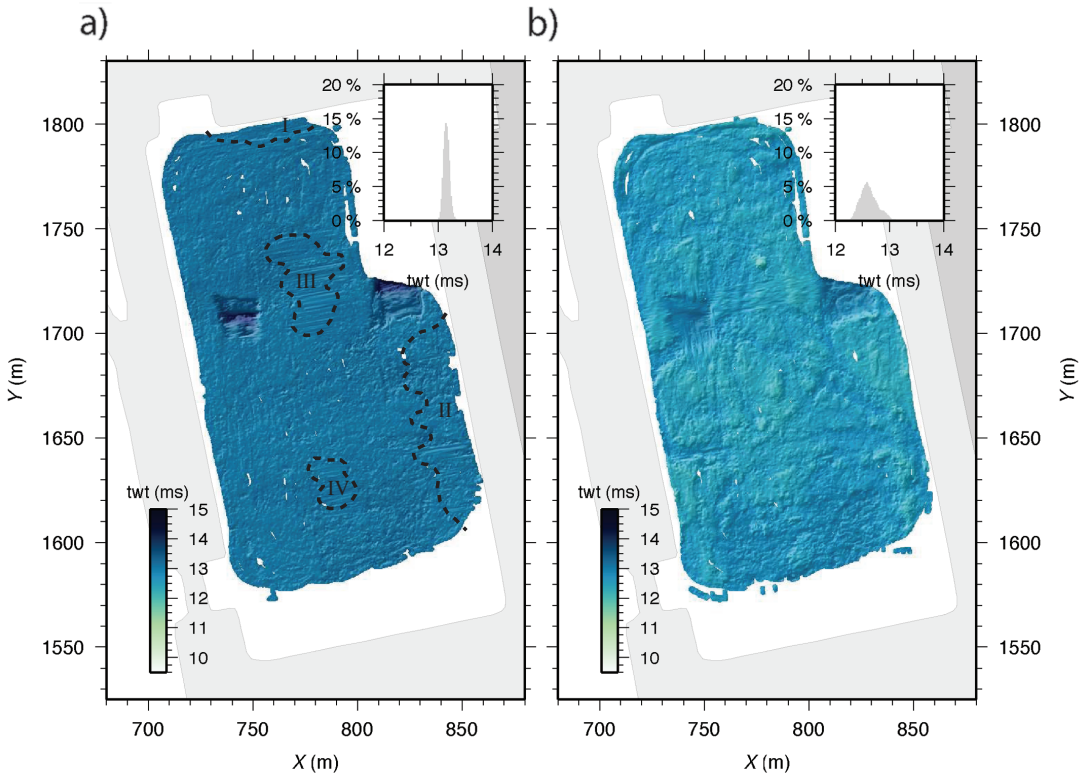

Figure 3.4: Surface maps showing TWT to bedrock, a), and seabed, b), horizons displayed using the same colour scale. Insets show histograms of surface TWT, highlighting the lack of topography, particularly on the bedrock horizon, where 98 % of returns arrive in a 0.3 ms TWT window. Outlines areas labelled I through IV denote zones of discontinuous bedrock reflections (see text for details).

3.3 Seabed and Bedrock Structure

3.3.1 Data Quality & Gross Structure

Within the Chirp seismic volume, two continuous reflection horizons extending across the entire survey area are clearly distinguishable (Figure 3.3). Since the envelope function has not been applied to these data, the seabed and bedrock horizons appear as classic Klauder wavelets with positive (black) side-lobes flanking a negative (white) central peak. The shallowest reflection is the seabed (TWT c. 12.6 ms), which is relatively weak, whereas the deeper slate interface

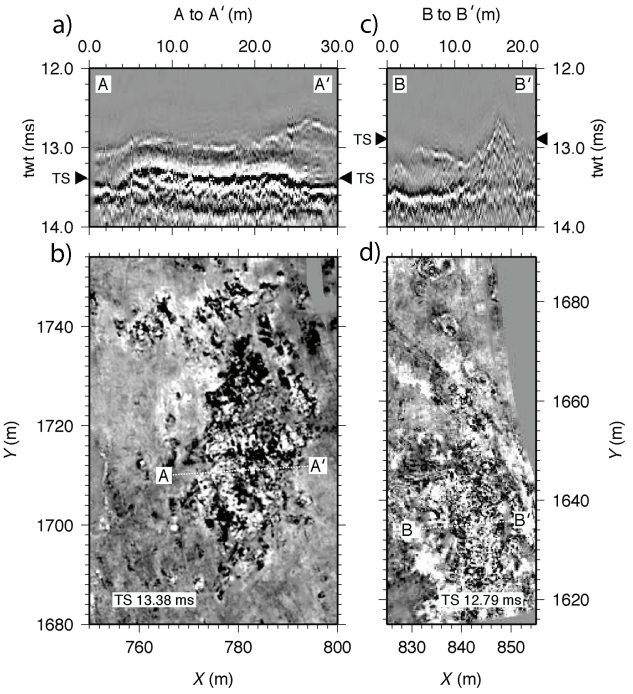

Figure 3.5: a) Vertical section and b) time slice through lower sediments, $\sim$ 0.10 m above the bedrock horizon, of the largest reverse polarity anomaly (zone III). With a maximum extent of 65 m north–to–south and 25 m east–to–west, this horizon covers 1,225 m^2 and displays a broken upper surface with considerably more topography than the overlying seabed. Panels c) and d) show a time slice and vertical section through the zone II anomaly which runs parallel to the eastern boundary of the basin.

(TWT c. 13.2 ms) is a relatively high amplitude reflection.

Using a sound velocity of 1500 ms^{-1}, the higher amplitude, deeper horizon sits at an average depth of $\sim$ 10.4 m below the local datum (defined as the height of the local base station, which is at +55.559 m from the WGS84 geoid), and demonstrates little topography (Figure 3.4a). Except for two discrete depressions (of which only the western is completely imaged), the bedrock surface varies $<$ 0.1 ms ($<$ 0.07 m) forming a gentle north–south gradient of $< 0.2°$.

Across 86 % of the volume, the bedrock surface is easily identifiable, but in four zones the bedrock horizon becomes discontinuous and indistinct (I through IV, Figure 3.4a). In zones I and II, high amplitude returns from an overlying morass of superimposed diffraction hyperbola mask any response from the deeper bedrock (Figure 3.5c and d). Subsequent dredging identified these as piles of waste material (e.g., rope, wire, cables, wood, and tyres) dumped along the basin margin. Similarly, the bedrock is masked zones III and IV by an irregular, reverse–polarity horizon sitting 10 cm to 15 cm above the average bedrock surface (Figure 3.5a and b).

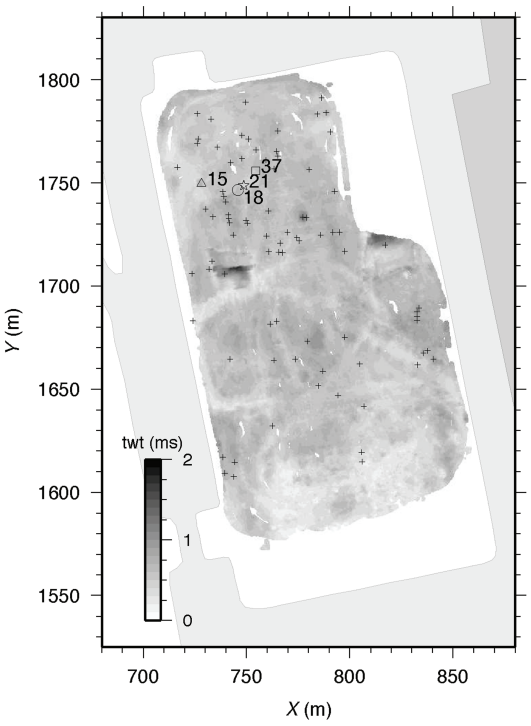

Figure 3.6: Sediment isopach map (TWT), overlaid by crosses marking locations of acoustically identified buried targets. The three objects used as examples for comparing seismic and dredging results in Section 3.4 are identified by their acoustic target number (15, 18, and 37), and a triangle, circle, and square, respectively. Similarly, target 21, used to highlight the advantages of using unmigrated volumes in Figure 3.8, is identified with a star.

The area covered by this latter horizon is 1,225 m^2, the largest zone of which (III) having a maximum extent of 65 m north–to–south and 25 m east–to–west (Figure 3.5a and b). The horizon's asymmetry with seabed topography makes it unlikely to be shallow gas. While, given the low density and thin covering of overbearing sediments, it is difficult to correlate it with a possible source/trap. Similar acoustic signatures have been observed in archaeological sites, where they are commonly associated with low density material such as wood/rope and peat layers (e.g., Quinn et al., 1997a,b; Arnott et al., 2005; Plets et al., 2007). However, the post–survey dredging failed to identify any material. The high amplitudes suggest that, if the horizon is the result of an accumulation of degraded material, it will be heavily degraded, making it probable that the material would have disintegrated in the dredge head.

The weaker, shallower horizon sits at an average depth of $\sim$ 9.1 m, and is consistent with the seabed of unconsolidated, fine–grained sediments described by preliminary diver sorties. Unlike the bedrock, the seabed displays a more irregular topography (Figure 3.4b), causing

the sediment cover to be highly variable (Figure 3.6). The average thickness is 0.76 ms TWT ($\sim$ 0.6 m), but thins to $<$ 0.2 ms TWT ($<$ 0.15 m) in the west and south, and thickens to 1.96 ms TWT ($\sim$ 1.5 m) in the two depressions.

The lack of sediment infill to the south, and presence of partially eroded, relic dredging scour marks is consistent with recorded dredging in the 1980s and 1990s. Other than two discrete depressions, where the sediment thickening is caused by the infilling of bedrock anomalies, several smaller, individual seabed promontories rising up to 0.50 m above the average bed depth. In most cases, these take the form of large diffraction hyperbola (or collections thereof) that protrude into the water column and can be up to 7.0 m in diameter. Dredging confirmed these to be piles of dumped material, commonly tangled conglomerates of rope, wire, hose, and broken chunks of wood. Similarly, to the north and east there are seabed highs, $\sim$ 0.25 m above average depth, which are coincident with the areas where dumped material obscures bedrock returns.

3.3.2 Seabed & Bedrock Depressions

Two anomalous seabed and bedrock depressions measuring $\sim$ 20 m in diameter and 2 ms TWT (c. 1.5 m) below the average bedrock level at their deepest points, are observed centred at X = 740, Y = 1710 and X = 815, Y = 1720 (Figure 3.7). The structures appear to be morphologically defined by the bedrock, with sediment infill mimicking the underlying structure.

The western depression, which is the only one of the two we have complete coverage of, measures 20 m east–to–west and 18 m north–to–south. The sides are steepest to the east and west, dipping at angles of 19° and 20° from the horizontal, respectively (Figure 3.7a and b). The southern is much shallower, 6°, while the northern is stepped. The upper wall slopes down at an angle of 17° from the horizontal, before flattening out into a 5.0 m wide terrace (see Figure 3.7a and b). The lower section slopes down at an angle of 14°, and terminates against

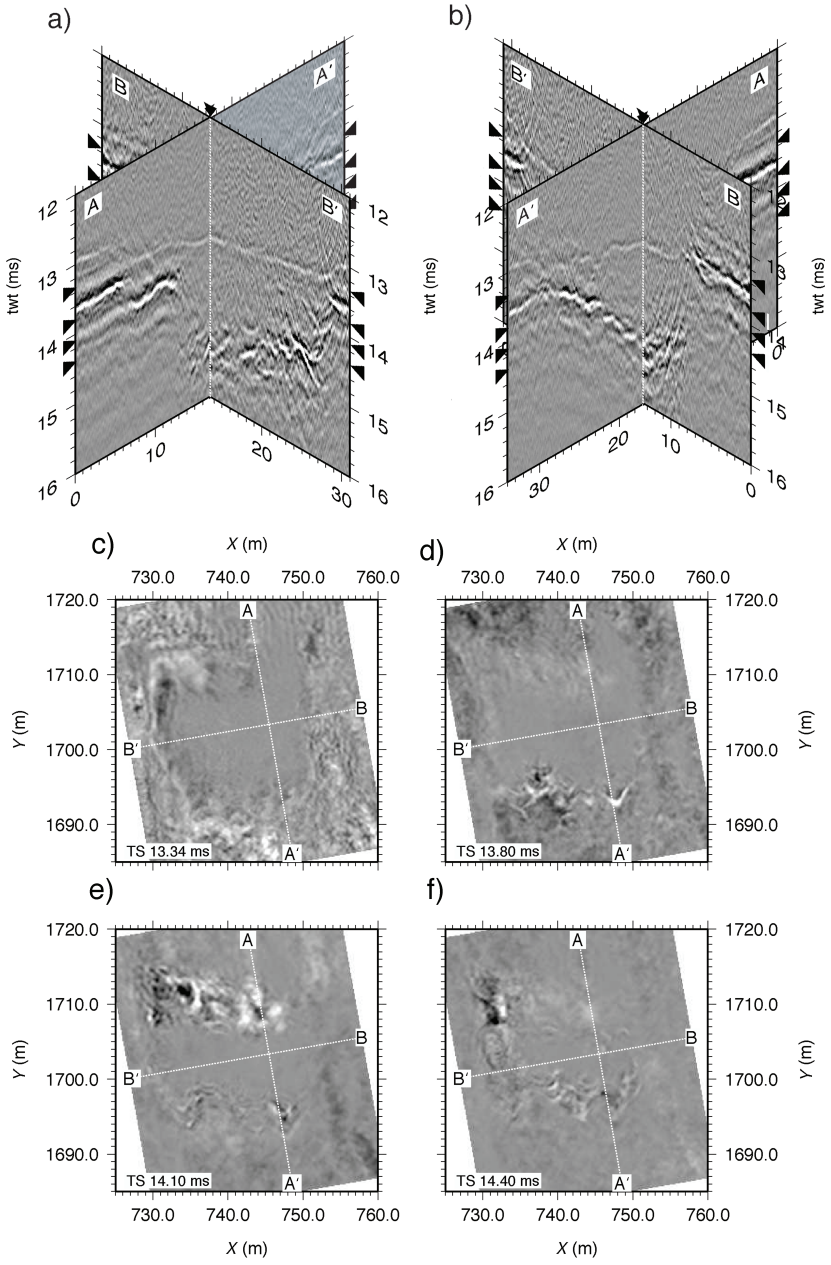

Figure 3.7: Fence diagrams of vertical sections looking from north–west, a), and south–east, b), together with a sequence of timeslices, c) through to f), moving down through the western bedrock depression. Panel c) slices through the lower sediments, 0.15 ms ($\sim$ 0.11 m) above the bedrock surface, showing strong, discontinuous reflections, possibly from ejected debris. Panels d) through f) show the changing shape of the crater with increasing depth; forming a narrow, 15 m long pit floor orientated along an angle of 113°.

the opposite, southern slope, forming the base of the depression. The steep eastern and western boundaries lead to the formation of a linear pit floor, which stretches 15 m at an orientation of 113° from the north–west to the south–east (see, Figure 3.7f), and appears to be a sharp intersection of the dipping northern and southern slopes with little or no shallowing (Figure 3.7a and b).

There is no historical evidence for excavation of two such structures, either as part of the most recent basin developments in the 1950s or before that. World War II Air Raid Warden records note the impact of a large number of high–explosive and incendiary shells having fallen in the vicinity of the surveyed area, while local records also support the possibility of their being bomb craters. This would be in agreement with timeslices through the lower sediments, which show dramatically increased returns in areas surrounding the craters that may be indicative of ejected material (Figure 3.7c). It is not immediately obvious why the depressions are so distinctly square in cross section, although it seems likely to be linked to the slate bedrock fracturing along pre–existing cleavage planes.

3.4 Small Object Identification

3.4.1 Seismic Characteristics

The survey was undertaken to map bedrock structures above the seabed and/or the size and distribution of buried and partly buried objects before targeted dredging. During interpretation of the 3D seismic volume, a set of criteria were used to identify suitable targets for the subsequent dredging – a 'target' being a reflection event that exhibits the distinctive diffraction hyperbolae associated with a local acoustic impedance contrast. Using that methodology, 89 individual targets (black crosses, Figure 3.6) were found in the survey area. Concentrated mainly in the northern half of the basin, some targets appear to be clustered; e.g., the seven that form a line running parallel to the basin margin, 29 m in from the western wall, starting at X =

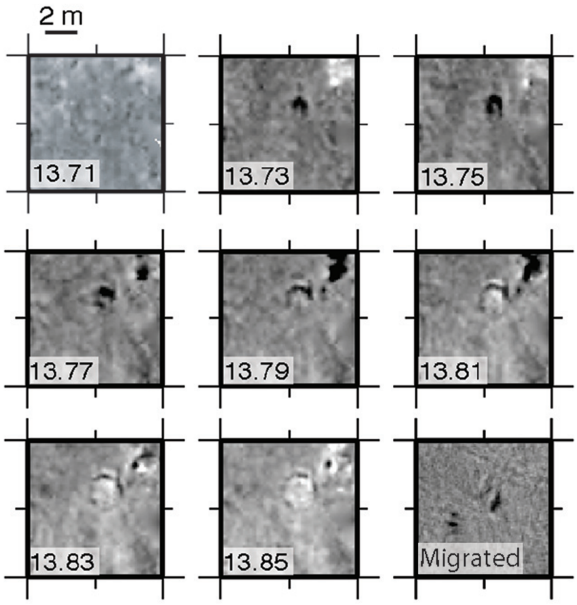

Figure 3.8: Panels showing 10 m by 10 m timeslices moving down from just above and through diffraction hyperbola of seismic target 21 in steps of 0.02 ms. The peak of the hyperboloid, although high amplitude, is small, $\sim 1.0\text{m}^2$, whereas 0.16 ms lower it has opened out into a 3.0 m diameter ring. By cycling up and down through the 3D volume I was able to easily identify buried targets through their coherent diffraction hyperboloids. In comparison, the migrated horizon, final time slice, is less easy to identify as a 'real' target being < 1.5 m^2 in size and extending over ~ 4 time slices.

746 , Y = 1725 and moving north. The targets in the basin range from 0.09 m^2 to 38.5 m^2 in migrated illuminated area, both protrude above the seabed and are completely buried, and demonstrate reverse– and normal–polarities.

Identifying the objects in a migrated volume is extremely difficult as the smallest is just 0.30 m by 0.30 m and so illuminates just 3 bins by 3 bins. In contrast, locating them in unmigrated data is considerably easier as their associated diffraction hyperbola can be up to 7.0 m in diameter (observed on a larger–scale by Hobbs (2003)). Figure 3.8 shows a series of timeslices moving down through the hyperbola of

acoustic target 21 in 0.02 ms TWT steps. The migrated horizon (final time slice, Figure 3.8) covers < 1.5 square metres, or < 9 pixels square, whereas the hyperbola has opened out to form an easily identifiable 3.0 m diameter ring 0.16 ms TWT (~ 0.11 m) below the object. This coherent opening of the diffraction hyperbolae into distinctive ringed structures, provided a method to quickly and effectively identify all objects buried in the basin.

Once each target had been located, small, 25 m square cubes centred on each object were migrated. From this geometrically correct horizon it was possible to extract estimates of object dimensions, together with polarity information that may give an indication of the material nature of the object.

3.4.2 Comparison of Acoustic Targets with Dredging Results

Subsequent to the completion of the 3D Chirp seismic survey, a comprehensive dredging program was undertaken to retrieve all discrete small objects. A 0.66 cubic metre bucket dredge was deployed from a 30 m by 15 m, four–legged dredging platform, with a separate, free–floating pontoon mounted hopper for sieving. Positioning a D–GPS antenna over the pivot point allowed each grab to be located to to an accuracy of ± 2.0 m. However, the use of a bucket grab prevented the acquisition of any orientation information or burial depth.

Due to the possible further development of the basin, it was seen as important that all objects were cleared, so dredging was not guided onto specific seismic targets. Instead, the entire 23,000 m^2 area was cleared systematically, making possible an exhaustive comparison of acoustically identified targets with dredged objects.

All objects recovered during dredging correlated to a coincident acoustic target, and for every target identified during the seismic survey an object of appropriate dimensions was retrieved. To illustrate that agreement between acoustic and dredging results, three examples, seismic targets 15, 18, and 37 (see, Figure 3.6) will be considered:

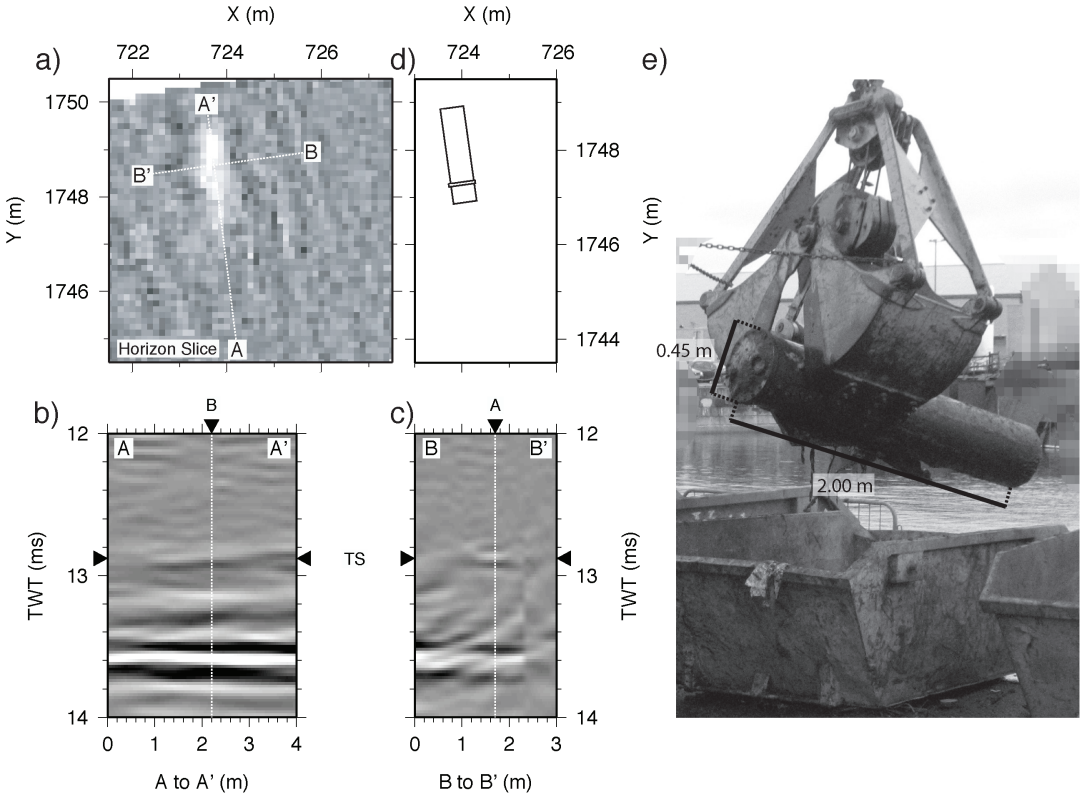

Figure 3.9: Timeslice, a), and vertical slices along–axis, b), and across–axis, c), through the migrated volume centred on acoustic target 15. While panels d) and e) show a location map and photo of the object dredged from this site; a 2.0 m by 0.45 m diameter metal cylinder. Vertical exaggeration 4:1.

3.4.2.1 Target 15

In the migrated volume, target 15 forms a long (2.0 m), narrow (0.3 m), normal polarity horizon (Figure 3.9). Sitting at a depth of 12.90 ms TWT, $\sim$ 0.50 m above the bedrock horizon, it it is contiguous with the seabed and slopes slightly north–to–south at an angle of 2° from the horizontal.

A large metal cylinder, 2.0 m long and 0.45 m in diameter, was recovered from this location (Figure 3.9d and e). Upon closer inspection, the seals of the cylinder had remained intact, there were no significant accumulations of rust, and the object appeared air filled and empty

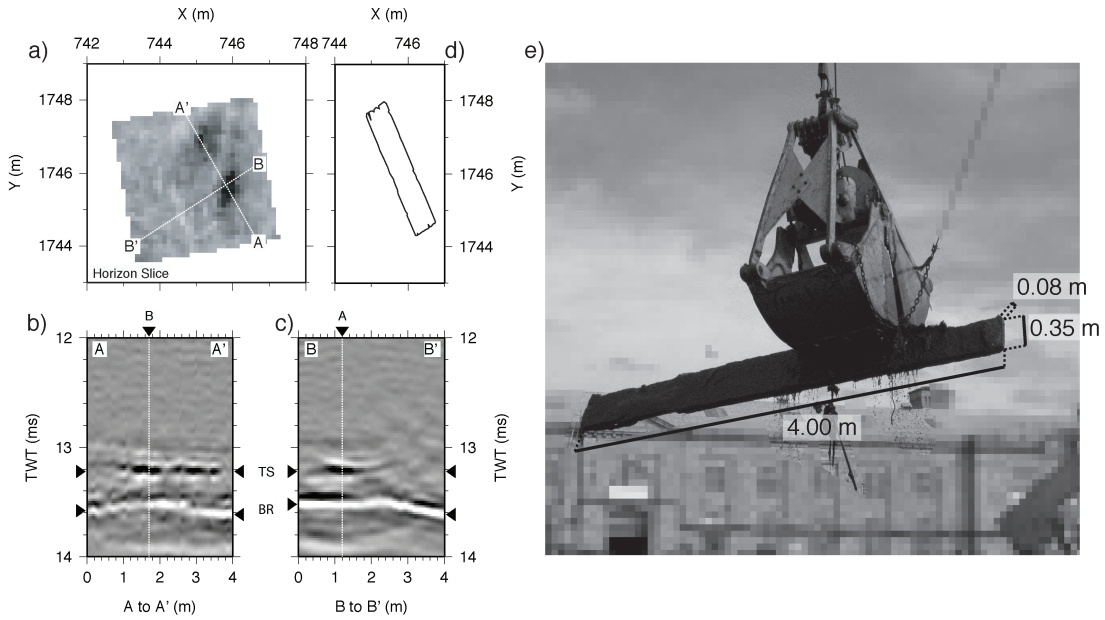

Figure 3.10: Timeslice, a), and vertical slices, b) and c), through acoustic target 18, together with location map and photo, d) and e), of object recovered; a 4.0 m by 0.35 m by 0.08 m heavily degraded wooden plank. BR indicates top bedrock reflector. Vertical exaggeration 4:1.

of liquid. Although the dimensions of the acoustic horizon are an excellent match for those of the recovered object, the horizon is surprisingly low amplitude for a target presenting such a large impedance boundary.

3.4.2.2 Target 18

Acoustic target 18 is a 3.8 m long, 0.75 m wide, reverse polarity event that sits at an average depth of 13.22 ms TWT, $\sim$ 9.3 m. As with target 15, it is not flat, rather it dips south–to–north at an angle of 0.5° from the horizontal. The vertical sections (Figure 3.10b and c) provide a better indication of the size and shape of the migrated horizon, while its reversed polarity suggests it is a wooden object, probably degraded (e.g., Quinn et al., 1997a,b; Arnott et al., 2005; Plets et al., 2007).

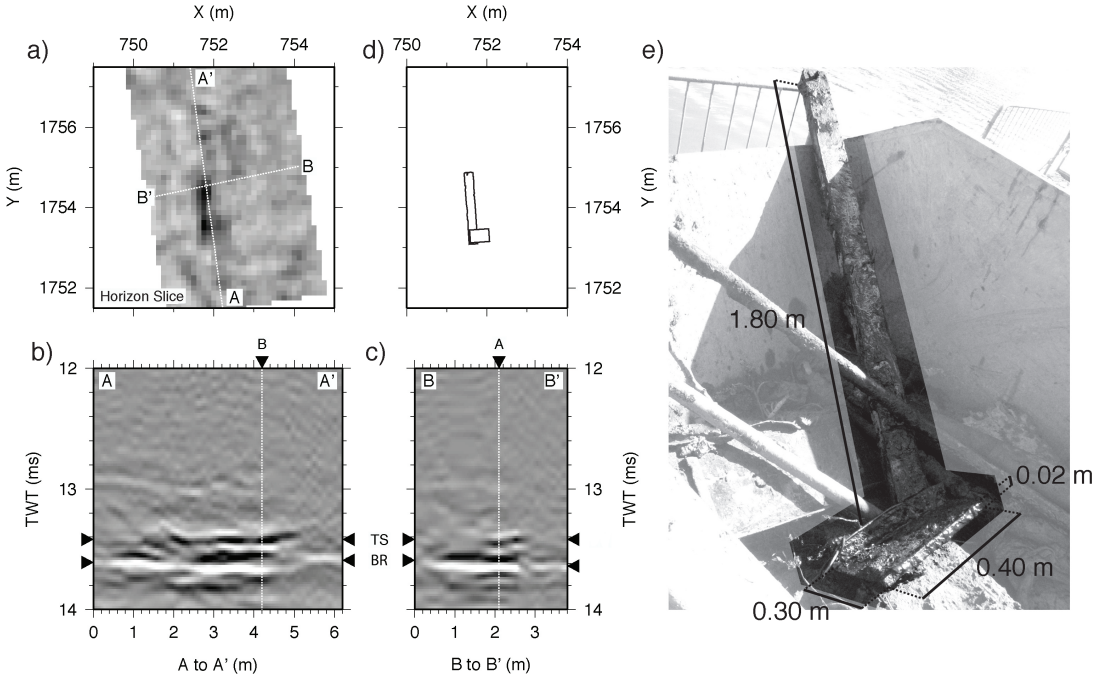

Figure 3.11: Timeslice, a), and vertical slices, b) and c), through acoustic target 37. Panels d) and e) show location map and photo of the 1.80 m by 0.13m by 0.10 m wooden pole and attached 0.40 m by 0.30 m metal sheet found during dredging. BR indicates top bedrock reflector. Vertical exaggeration 4:1

At this location a 4.0 m long, 0.36 m wide, and 0.08 m thick wooden railway sleeper was found (Figure 3.10d and e). Heavily degraded, the wooden railway sleeper broke apart when it landed in the hopper, and again upon transferral to a skip, making it an good match in both size and composition for the observed acoustic target.

3.4.2.3 Target 37

Target 37 is an anomalously shaped 1.8 m long, high amplitude horizon (Figure 3.11). For most of its length it remains consistently 0.5 m wide, but broadens to 1.0 m to the south. The peak of the Klauder wavelet is 0.25 ms TWT , $\sim$ 0.18 m, above that of the bedrock, and runs parallel along a shallow south–to–north gradient of 0.5° from the horizontal. Similar to target 18, it is polarity reversed, which

we would expect to indicate an object composed of wood, probably degraded.

The object found here was a 0.10 m wide by 0.13 m thick by 1.8 m long wooden pole, attached at one end to a 0.40 m by 0.30 m metal plate with 0.02 m high raised edges (Figure 3.11d and e). Upon closer inspection, the wooden bar was badly degraded with large chunks being easily broken free. Interestingly, at no point does the the acoustic horizon revert to normal polarity, even though the shape and dimensions (Figure 3.11a) agree extremely well with the retrieved object.

3.5 Discussion

The results demonstrate an excellent correlation between the observed seismic reflection event and the recovered object. A key factor in achieving this lies in the processing of the data. For example, in the unmigrated volume surrounding target 18, the horizon disappears into a data gap to the south, meaning that the peak of the diffraction hyperbola is only ~ 2.5 m in length. Post–migration, the hyperbola has been collapsed back to a horizon of similar length to the coincident object, highlighting the advantage of using a 3D Kirchhoff migration to resample the data onto a regular grid.

The amplitudes of the seismic horizons, whether migrated or otherwise, cannot simply be taken as a proxy for material properties of the object. The dimensions of the targets cause waveforms from upper and lower surfaces to interfere. As Widess (1973) discussed when thinking in terms of thin beds in multi–channel seismic data, this can dramatically reduce the amplitude and alter the shape of the reflected wavelet. The anomalous amplitude of target 15 is therefore likely to be a result of the thickness of the metal sheeting being substantially less than the wavelength.

Similarly, for target 37, as the plate is attached to the pole, the two would not be resolvable into two distinct sources, making the resulting horizon a combined response from both. Since the metal plate

is < 0.01 m thick the acoustic response will suffer from destructive interference in the same manner as the metal cylinder found at the site of target 15, leading to the reflected horizon being dominated by the response from the wooden pole. This agrees with the horizon becoming lower amplitude to the south.

3.6 Conclusions

I have presented the results of a survey in an atidal basin on the south coast of UK, using the 3D Chirp high–resolution sub–bottom profiler. The data permitted detailed mapping of seabed and bedrock structure in 3D, and the acoustic identification of 89 discrete buried targets. Except for the acoustic anomaly labelled zones II and IV, subsequent post–survey dredging confirmed a 100 % success rate in identifying buried objects, and showed a strong correlation between observed acoustic signature and object size.

With these results I have demonstrated that:

- The 3D Chirp sub–bottom profiler is capable of acquiring coherently imaged true 3D volumes with decimetre horizontal and centimetre vertical resolution.
- The effect of systematic noise present within the data, such as sea–surface ghosting, can be effectively minimised using predictive Wiener filtering.
- It is possible to correct for the irregular and incomplete areal sampling of the data by using a 3D pre–stack Kirchhoff time migration.

However, they also indicate a number of limitations with employing standard processing approaches to 3D Chirp volumes:

1. Pre–stack 3D Kirchhoff migration (using the ProMAX algorithm) is not a viable solution for 3D imaging a whole 3D Chirp volume. Migrating the 25 m by 25 m by 18 ms cubes centred on each object took between 24 and 36 hours, depending on trace densities. To

migrate the entire data set (which, given the short trace lengths, is not overly large) would take more than 23 days of solid processing on a 8 core workstation with 16 GB of RAM.

2. A post–migration filtering technique is needed to remove migration artefacts caused by spatial aliasing of the data in regions of steeply dipping topography (e.g., western and eastern boundaries of the crater). If this structure were deeper these artefacts could lead to misinterpretation of overlying features.
3. Automated programs need developing for the removal of traces with bad timing, positioning, and anomalous amplitudes. Although time–gated amplitude filtering was primarily used for the latter, timing and positioning errors were largely filtered by hand. As data sets become larger this becomes increasingly unfeasible, and unnecessarily lengthens the processing time.

These three key limitations are listed in order of importance. Although Normal Move–Out (NMO) stacked volumes are extremely useful for identifying discrete targets (e.g., Figure 3.8), for accurate geological/structural interpretation and to handle irregularities in the spatial coverage it is necessary to produce 3D imaged volumes.

"This is called practice, but remember first to set forth the theory."

Leonardo da Vinci (1452–1519)

4

3D Imaging

The juxtaposition of recorded time series into a CMP binned 3D seismic volume makes the fundamental assumption that all energy recorded on that trace is the result of a simple ray path between the source and receiver via their geometric mid–point. In an Earth model comprising a series of flat, horizontal layers with a homogeneous velocity field such an assumption holds, and the relative orientations of reflectors are representative of the geological cross–section. However, in a more realistic Earth model in which layering dips at a variety of angles, the velocity field can vary on small spatial scales, and discrete reflectors (such as ore deposits, boulders, or ordnance, etc.) and/or discontinuities in reflectors are common, the assumption of pure mid–point reflection fails. In these scenarios, dipping reflectors appear to have shallower dip angles, while discrete objects and discontinuities are represented by large diffraction hyperbolae (Figure 4.1).

The final step in seismic data processing moves dipping reflectors to their 'true' subsurface position and collapses diffraction hyperbola

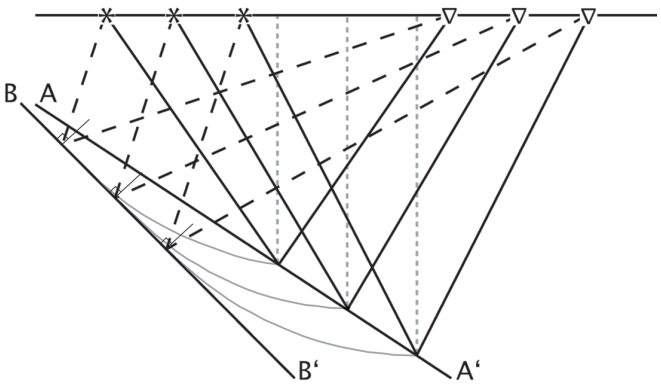

Figure 4.1: CMP binning of non-zero offset data maps energy from the dipping reflector along the line A→A' via solid ray paths (from source, $*$, to receiver, ∇), while the real reflector location, line B→B' mapped by dashed ray paths, is steeper dipping and located at deeper depth (although, note the actual reflection locations are shallower).

using a mathematical process called migration. As by–products of this, a correctly implemented migration will also suppress incoherent noise, thereby improving vertical resolution and S/N.

In this chapter, a number of basic approaches to seismic imaging are discussed, and their suitability for use in the migration of 3D Chirp volumes considered using a combination of theory and the imaging of synthetic seismograms. Initially the basic principles of migration are defined, detailing how a variety of common methods are used for 3D imaging of the pre–stack and post–stack wavefields. The ability of these methods to replicate the reflected wavefields within the 3D Chirp sampling constraints is then weighted against the computational expense. Finally, suitable methods for pre– and post–stack imaging are compared using synthetic data generated using the phase screen forward modelling code of Wild and Hudson (1998) to test their effectiveness against typical acquisition artefacts, and a subset of the volume discussed in **Chapter 3**.

4.1 Migration Theory

The fundamental principles of migration were defined geometrically by Hagedoorn (1954), although investigations into diffraction patterns had been conducted considerably earlier (e.g., see Hilterman, 1970). Hagedoorn (1954) defined migration as the movement of energy along curves of maximum convexity, in effect curves of equal travel time. This principle forms the basis of more advanced migration approaches, which are derived from a robust mathematical treatment of the Huygen's Principle (or, Huygen's–Fresnel Principle) for analytical solution using a computer algorithm rather than wave propagation charts (Trorey, 1970). Although some people still refer to certain migration methods as 'wave equation migration', in reality all migration methods used today solve a form of the wave equation, what differs is their chosen method to accomplish this (Yilmaz, 1987).

With the 3D Chirp system we sample only very short source–receiver offsets ($<$ 1.5 m) and beam–form (caused by the directivity of the source array) a narrow, downward propagating source sweep (-3 dB $<$ 30° from normal along–track and 15° across–track; Gutowski (2004)). Hence, only normal incident or near–normal incident reflections need considering, and the conversion of compressional waves into shear waves can be neglected. This allows the seismic wavefront to be considered using a general form of Hooke's Law, where the pressure, p, is equal to the product of the bulk modulus, K, and deformation (expressed in terms of displacement, $\mathbf{u}$) of the host medium (Claerbout, 1970):

$$p = -K\nabla.\mathbf{u}. \tag{4.1}$$

Newton's Second Law of motion allows the pressure gradient at the wavefront to be related to the product of acceleration and density, ρ:

$$\rho\frac{\partial^2\mathbf{u}}{\partial t^2} = -\nabla p. \tag{4.2}$$

By taking the second time derivative of Equation 4.1, we find:

$$\frac{\partial^2 p}{\partial t^2} = -K\nabla\frac{\partial^2 \mathbf{u}}{\partial t^2}. \tag{4.3}$$

Both Equations 4.2 and 4.3 are now in terms of acceleration, allowing them to be combined:

$$\begin{aligned}\frac{\partial^2 p}{\partial t^2} &= K\nabla\frac{\nabla p}{\rho}, \\ &= \frac{K}{\rho}\nabla^2 p - \frac{K}{\rho}\nabla p_0\frac{\nabla\rho}{\rho}.\end{aligned} \tag{4.4}$$

Since velocity $v = \sqrt{K/\rho}$, as long as the second term is ~ 0 (i.e., $\nabla\rho = 0$), Equation 4.4 can be re–arranged to form a homogeneous approximation of the wave equation:

$$\boxed{0 = \nabla^2 p - \frac{1}{v^2}\frac{\partial^2 p}{\partial t^2}.} \tag{4.5}$$

Here, the propagation of the compressional wave is described in terms of the the scalar, p, and hence is referred to as the 'Scalar Wave Equation'. A general solution to Equation 4.5 takes the form (Claerbout, 1970):

$$p = \left(p^+(x,y,z)e^{imz} + p^-(x,y,z)e^{-imz}\right)e^{-i\omega t}; \tag{4.6}$$

where p^+ and p^- are the downgoing and upgoing wavefronts, respectively, with wave vector component m in the z–direction.

In migration we assume that 'reflectors exist at points in the Earth where the first arrival of the downgoing wavefront is coincident with an upgoing wavefront' (Claerbout and Doherty, 1972), allowing us to reconstruct an image of the subsurface by projecting the upgoing wavefield, which is recorded by the hydrophones, back down into the Earth.

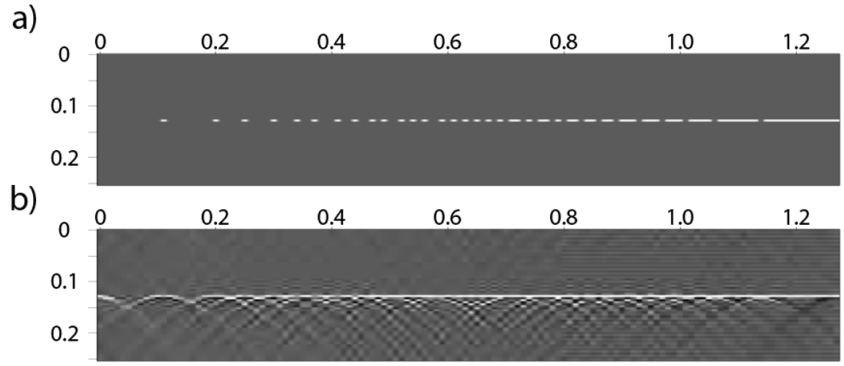

Figure 4.2: Panel a) shows a barrier with holes, and b) the wavefield as recorded beyond the barrier. As long as the condition $z >> \Delta x$ is satisfied, the Huygen's secondary sources superimpose to produce a vertically propagating plane wave. Figure from Claerbout (2005).

4.1.1 Post–Stack Migration

When considering the relationship between the reflection event location on a seismogram and the true location of the corresponding acoustic impedance contrast, there are two factors which cause the apparent position to differ from the true position: the physical survey geometry, i.e. source and receiver offset; and endemic properties such as the interface dip angle and the velocity field (Claerbout, 2005). Traditionally, these two parameters are considered independently, using NMO and stacking to correct for the offset component, leaving the imaging algorithm to adjust for dip on this zero–offset volume (e.g., Judson et al., 1980; Schultz and Sherwood, 1980).

Such post–stack migration algorithms are computationally very efficient, since: the post–stack wavefield is 3–dimensional ($p(x, y, t)$); is typically evenly sampled in x and y; and the stacking process reduces the number of input traces by a factor of the average fold. They are, also, more robust in low S/N environments due to the statistical S/N increase during stacking. In addition, CMP stacking of the data onto a regular grid allows the traces to be migrated together by simulating a continuous wavefield rather than a series of discrete overlapping

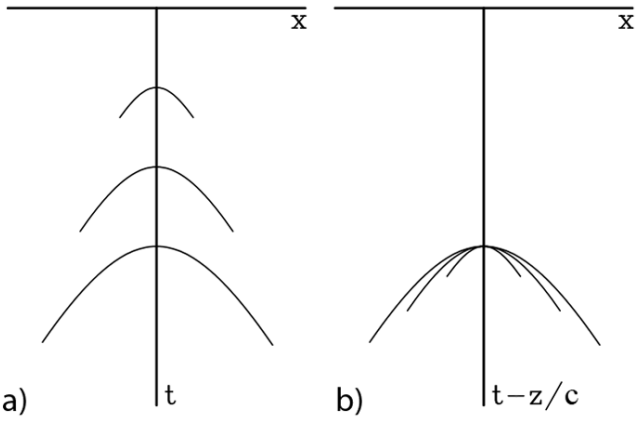

Figure 4.3: Illustration of hyperbola superposition when a wavefront imaged at three different times, a), is translated into a downward continued reference frame with retardation time $t' = t - z/c$, b). Image adjusted from Claerbout (2005).

wavefields that sub–sample the 3D volume (Vermeer, 2002).

4.1.1.1 Migration by Downward Continuation

Due to source/receiver reciprocation, in a zero–offset volume each CMP location can be thought of as an individual Huygen's secondary source. Therefore, as long as the condition $z >> \Delta x$ and Δy (relating depth z with horizontal sampling intervals Δx and Δy) is met, the wavefields can be modelled as vertically propagating plane waves (Figure 4.2).

This allowed Claerbout (1970, 1971) to introduce frequency–domain techniques for performing the downward propagation of the upgoing wavefield based on plane wave solutions to Equation 4.5. Although revolutionary (being the first attempt at using computational solutions to the wave equation for imaging), this approach is relatively inefficient. Instead, Claerbout and Doherty (1972) demonstrated a time–domain approach where the scalar wave equation is translated into a reference frame moving upwards at velocity c (half the sub–surface velocity), thereby minimising the effort involved in the downward propagation. Setting the wavefield in a reference frame moving at velocity c, means that wavefronts will not move relative to the vertical, retardation time axis during downward continuation. With the hyperbola peaks remaining stationary, the residual motion is therefore merely a change of shape (Figure 4.3).

Using the exploding reflector model, such that t is the one–way traveltime, then a plane wave propagating at angle θ can be described by the equation:

$$p(x, y, z, t) = Be^{i\omega(t-(x/c)sin\theta-(z/c)cos\theta)}; \tag{4.7}$$

where c is half the sub–surface velocity and/or the velocity of the moving reference frame.

By considering only small angles of θ, this can be simplified using the expansions $sin\ \theta \approx \theta$ and $cos\ \theta \approx 1 - \frac{1}{2}\theta^2$. Giving:

$$p(x, y, z, t) = Be^{i\omega(t-x\theta/c-z/c+z\theta^2/2c)}. \tag{4.8}$$

The translation from stationary to moving reference frame involves the co–ordinate transformations of wavefront $p(x, y, z, t)$ to $p'(x', y', z', t')$, using:

$$x' = x, \qquad y' = y, \qquad z' = z, \qquad t' = t - \frac{z}{c}.$$

Equation 4.8 now becomes:

$$p'(x, y, z, t') = Be^{i\omega(t'-x\theta/c+z\theta^2/2c)}. \tag{4.9}$$

The array of transform equations also give the vertical propagation of the wavefield in the non–moving reference frame in terms of a shifted version of those in the moving reference frame:

$$\frac{\partial^2 p'}{\partial z^2} = \frac{\partial^2 p'}{\partial z'^2} - \frac{2}{c}\frac{\partial^2 p'}{\partial t' \partial z} + c^{-2}\frac{\partial^2 p'}{\partial t'^2}. \tag{4.10}$$

Substitution into the scalar wave equation gives a transformed scalar wave equation:

$$\frac{\partial^2 p'}{\partial x^2} + \frac{\partial^2 p'}{\partial y^2} + \frac{\partial^2 p'}{\partial z^2} - \frac{2}{c}\frac{\partial^2 p'}{\partial t' \partial z} = 0. \tag{4.11}$$

The final term in Equation 4.11, $-c^{-2}\frac{\partial^2 p'}{\partial t'^2}$, is proportional to a Doppler shift in the frequency of the upgoing and downgoing wavefields (to lower and higher frequencies) by the transformation into a moving reference frame. This can be dropped to eliminate the downgoing wavefield, but at the cost of limiting the velocity accuracy to 1 % at a dip angle of 15 degrees (Claerbout and Doherty, 1972). This leads to the so–called '15 degree wave equation':

$$\frac{\partial p}{\partial z} = \frac{c}{-2i\omega}\left(\frac{\partial^2 p}{\partial x^2} + \frac{\partial^2 p}{\partial y^2}\right). \tag{4.12}$$

Equation 4.12 is a second order approximation of the three–dimensional scalar wave equation, called the parabolic wave equation (Claerbout, 1970). Differentiation of Equation 4.12 with respect to z, and substitution back into Equation 4.11 gives a better approximation, capable of imaging up to a maximum dip of 45 degrees. In the 2–dimensional case, Claerbout (1970) use this method to derive the '45 degree' equation:

$$\boxed{\frac{\partial^3 p}{\partial x^2 \partial t'} - \frac{c}{2}\frac{\partial^3 p'}{\partial x^2 \partial z} - \frac{2}{c}\frac{\partial^3 p}{\partial x \partial t'^2} = 0.} \tag{4.13}$$

The first two terms of Equation 4.13 accommodate the shift and thin lens terms of the wavefield propagation, both of which can be solved analytically. The third term, the diffraction term, accounts for non–normal incident reflection. This is complicated, but can be efficiently solved using the finite difference method, whilst simultaneously stepping through the analytical solutions for the other two terms (Claerbout and Doherty, 1972).

Although equations including more accurate expansions of $sin\ \theta$ and $cos\ \theta$ for Equation 4.8 have been derived (Claerbout, 2005), the imaging to steeper dips ($\geq 45°$) comes with increased computational cost. This 45 degree equation forms the basis of Finite–Difference Migration, which has been shown to be a robust post–stack imaging technique, even in low S/N environments. By keeping data in the time–domain, laterally and vertically inhomogeneous velocity fields can be

correctly implemented, as long as reflector dips are shallower than 45 degrees (Yilmaz, 1987). However, staying in the time-domain makes solving the diffraction term computationally expensive, particularly in 3–dimensions (Robinson and Durrani, 1986).

An alternative approach is to work in the Fourier–domain (Gazdag, 1978). Assuming that a time series $f(t)$ is composed purely of harmonics, the contribution at time $t + \Delta t$ can be extrapolated from time t by working in the frequency–domain. This is described by the equation:

$$p(t + \Delta t) = \int_{\omega} F(\omega) e^{i\omega \Delta t} d\omega. \tag{4.14}$$

Using this principle, it is possible to relate the data recorded at the surface, $p(x, y, z = 0, t)$, to the reflector geometry, $p(x, y, z, t = 0)$.

$$p(x, y, 0, t) = \int_{k_x} \int_{k_y} \int_{k_z} P(k_x, k_y, k_z, 0) e^{i(k_x x + k_y y + \omega t)} dk_z dk_y dk_x, \tag{4.15}$$

similarly:

$$p(x, y, 0, t) = \int_{k_x} \int_{k_y} \int_{\omega} P(k_x, k_y, 0, \omega) e^{i(k_x x + k_y y + \omega t)} d\omega dk_y dk_x. \tag{4.16}$$

Equating Equations 4.15 and 4.16 provides an fundamental relationship between the migrated and recorded wavefields in the Fourier–domain.

$$P(k_x, k_y, k_z, 0) = P(k_x, k_y, 0, \omega) \frac{dk_z}{d\omega}. \tag{4.17}$$

Hence, in the frequency–domain, the migrated data, $P(k_x, k_y, k_z, 0)$, can be calculated from the product of the observed data, $P(k_x, k_y, 0, \omega)$, and a dispersion term. So, given an estimate of the dispersion, the transformation from observed to imaged data is straight–forward.

To obtain this dispersion term, we start with the Fourier transform of the wavefield $p(x, y, z, t)$, which we know equates to:

$$p(x, y, z, t) \leftrightarrow P(k_x, k_y, k_z, \omega) = \int_{k_x} \int_{k_y} \int_{k_z} \int_{\omega} p(x, y, z, t) \; e^{-i(k_x x + k_y y + k_z z + \omega t)} dx \; dy \; dz \; dt. \tag{4.18}$$

The Standard Derivative Theorem of Fourier transforms enables us to express Equation 4.18 as a family of differential equations:

$$\begin{aligned} \frac{\partial^2 p}{\partial x^2} &\leftrightarrow (i\omega)^2 p(k_x, y, z, t), \\ \frac{\partial^2 p}{\partial y^2} &\leftrightarrow (i\omega)^2 p(x, k_y, z, t), \\ \frac{\partial^2 p}{\partial z^2} &\leftrightarrow (i\omega)^2 p(x, y, k_z, t), \\ \frac{\partial^2 p}{\partial t^2} &\leftrightarrow (i\omega)^2 p(x, y, z, \omega). \end{aligned} \tag{4.19}$$

Substitution of these into the 15 degree equation (Equation 4.12) provides an approximation of the dispersion term:

$$\frac{dk_z}{d\omega} = \frac{-ic^2(k_x^2 + k_y^2)}{8\omega}; \tag{4.20}$$

therefore:

$$P(k_x, k_y, k_z, 0) = \frac{-ic^2(k_x^2 + k_y^2)}{8\omega} P(k_x, k_y, 0, \omega). \tag{4.21}$$

A more accurate estimate, based on the 45 degree equation (Equation 4.13), is (Gazdag, 1978):

$$\boxed{I(\xi) = P(k_x, k_y, k_z, 0) = i\omega \left[1 - \frac{c^2(k_x^2 + k_y^2)}{4\omega^2}\right] P(k_x, k_y, 0, \omega).} \tag{4.22}$$

Working in the frequency–domain, imaging is considerably faster than using the time–domain finite difference methods, whilst using the downward continued frequency–domain means vertical velocity variations are implicitly included. Lateral velocity gradients, however, are considerably harder; the selective over– and under–migrating of spatial subsections using slightly higher or lower velocities than is correct allows a weak lateral velocity gradient to be approximated. Another issue of working in the frequency domain is the wrapping around of energy between the Nyquist limits k_N and $-k_N$, which commonly introduces steeply dipping, high–frequency noise (Claerbout, 2005).

4.1.1.2 Frequency–Wavenumber Migration

An alternative to migration by downward continuation of the wavefield, involves translating the full scalar wave equation into the frequency–wavenumber domain (Stolt, 1978). As with phase–shift migration, it is assumed that the wavefield can be represented by harmonics, such that the relationship between $p(x, y, z = 0, t)$ and $p(x, y, z, t = 0)$ is represented by Equation 4.14. In this manner, the wavefield in the Fourier–domain can be estimated as a multiplication of the original data and a dispersion term (Equation 4.17).

For f–k migration, the dispersion term, $\frac{dk_z}{d\omega}$, is estimated by differentiation of the dispersion relation for the full scalar wave equation. This can be obtained in the same manner as for phase–shift migration; by substituting Equation Array 4.19 into the scalar wave equation (Equation 4.5).

$$\omega^2 = v^2(k_x^2 + k_y^2 + k_z^2). \tag{4.23}$$

Differentiation of this leads to:

$$\frac{dk_z}{d\omega} = \frac{v^2 k_z}{k_z^2 + k_x^2 + k_y^2}; \tag{4.24}$$

giving:

$$\boxed{I(\xi) = P(k_x, k_y, k_z, 0) = \frac{v^2 k_z}{k_z^2 + k_x^2 + k_y^2} P(k_x, k_y, 0, \omega).} \qquad (4.25)$$

In this way, the Fourier–domain equivalent of unmigrated time sections can be translated from $P(k_x, k_y, 0, \omega) \rightarrow P(k_x, k_y, k_z, 0)$, before an inverse Fourier transform translates the migrated section back into the spatial–domain.

Using the dispersion relation for the full scalar wave equation, rather than the parabolic wave equation of Claerbout and Doherty (1972), enables dips of any angle to be migrated correctly and quickly (since the multiplier in Equation 4.25 can be solved analytically) within spatial aliasing limits (Stolt, 1978). As with the phase–shift migration, energy wrap–around or incorporating an inhomogeneous velocity model introduce errors. However, unlike the phase–shift migration, using the scalar wave equation dispersion term means that vertical velocity gradients are not implicitly included. To solve this, Stolt (1978) introduced the 'Stolt Stretching Factor' which approximates time–dependant velocity variations by stretching the time–domain, but lateral gradients cannot be accommodated in the same way without introducing sampling issues into the Fourier transform. As before, selective over– and under–migration of subsets is the only solution.

4.1.2 Pre–Stack Migration

Post–stack migration algorithms are computationally very efficient, the wavefield being only 3–dimensional ($p(x, y, t)$). The pre–stack wavefield, in contrast, is 5–dimensional ($p(x_s, y_s, x_g, y_g, t)$), and is consequently significantly more expensive to solve.

NMO, however, is a very simple approximation of the wave equation. Pythagorean theorem is used to get travel–time, t, as a function of

offset, h (Yilmaz, 1987).

$$t^2(x) = t^2(0) + \frac{h^2}{v_N^2}; \tag{4.26}$$

where v_N is an estimate of the acoustic velocity.

From this, a time shift can be calculated and applied to each sample on the trace, thereby approximating a shift to zero–offset.

$$\Delta t_N = t(x) - t(0) = t(0) \left[\sqrt{1 + \left(\frac{h}{v_N t(0)} \right)^2} - 1 \right]; \tag{4.27}$$

Typically approximated to:

$$\Delta t_N \simeq t(0) \sqrt{\frac{h}{v_N t(0)}^2}. \tag{4.28}$$

This purely geometric approach to offset correction inherently assumes a homogeneous velocity structure, and flat reflectors. Vertical velocity gradients can be accommodated by specifying a more complex velocity model, which defines the Earth as a series of horizontal isovelocity layers (Taner and Koeler, 1969), while a series of layers uniformly dipping at angle θ can be corrected for by introducing a $cos^2\theta$ factor into the effective velocity (Levin, 1971). More complex Earth structure with impedance boundaries dipping at multiple, arbitrary dips can also be accommodated (Yilmaz, 1987), but at dramatically increased complexity and reduced computational efficiency. Regardless of the added complexity, NMO is still only an approximation of the wave equation, including no correction for dispersion, which leads to poor resolution of higher frequencies.

In addition, the application of NMO induces a frequency distortion, particularly on shallow reflections. Wavefronts calculated using Equation 4.27 are modelled as hyperboles. At very shallow depths the distance between hyperboles calculated for time t and time $t + \Delta t$ increases over short offset ranges. This causes the time samples constituting a seismic wavelet to become stretched as you move to larger

offsets. At greater depths the wavefronts become approximately parallel to large offsets, therefore the stretching is lower. This effect is an artefact of the imaging condition, and is also present in pre–stack depth migrated volumes (Biondi, 2006).

Several other methods have been developed to more accurately approximate the shift to zero–offset. Sherwood (e.g., Judson et al., 1978), for example, implemented a dip correction he called his 'Devilish' for Dipping–Event-Velocity-Inequalities–Licked. Subsequently, this technique has been renamed pre–stack partial migration (Yilmaz, 1987), and is now commonly referred to as Dip Move–Out (DMO). DMO can be applied before (Forel and Gardner, 1988) or after (Deregowski and Rocca, 1981) NMO, to sum traces across mid–points in manner described geometrically by Biondi (2006):

$$\frac{t_{zo}^2}{t_N^2} + \frac{x_{zo}^2}{h^2} = 1; \tag{4.29}$$

where t_{zo} is the zero offset time, t_N is the NMO time, x_{zo} the zero offset inline midpoint, and h the absolute offset.

An alternative is Azimuthal Move–Out (AMO), which produces a series of partial stacks that can then be pre–stack migrated (e.g., Ronen, 1987). Each common–shot gather is binned into a number of offset bands, AMO then transforms each of these into a common–offset–common–azimuth stack. In principle, any pre–stack imaging operator can be used for AMO, which performs the geometric transform of moving a trace from time t_1 to t_2 (Biondi, 2006):

$$t_2 = t_1 \frac{h_1}{h_2} \sqrt{\frac{h_1^2 sin^2(\beta_1 - \beta_2) - \Delta m^2 sin^2(\beta_2 - \Delta\phi)}{h_2^2 sin^2(\beta_1 - \beta_2) - \Delta m^2 sin^2(\beta_1 - \Delta\phi)}}; \tag{4.30}$$

where m is the mid–point location, β the azimuth, and ϕ the angle between input and output offset vectors.

While these methods, particularly AMO which uses an imaging operator, result in impressive improvements in the quality of post–stack migrated images, the exponential growth of computing power in recent

years has meant that pre–stack migration is now the norm. Stacked sections are often still used for quality control, but post–stack migration is generally reserved for extremely noisy environments (Biondi, 2007).

4.1.2.1 Integral Solution to the Wave Equation

The geometrical approach to migration described by Hagedoorn (1954), and subsequently expanded into a mathematical treatment of diffraction response using Kirchhoff's retardation potential solution to the wave equation (Trorey, 1970; Hilterman, 1970, 1975; Berryhill, 1977), lends itself readily to pre–stack imaging by considering the data on a trace–by–trace basis. It does not require regular spatial sampling, as is the case for the Fourier or downward continuation approaches discussed previously.

Conceptually, it involves the summation of energy from equal travel time curves, which the early computer migration algorithms, known as diffraction–stack migration (e.g., Sheriff, 1978), calculated using simple offset geometry, similar to the wavefront charts used by hand (see, Hagedoorn, 1954). However, as shown by Berryhill (1977), the phase and frequency content of the wavelet depend on distance from the apex of the diffraction hyperboloid, meaning that a complete solution to the wave equation is required to produce accurate images. The full mathematical approach takes the form of a surface integral over the wave front in the half–space of $z > 0$ using Green's Theorem (Schneider, 1978).

The application of Green's Theorem to obtain the complete integral solution of the inhomogeneous wave equation is well known, but extremely involved (e.g., Morse and Feshback, 1953). The usual solution involves integrating over the wavefront surface, S, and enclosed volume, V, with a given set of boundary conditions. For application to seismic data, Schneider (1978) assumed a point source, thereby introducing a spherical spreading parameter into the initial differential

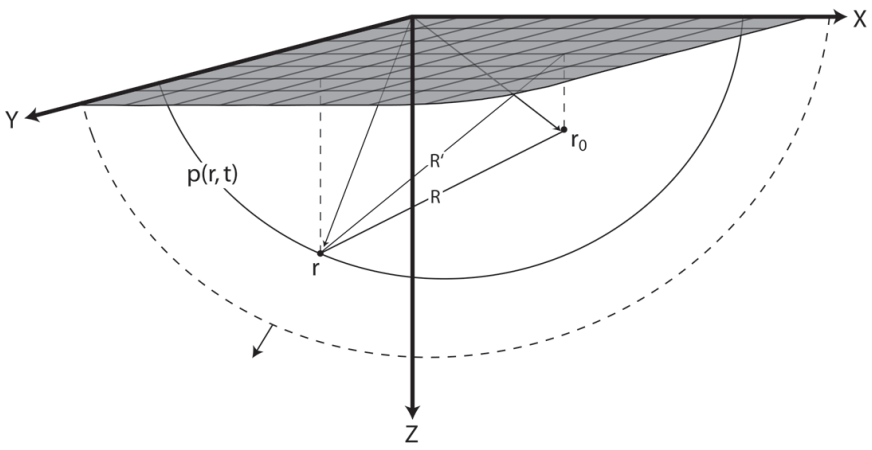

Figure 4.4: Illustration of boundary conditions for integral solution of the inhomogeneous wave equation, adjusted from Schneider (1978). Location r_0 is the source point for wavefront $p(r,t)$ observed at location r.

wave equation (see, Equation 4.31), but allowing the volume integral to be ignored as the initial volume, V_0, is equal to zero.

$$-4\pi.s(x,y,z,t) = \nabla^2 p - \frac{1}{v^2}\frac{\partial^2 p}{\partial t^2}. \tag{4.31}$$

Expressing this as an integral over surface, S, at time, t, distance, r, from the source location r_0, t_0, takes the form:

$$p = \frac{1}{4\pi}\int dt \int dS \left[G\frac{\partial}{\partial n}p(r_0,t_0) - p(r_0,t_0)\frac{\partial}{\partial n}G\right]; \tag{4.32}$$

where $\mathbf{n}$ is the outward normal vector to surface, S (Schneider, 1978).

This is the spatially independent homogeneous wave equation, with inhomogeneous boundary conditions of the Dirichlet type, such that the gradient of $p \to 0$ at S (Schneider, 1978). As a result, the second term in square brackets also tends to zero, reducing the boundary value to an integral over the wavefront surface, S, and a suitable Green's function. Schneider (1978) found a suitable Green's function

to be:

$$G(r,t \mid r_0,t_0) = \frac{\delta\left(t - t_0 - \frac{R}{v}\right)}{R} - \frac{\delta\left(t - t_0 - \frac{R'}{v}\right)}{R'}; \tag{4.33}$$

where R and R' are vectors defined in Figure 4.4.

Substitution leads to a rigourous statements of the Huygen's principle, commonly referred to as the Kirchhoff Integral:

$$\boxed{p(r,t) = \frac{1}{2\pi}\int_{t_0}\int_A p(r_0,t_0)\frac{\partial}{\partial z_0}\left[\frac{\delta\left(t - t_0 - \frac{R}{v}\right)}{R}\right] dA dt_0.} \tag{4.34}$$

This expresses the migration process performed over aperture, A, as a 3D, frequency–domain convolution between the recorded wavefield and a space–time operator (Schneider, 1978), in the same manner as that derived by Claerbout and Doherty (1972). Equation 4.34 can, therefore, be recast in terms of a downward continued wavefield:

$$p(x,y,z,t=0) = \int_A -\frac{1}{2\pi R}\frac{\partial}{\partial z}p\left(x,y,z=0,t=R/c\right) dA. \tag{4.35}$$

Basic Fourier theory tells us that $\frac{\partial}{\partial t}f(t) \leftrightarrow i\omega F(\omega)$. Hence, by considering the observed wavefield as the superposition of infinite monochromatic wavefields, the kernel of Equation 4.35 becomes:

$$\frac{\partial}{\partial z}p\left(x,y,z=0,t=R/c\right) = \int_\omega i\omega p(x,y,z=0,\omega)e^{-i\omega t}d\omega; \tag{4.36}$$

Leading to a full expression of 3D Kirchhoff imaging (Bleistein and Gray, 2001).

$$\boxed{I(\xi) = \int_A W(x,y,z,t)\int_\omega i\omega p(x,y,z,\omega)e^{-i\omega t}d\omega dA;} \tag{4.37}$$

where $W(x, y, z, t)$ is a weighting function that combines terms to account for the obliquity, the angular dependance of amplitudes generated by a Huygen's secondary source, and spherical spreading. In practice, because the recorded wave field is quantised, we use multi–dimensional summation rather than a pure integration.

Being a simple summation over the wavefront, there is no theoretical limit on the maximum dip angle that can be imaged. However, the computational cost of imaging grows with the cube of the depth, and the non–continuous sampling of the reflected waveform will introduce aliasing artefacts above certain dip angles (see, **Chapter 2**). Therefore, it is practically necessary to introduce a maximum imaging aperture over which data is summed, thereby imposing limits on the maximum dip angle of the wavefront and the computational cost. For most applications this has little degrading effect on the final image, while the four Chirp transducers on the 3D Chirp mat act to beam form the seismic source (e.g., Gutowski et al., 2002; Gutowski, 2004), therefore limiting the amplitudes of reflections from steeply dipping events. Also, Kirchhoff summation mixes amplitudes from different times and makes Kirchhoff migration robust in low S/N environments since the 'randomness' of the noise will lead to cancellation (Yilmaz, 1987).

Although vertical velocity gradients can be readily accommodated, a major limitation of the integral solution to the wave equation is its ability to cope with lateral velocity variations (Hubral, 1977). There are a number of approaches using ray tracing (e.g., Červeny and Pšenčík, 1983) or finite–difference (e.g., van Trier and Symes, 1991) methods, all of which involve solving a high frequency approximation of the wave equation (the Eikonal equation of Bleistein (1984)) using the asymptotic Green's function. As the velocity model becomes more complex and multiple ray paths are generated, the Green's function becomes multi–valued and the summation surface multi–branched, making the solution extremely computationally expensive and inaccurate (Biondi, 2007).

4.1.2.2 Wavefield Continuation Methods

Given the present models for oil/gas reservoir formation and migration, the exploration industry is especially keen on obtaining high–resolution images of geologically complex structures such as salt domes or steeply dipping fault planes, locations where the traditional integral solution to the wave equation becomes least accurate. In response, there has been a significant effort dedicated toward the development of a non–asymptotic approach to solving the scalar wave equation. Although commonly referred to as Wave Equation Migration, since all computer migrations involve solving the wave equation, they would be better described as a Wavefield Continuation approach to migration.

The basic premise can be described by the following 2–step process:

1. Numerical propagation of the recorded wavefield, and possibly the source function (depending on the wavefield continuation approach), through a velocity model.
2. The formation of an image by the application of an imaging condition to the propagated wavefield(s).

There are a number of ways to accomplish these imaging steps, which can be grouped under the general headings of Reverse–Time Migration (Baysal et al., 1983; Whitmore, 1983) or Downward Continuation Migration. The principles of these two approaches are the same, with the exception that reverse–time migration works in the time domain, and downward continuation in the depth domain. Using a velocity model, the receiver wavefield is propagated backwards in time/depth from the recorded data, while the source wavefield is propagated forwards in time/depth using an assumed source wavelet. An image, in image space (x_ξ, y_ξ, z_ξ), is then formed where the 2 wavefields coincide. Mathematically, this is described by the condition:

$$I(x_\xi, y_\xi, z_\xi) = \sum_i \sum_t \begin{array}{l} p_g(x = x_\xi, y = y_\xi, t, z = z_\xi; \mathbf{s}_i) \\ p_s(x = x_\xi, y = y_\xi, t, z = z_\xi; \mathbf{s}_i) \end{array} \tag{4.38}$$

where p_s and p_g are the source and recorded wavefields, respectively.

Migration Type	Limiting Dip Angle (°)	Velocity Model Complexity	Irregular Sampling	Computational Cost
Finite–Difference	15/45	Vertical & Horizontal	No	Medium
Phase–Shift	90	Vertical	No	Low
f–k Stolt	90	None	No	Very Low
Kirchhoff	None	Vertical & Horizontal	Yes	High
Wavefield Continuation	None	Vertical & Horizontal	Yes	Very High

Table 4.1: Summary table comparing the limitations of different migration techniques.

However, this condition generates internal reflections that cause high amplitude, low frequency artefacts to be introduced into the final volume when the velocity model contains sharp interfaces (particularly at shallow depths/times) (e.g., see Zhang and Sun, 2009). Several methods have been proposed to eliminate this problem, such as: reducing acoustic impedance differences to zero at the interfaces (Baysal et al., 1983); using a non–reflective wave equation (Baysal et al., 1984); smoothing the velocity model (Mulder and Plessix, 2003; Biondi, 2006); or angle–domain muting of reflection angles $> 60°$ (Zhang and Sun, 2009). However, none have satisfactorily demonstrated a practical solution without degrading the imaged volume or adding to the already expensive computational cost. It is this computational expense that is the downfall of most wavefield continuation methods. Although the linearity of Equation 4.5 allows several shot gathers to be imaged at once using either the delayed shot migration (Zhang et al., 2005) or plane wave (Duquet et al., 2001) approaches, thereby reducing the computing time by a factor of the migration aperture shot fold, the computational cost is still prohibitive. As a result, it is almost never used (Biondi, 2007).

4.1.3 Migration of 3D Chirp Data

The application will often constrain the most suitable imaging technique. When considering 3D Chirp data, the following characteristics

need to be considered when migrating a volume:

i) **Time vs. Depth Migration**: The maximum source–receiver offset in 3D Chirp data is 1.5 m. Even with a source frequency content of 1.5 kHz to 13.0 kHz and a sample rate of 20 μs, there is not enough of a diffraction curve within common–shot or common–reflection point gathers to enable velocity picking (Yilmaz, 1987). Diffraction curves are observed in the common–offset sections, but accurate interval velocity picking in this domain is complicated. Also, given the complexity and expense of acquiring 10 m to 30 m cores in shallow water, there is little opportunity for using core logged p–wave velocity data to constrain an interval velocity model for the migration of a 3D Chirp volume. This removes the possibility of performing a depth migration, which uses the interval velocity model to apply a traveltime correction and depth conversion simultaneously. Effectively, the imaging of 3D Chirp volumes is restricted to time migration, where an RMS velocity (v_{rms}) model is used for traveltime correction only. However, time migrations are less computationally expensive and more robust to velocity model errors.

ii) **Velocity Sensitivity**: The small migration apertures resulting from source array beam forming (**Chapter 2**) and shallow depths lead to a low velocity sensitivity. Figure 4.5 shows the change in traveltime correction with velocity for a variety of depths, together with the gradient of those relationships. The theoretical resolution of the broadband Chirp sweeps (w13 and w32; **Chapter 2**) can be described by the relationship (Quinn, 1997):

$$\frac{1}{(-3\ dB)\Delta f} \leq t_{res} \leq \frac{1.5}{(-3\ dB)\Delta f}. \tag{4.39}$$

The -3 dB effective bandwidth for these sweeps is 10.0 kHz (2.0 – 12.0 kHz), which equates to a theoretical resolution of 0.10 ms $\leq t_{res} \leq$ 0.15 ms. Taking 0.15 ms as being the maximum resolution attainable in real data (Plets, 2007), Figure 4.5b indicates that, even for a reflector at 50 m depth, the v_{rms} would have to change by 100 ms^{-1} to have a resolvable difference in traveltime

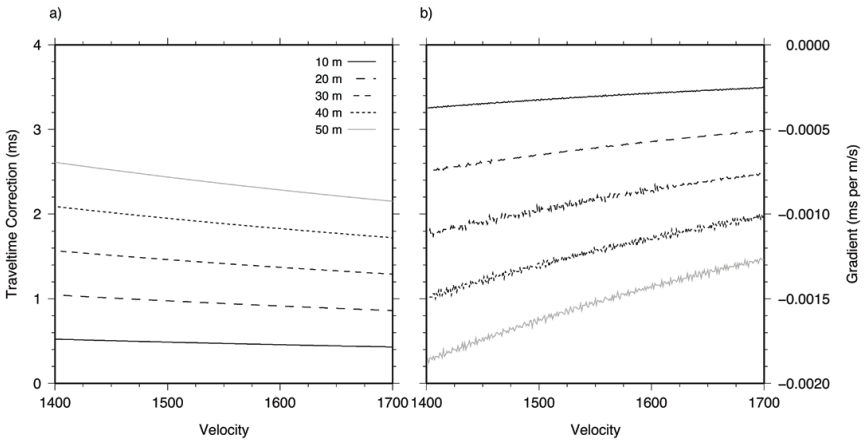

Figure 4.5: Illustration of limited sensitivity to changes in v_{rms}. Panel a) shows variation with velocity of traveltime correction calculated at maximum aperture and maximum offset for a series of different depths. Panel b) shows the changing gradient of the lines on a). For comparison, the theoretical temporal resolution limit of the broadband Chirp sweeps (w13 and w32; **Chapter 2**) is between 0.10 ms and 0.15 ms (Plets, 2007).

corrections. Interval velocity changes of ~ 100 ms^{-1} are possible in volumes with several distinct stratigraphic facies, but highly unlikely with v_{rms} values for 3D Chirp applications to image features in sedimentary units. Hence, it is reasonable to assume a constant velocity field for 3D Chirp imaging.

iii) Dip Angle: The 3D Chirp source array beam forms the outgoing Chirp sweep to a narrow (15° cross–track and 30° along–track) downgoing cone (**Chapter 2**). This limits the maximum observable dip angle of reflectors to 15° in the cross–track direction and 30° in the along–track direction. In addition, with a horizontal sampling interval of 0.125 m the highest frequencies become aliased at dip angles $\geq 13°$ (**Chapter 2**). To avoid introducing aliasing artefacts into the migrated volume a generic maximum dip angle of 13° is assumed.

iv) Non–Regular Grid: The acquisition of regularly spaced 1.0 m lines (as required for complete coverage using 3D Chirp profiler; **Chapter 1**) is not feasible when surface towing equipment be-

hind a small boat. A survey area is normally covered by repeated strafing at a number of different orientations (**Chapter 3**). This results in highly variable trace spacing, CMP fold, and the offset sampling within each CMP bin. Any suitable migration method needs to be robust to these irregularities, in particular discontinuities in the spatial coverage.

Therefore, when migrating a 3D Chirp volume, we choose to perform a constant velocity time migration to a maximum dip angle of 13°.

Ideally, such imaging would be performed pre–stack where the true source–receiver locations are used to solve the wavefield. Of the pre–stack migration algorithms discussed in Subsection 4.1.2, Kirchhoff migration is the most appropriate since it treats each trace independently and is therefore insensitive to irregularities in acquisition geometry. In comparison to other pre–stack approaches, it is also computationally inexpensive (especially for constant velocity time migration), although, as was discussed in **Chapter 3**, it is still computationally too expensive to use on a full 3D Chirp volume (when applied using the ProMAX algorithm). This expense arises because Equation 4.37 accommodates dispersion by frequency decomposing the recorded wavefield into a set of monochromatic wavefields that are then migrated and summed independently, not the number of traces or samples to be migrated. For the shelf application thought experiment introduced in **Chapter 2**, the trace length of 100 ms and sampling interval of 20 μs results in $\geq$ 2000 frequency samples ($\geq$ 4000 including negative frequencies). Migrating each of these monochromatic traces independently increases the number of traces processed by the migration kernel from c. 15 million to $\geq$ 30 billion. As a result, imaging is generally limited to subsets rather than the whole volume (e.g., see **Chapter 3**).

The obvious way of reducing computation time is to image post–stack, which increases efficiency by a factor of the average fold (c. 20 for a typical 3D Chirp volume), at the expense of a lower resolution image due to a combination of: the NMO effects discussed previously; and

the assumption that each CMP stacked trace originates at the bin centre rather than the true source/receiver mid–point. Since 3D Chirp data lends itself to performing a constant velocity time migration, the most efficient post–stack imaging algorithm is the Frequency–Wavenumber approach (from now on referred to as fk–Stolt migration), which is faster than the Finite Difference or Phase–Shift approaches (particularly Finite Difference), whilst also being more accurate by solving the full scalar wave equation. However, performing the post–stack imaging in the fk–domain is less robust in the presence of gaps in spatial coverage since the Fourier transform assumes regularly spaced sampling for efficiency. This is a significant issue, since the 1.0 m line spacing required for complete coverage using the 3D Chirp sub–bottom profiler is not practical (**Chapter 1**).

There are a number of methods that can be used to reduce artefacts through interpolation of the irregular pre–stack data onto a regular post–stack grid. The most reliable is partial pre–stack migration using an imaging operator (normally the Kirchhoff operator). There are two basic approaches: operator continuation in either the common–offset (e.g., Bagaini and Spagnolini, 1996), common–shot (Spagnolini and Opreni, 1996), or azimuthal domains (Fomel and Biondi, 1996; Biondi et al., 1998; Chemingui, 2001); or operator inversion (e.g., Nemeth et al., 1999). Both these methods are computationally very expensive (particularly operator inversion), and provide little efficiency improvement over a full pre–stack Kirchhoff migration since the imaging operator would still require frequency decomposed traces. Also, continuation of 3D Chirp in common–shot or azimuthal domains is not possible given the offset limitations.

Alternatively, a purely statistical approach can be taken using: Fourier operators with the non–uniform Fourier transform (e.g., Duijndam and Schonewille, 1998; Duijndam et al., 1999; Hindriks and Duijndam, 2000); iterative optimisation of the downward continuation convolution operator using prediction–error filters (e.g., Spitz, 1991; Crawley, 2001); or stochastic inversion of the Radon transform operator (e.g., Thorson and Claerbout, 1985). The limited offsets make inversion of

the Radon transform operator unfeasible, while iterative optimisation of the convolution operator is computationally expensive since it also assumes a monochromatic wavefield and, therefore, requires frequency decomposition. Fourier interpolation using the non–uniform Fourier transform could be applied to regularise 3D Chirp pre–stack volumes, but the limiting gap size that can be reliably reconstructed is three times the Nyquist interval, beyond which a weighting function tends the amplitudes toward zero (Duijndam et al., 1999). With a spatial sampling of 0.125 m, three times the Nyquist interval ($1/2B$; B = bandwidth) equates to 0.75 m. Given the primary concern for imaging 3D Chirp volumes is filling the larger spatial discontinuities (≥ 1 Fresnel Zone radius), a limiting reconstruction distance of < 1.0 m is not a sufficient return for the computational cost of performing the 2D non–uniform Fourier transform.

As a result, the only suitable method for providing a post–stack migration with a fully regularly sampled volume is the simple padding of empty CMP's with blank traces after NMO and stacking.

4.2 Testing

In the following subsections the imaged results from pre– and post–stack migration for a number of different conditions using real and synthetic volumes are compared. Pre–stack, the imaging is performed using a full 3D Kirchhoff time migration, while post–stack empty CMP bins are padded with zero traces prior to imaging using a fk–Stolt migration. The constant velocity assumption allows the fk–Stolt migration to be performed using two–passes of a 2D migration with orthogonal sorting directions (Dickinson, 1988).

4.2.1 Synthetic Modelling

Several synthetic models were generated using the Phase Screen 3D forward modelling code of Wild and Hudson (1998) to test reflector reconstruction across gaps (Figure 4.6). The models contained two

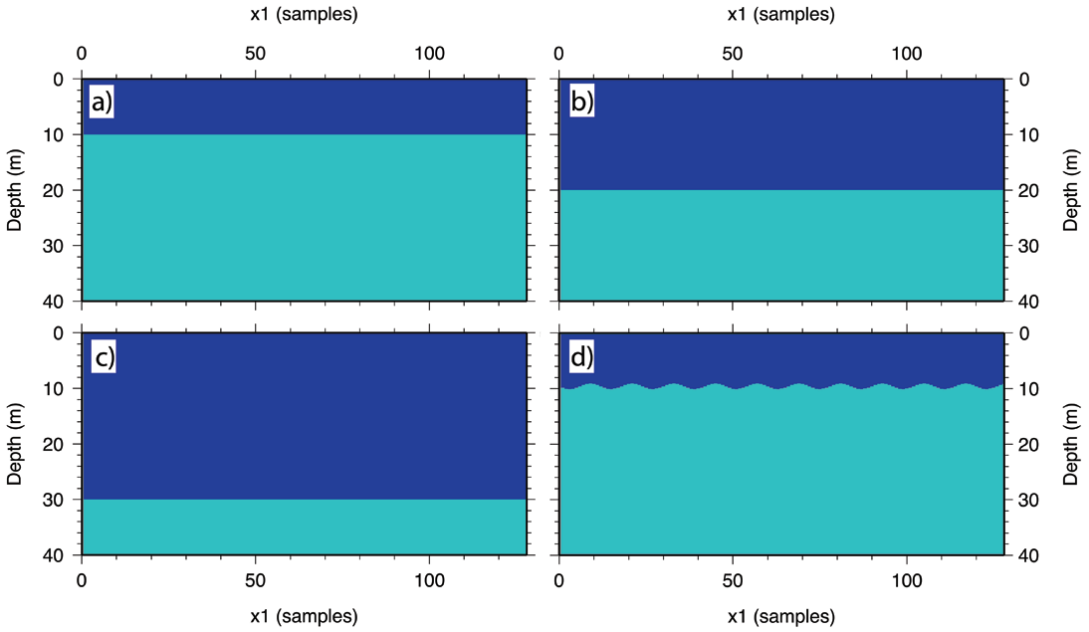

Figure 4.6: Figure illustrating the four synthetic models. Panels a through c show a flat interface between two media (velocities 1480 ms^{-1} and 1550 ms^{-1} and densities 1020 gm^{-3} and 1680 gm^{-3}, respectively), while panel d contains a sinusoidal boundary with 1.0 m peak–to–peak amplitude and 6.0 m wavelength.

media with velocities of 1480 ms^{-1} and 1550 ms^{-1}, and densities of 1020 gm^{-3} and 1680 gm^{-3}, respectively. Synthetic volumes were created using a flat interface between these two media at three depths (10.0 m, 20.0 m, and 30.0 m), and a complex sinusoidal interface centred about 10.0 m depth. Source and receiver geometry mimicked as closely as possible the 3D Chirp array, with a central source (beam formed using limited take–off angles) surrounded by a 2.0 m by 2.5 m array of receivers at 0.25 m intervals in both X and Y.

By varying reflector depth and complexity, along with gap size and asymmetry, the ability of pre– and post–stack migration algorithms to reconstruct reflectors in areas with missing spatial coverage can be compared.

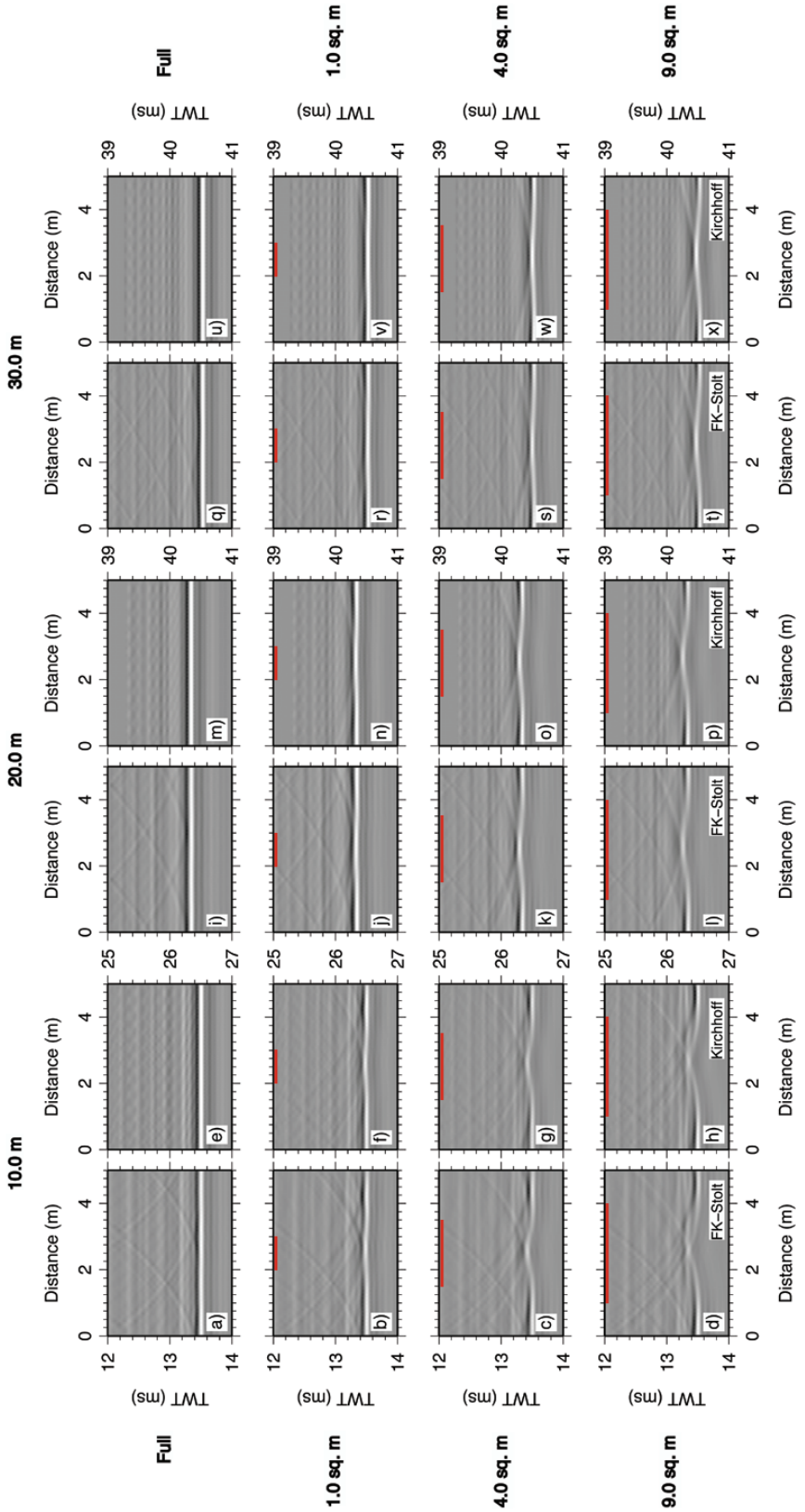

Figure 4.7: Illustration of reflector reconstruction by fk–Stolt and Kirchhoff migration for gaps of increasing size and reflectors at increasing depth. Top row of panels show imaged sections for fully sampled volume, second row contains a 1.0 m^2 gap in the centre of the section, while the third and fourth rows 4.0 m^2 and 9.0 m^2 gaps, respectively. Red lines indicate regions of missing data prior to migration. The first pair of columns show results for reflector at 10.0 m depths, second and third pairs for 20.0 m and 30.0 m, respectively.

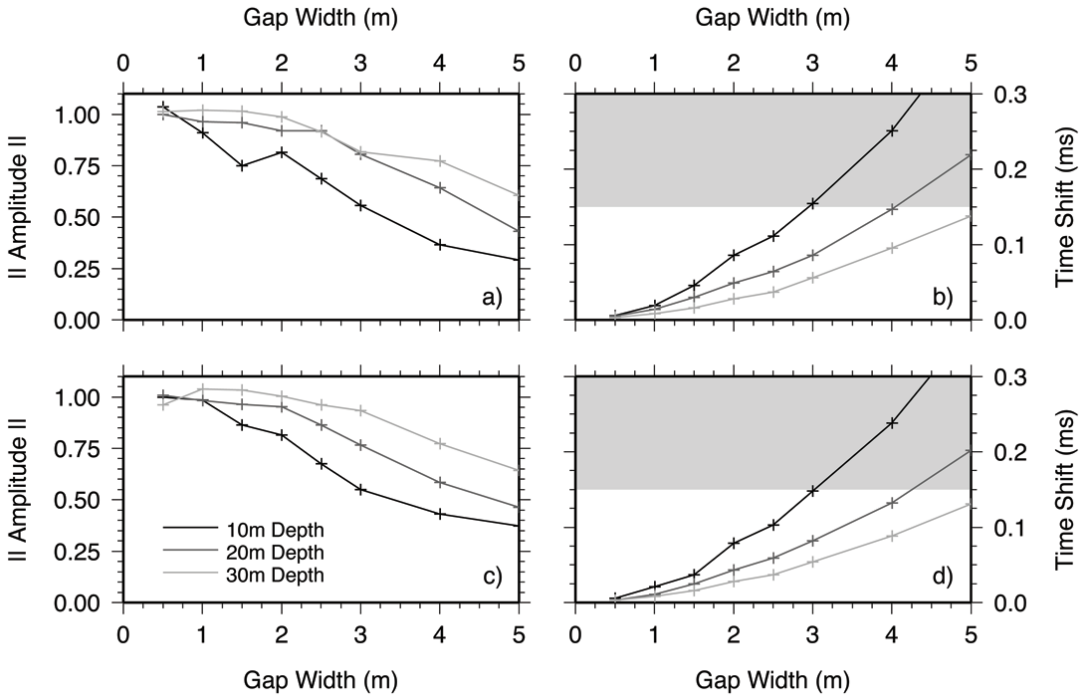

Figure 4.8: Extracted reflector amplitudes and time shifts for central trace from volumes with varying gap sizes and reflector depths, normalised against fully sampled volume. Panels a) and b) show results migrated using two–pass, padded fk–Stolt migration, while c) and d) results from 3D pre–stack Kirchhoff.

4.2.1.1 Reflector Reconstruction with Depth

Traces within symmetric areas of 0.5×0.5 m, 1.0×1.0 m, 1.5×1.5 m, 2.0×2.0 m, 2.5×2.5 m, 3.0×3.0 m, 4.0×4.0 m, and 5.0×5.0 m were removed from the centre of the synthetic volume to artificially introduce gaps in the spatial coverage of sizes 0.25 m^2 through 25.0 m^2. Each volume was imaged using pre–stack 3D Kirchhoff time migration, and using two–pass post–stack fk–Stolt migration, both assuming a constant v_{rms} of 1500 ms^{-1}.

Figure 4.7 shows cross–line sections through imaged volumes. The first pair of columns (panels a through h) show results for fully sampled volume, together with 1.0 m^2, 4.0 m^2, and 9.0 m^2 gaps centred within the section for reflector at 10.0 m depth, migrated using post–

stack fk–Stolt (a to d) and pre–stack Kirchhoff (e to h). Subsequent column pairs show same results for reflectors at 20.0 m and 30.0 m depth. Increasing depth allows larger gaps to be reliably reconstructed (lower row of panels) as the Fresnel zone radius grows from 1.23 m at 10.0 m depth to 2.12 m at 30.0 m depth. This is supported by reflector amplitudes extracted from the central trace (Figure 4.8a and c), which show an increase by c. 15 % of the peak amplitude with each 10.0 m increase is depth.

Panels c, d, g, and h on Figure 4.7 suggest that the interpretable reconstruction limit for a reflector depth of 10.0 m is $\leq$ 2.0 m width ($\leq$ 4.0 m^2 area). Panels c and g show imperfect, but interpretable, reflector reconstruction across a 2.0 m wide gap, whereas panels d and h show a distinct gap in the reconstruction, increased steeply dipping, uncancelled energy propagating to shallower times, and the suggestion of a false reflector being reconstructed at a shallower depth (c. 15.9 ms). This change in the reconstructed reflector time is particularly useful. Figure 4.8b and c show when this change in traveltime becomes theoretically resolvable (indicated by the shaded grey region) using the broadband Chirp sweep resolution limit of 0.15 ms (Plets, 2007). For a reflector at 10.0 m depth the shift in reconstructed reflection peak becomes resolvable at a gap size of 3.0 m (9.0 m^2); supporting the interpretation of the reconstruction limit as $\leq$ 2.0 m from cross–line sections in Figure 4.7. Breakdown in reflector reconstruction for reflectors at 20.0 m depth therefore occurs at $<$ 4.0 m (16.0 m^2) and $<$ 6.0 m (36.0 m^2) at 30.0 m depth, which is in agreement with a limit being approximately equal to twice the Fresnel Zone radius (approximately 1.23 m, 1.73 m, and 2.12 m for 10.0 m, 20.0 m, and 30.0 m depth, respectively).

Results for pre–stack 3D Kirchhoff migration and two–pass padded fk–Stolt are consistent. Both demonstrate a loss of reflector reconstruction at the same gap sizes, and remarkably similar reconstruction prior to this limit. Although, the post–stack fk–Stolt imaged volumes have larger amounts of steeply dipping, uncancelled energy migrated

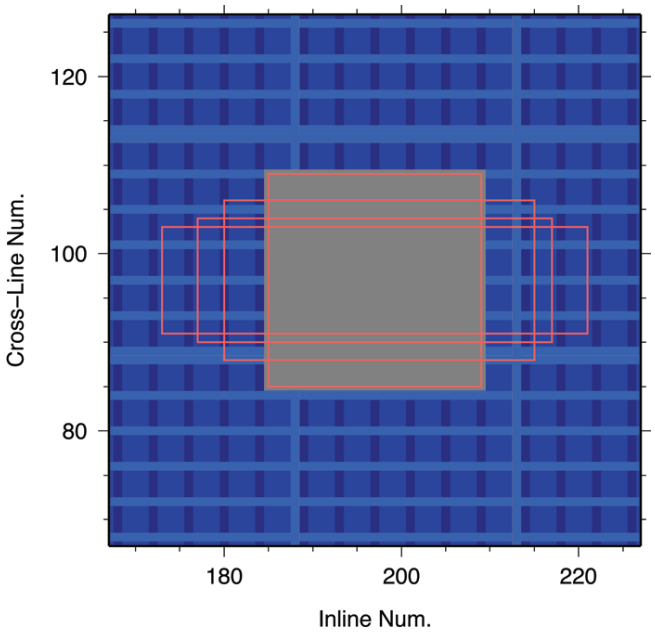

Figure 4.9: Illustration of the artificial gaps introduced into the CDP coverage of the synthetic volumes to mimic discontinuities in the spatial sampling. Grey square outlined in red shows a 3.0 × 3.0 m block of missing data. Superimposed red rectangles show gaps of the same spatial area, but increasing asymmetry from 2:1 through 4:1.

to shallower times, and slightly lower reconstructed amplitudes, the difference is negligible.

4.2.1.2 Reflector Reconstruction with Gap Symmetry

Gaps with the same set surface areas (between 0.25 m^2 and 25.0 m^2) but inline to cross–line width ratios ranging between 1:1 and 4:1 (Figure 4.9) were removed from the synthetic volume of a flat reflector at 10.0 m depth. Each of these 24 volumes was imaged pre–stack using 3D Kirchhoff time migration, and post–stack using a padded two–pass fk–Stolt migration. In the post–stack case, the first sorting direction was such that imaging was carried out along the shorter gap width axis, which optimised reflector reconstruction for the asymmetric gaps.

Figure 4.10 shows cross–line sections through the centre of the imaged volumes for the fully sampled volume, together with missing areas of 1.0 m^2, 4.0 m^2, and 9.0 m^2 for symmetric gaps, and inline to cross–line ratios of 2:1 and 3:1. As gap asymmetry increases so does continuity of the reconstructed reflector for gaps of constant surface area, although this reconstruction appears to take place at shallower times

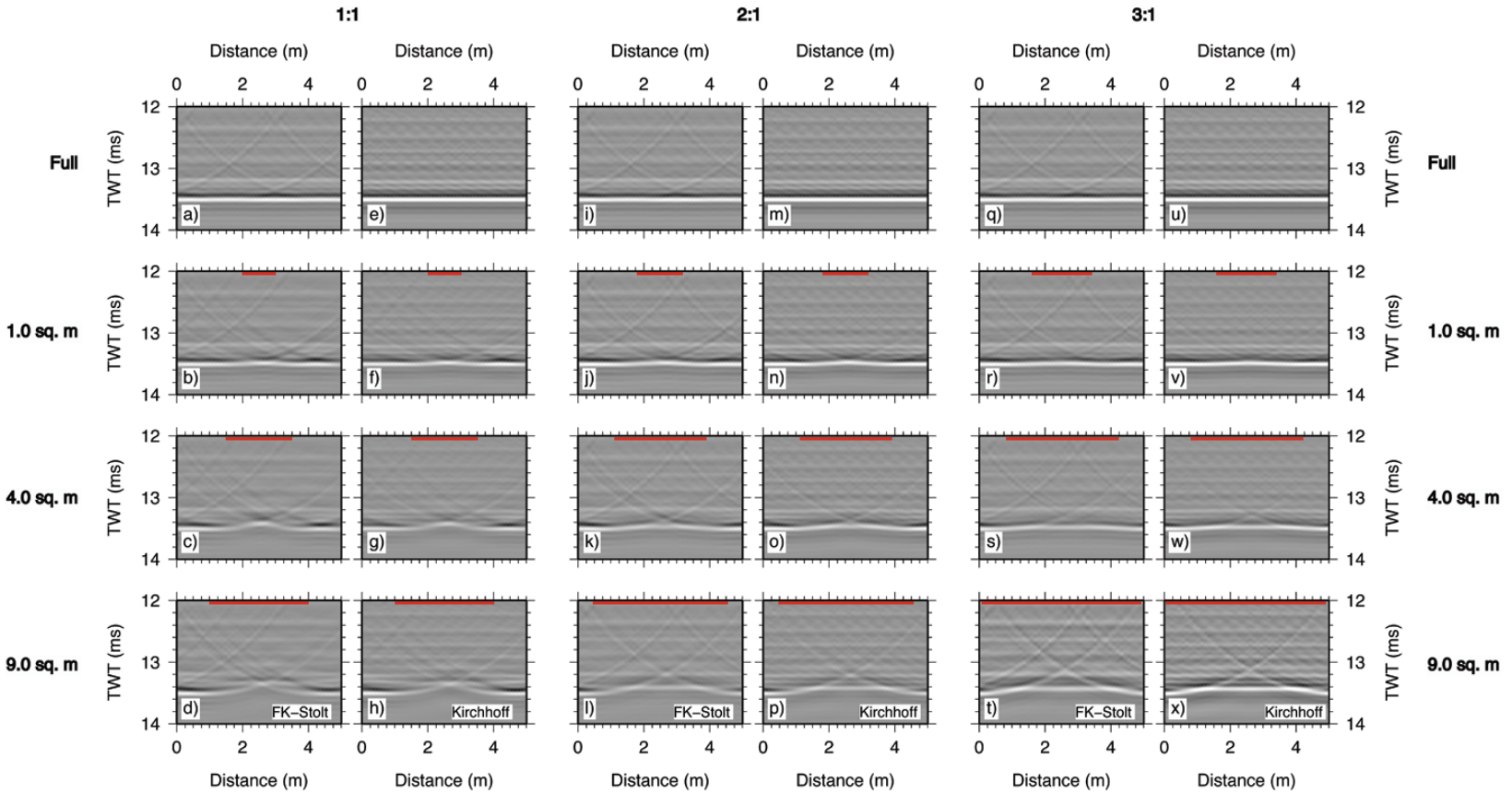

Figure 4.10: Illustration of reflector reconstruction by fk–Stolt and Kirchhoff migration for gaps of increasing size and asymmetry. Top row of panels show imaged sections for fully sampled volume, second panel contains a 1.0 m^2 gap in the centre of the section, while the third and fourth rows 4.0 m^2 and 9.0 m^2 gaps, respectively. Red lines indicate regions of missing data prior to migration. The first pair of columns show results for gaps with inline to cross–line ratio of 1:1, second and third pairs for 2:1 and 3:1, respectively. All at 10.0 m depth.

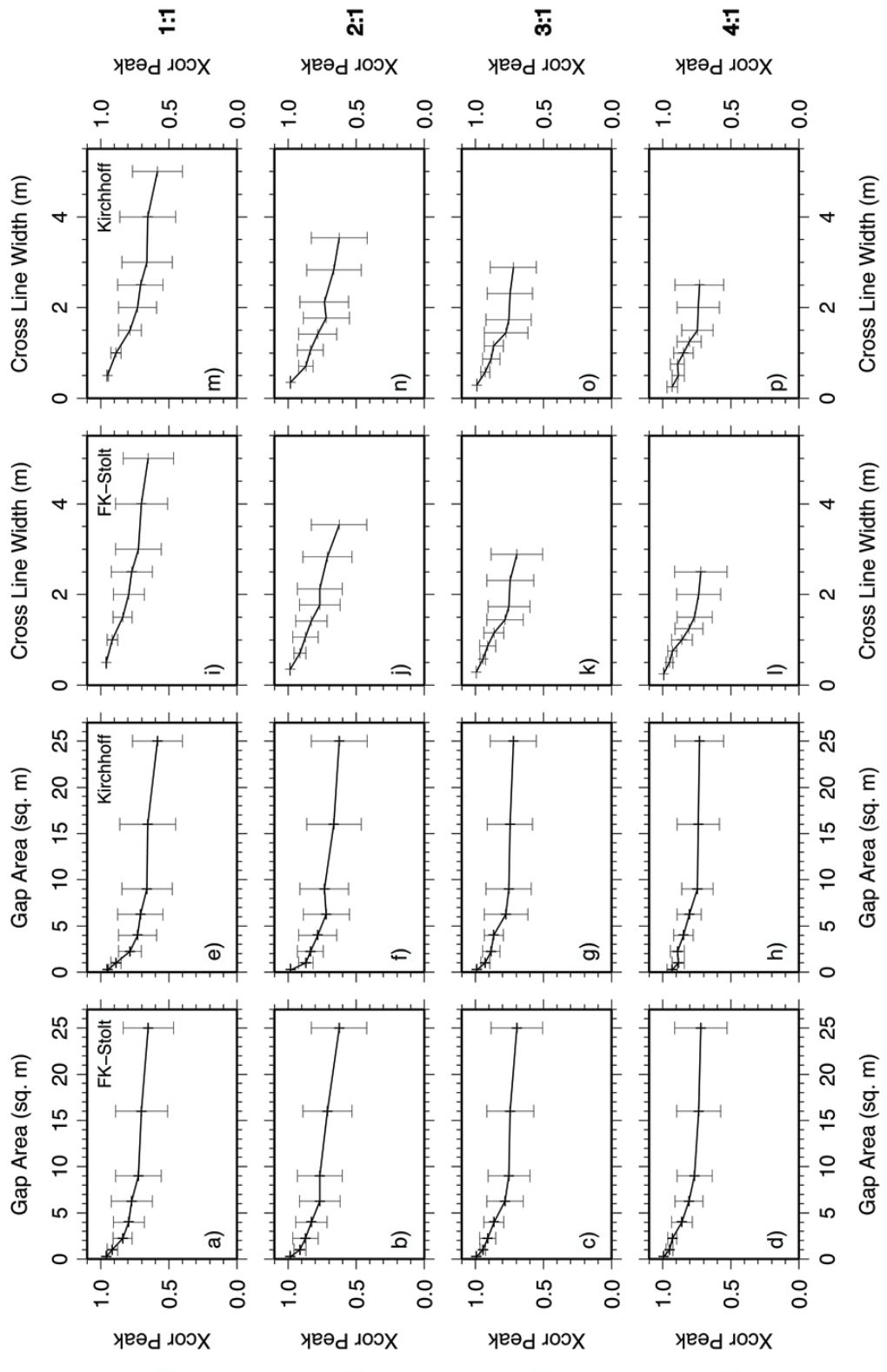

Figure 4.11: Volumetric cross–correlations calculated between fully sampled volume and gapped volumes for missing region, imaged using fk–Stolt and Kirchhoff migration. Each row shows results for gaps of a different inline to cross–line width ratio; 1:1, 2:1, 3:1, and 4:1, respectively. While first pair of columns show results normalised to gap surface area, and second pair to cross–line width.

(compare panels r and v with t and x in Figure 4.10). This is also evident in the volumetric cross–correlation results (Figure 4.11), which show no significant change in mean peak value with gap asymmetry whether normalised against gap area (panels a through h) or cross–line width panels i through p). Suggesting that, for simple reflectors, the reconstruction is dominated by the minimum image location to trace distance (i.e., the smallest gap width).

As with reflectors at different depths, the results of pre– and padded post–stack migration are very similar. Differences in the cross–correlated results are extremely subtle (Figure 4.11), as is the slight increase in uncancelled energy at shallower times in the post–stack imaged volume (Figure 4.10). The amplitudes of the reconstructed horizons are also slightly higher when imaged with pre–stack Kirchhoff migration; panels t and x, Figure 4.10.

4.2.1.3 Reflector Reconstruction for Complex Reflectors

Modelling gaps in flat reflectors at various depths and with different gap asymmetries provides limited insights into the behaviour of the migration algorithms due to the low likelihood of imaging a perfectly flat and continuous reflector in a real data volume. These results are, therefore, not necessarily representative of the reflector reconstruction attainable in real data. Figures 4.12, 4.13, and 4.14 show the imaging results for gaps of various sizes and symmetries using a synthetic volume containing a sinusoidal reflector of 1.0 m peak–to–peak amplitude and 6.0 m wavelength, centred around a depth of 10.0 m (see, Figure 4.6 and **Appendix A**).

Figure 4.12 compares the reflector amplitude of the central trace as gap sizes vary between 0.25 m^2 and 25.0 m^2, and gap symmetries between 1:1 and 4:1 (normalised against the amplitude extracted from the fully sampled volume). When plotted against gap area the results are independent of gap asymmetry, but when plotted against cross–line width, there is a clear distinction between reconstruction across symmetric and asymmetric gaps. This is supported by Figure 4.14,

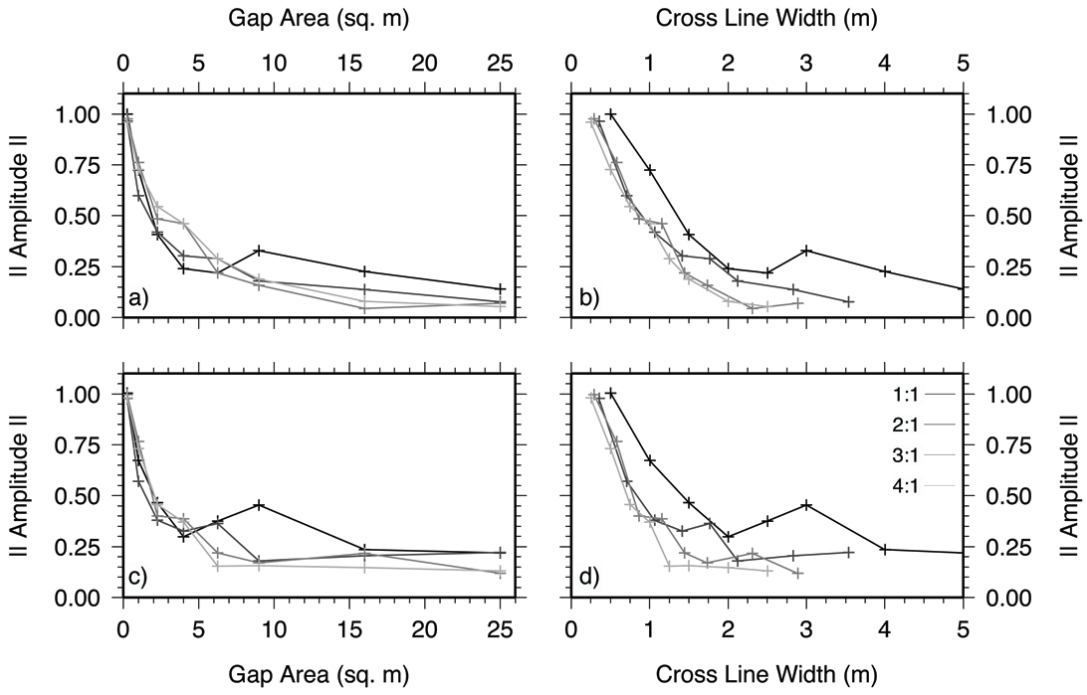

Figure 4.12: Extracted reflector amplitudes for central trace from volumes with varying gap sizes and varying gap symmetries, normalised against fully sampled volume for a sinusoidal reflector of 6.0 m wavelength. Panels a) and b) show results migrated using padded fk–Stolt algorithm, while c) and d) results from 3D pre–stack Kirchhoff .

where the mean volumetric cross–correlation for gaps of equal cross–line width decreases with increasing asymmetry.

Figure 4.13, which shows cross–line sections through volumes containing symmetric gaps imaged using Kirchhoff and fk–Stolt migration, suggests that the limiting reconstruction for a reflector of this depth is ≤ 2.0 m (4.0 m^2). In Figure 4.14 this corresponds to volumes with volumetric cross–correlation of ≥ 0.75 being successfully reconstructed. This places a limiting cross–line gap width of 1.5 m, 1.25 m, and 1.0 m for gap asymmetries of 2:1, 3:1, and 4:1, respectively. This is likely to be caused by the reconstruction of complex reflectors being more sensitive to the contribution of the whole Fresnel Zone, rather than the minimum image location to trace distance. Therefore, as gaps in

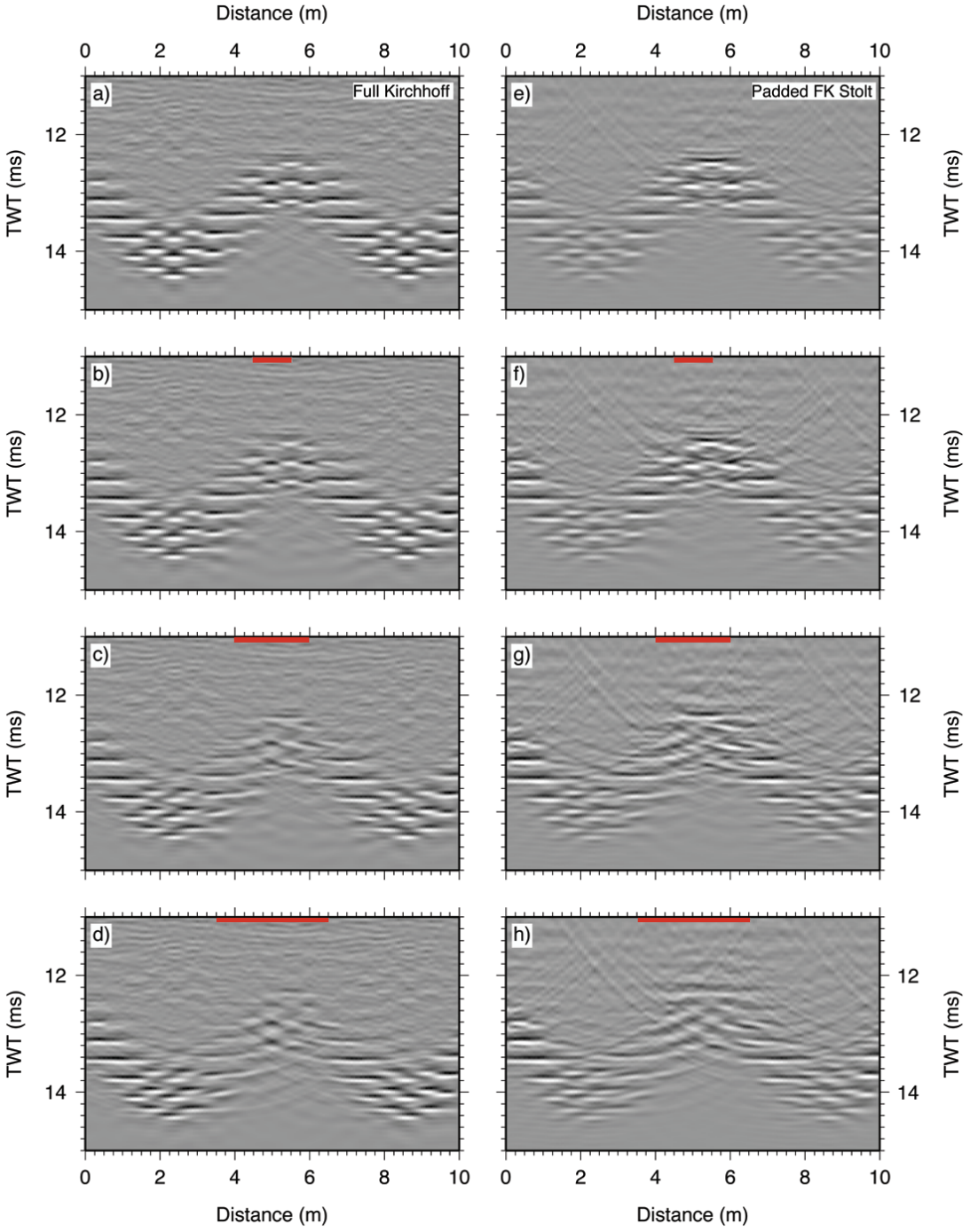

Figure 4.13: Figure showing cross–line sections imaged using pre–stack Kirchhoff through full, a) through d), and post–stack fk–Stolt , e) through h), migration algorithms. Panels a) and e) are from fully sampled volumes, while b) and f), c) and g), and d) and h), contain 1.0×1.0 m, 2.0×2.0 m, and 3.0×3.0 m gaps, respectively, centred around 5.0 m into the section.

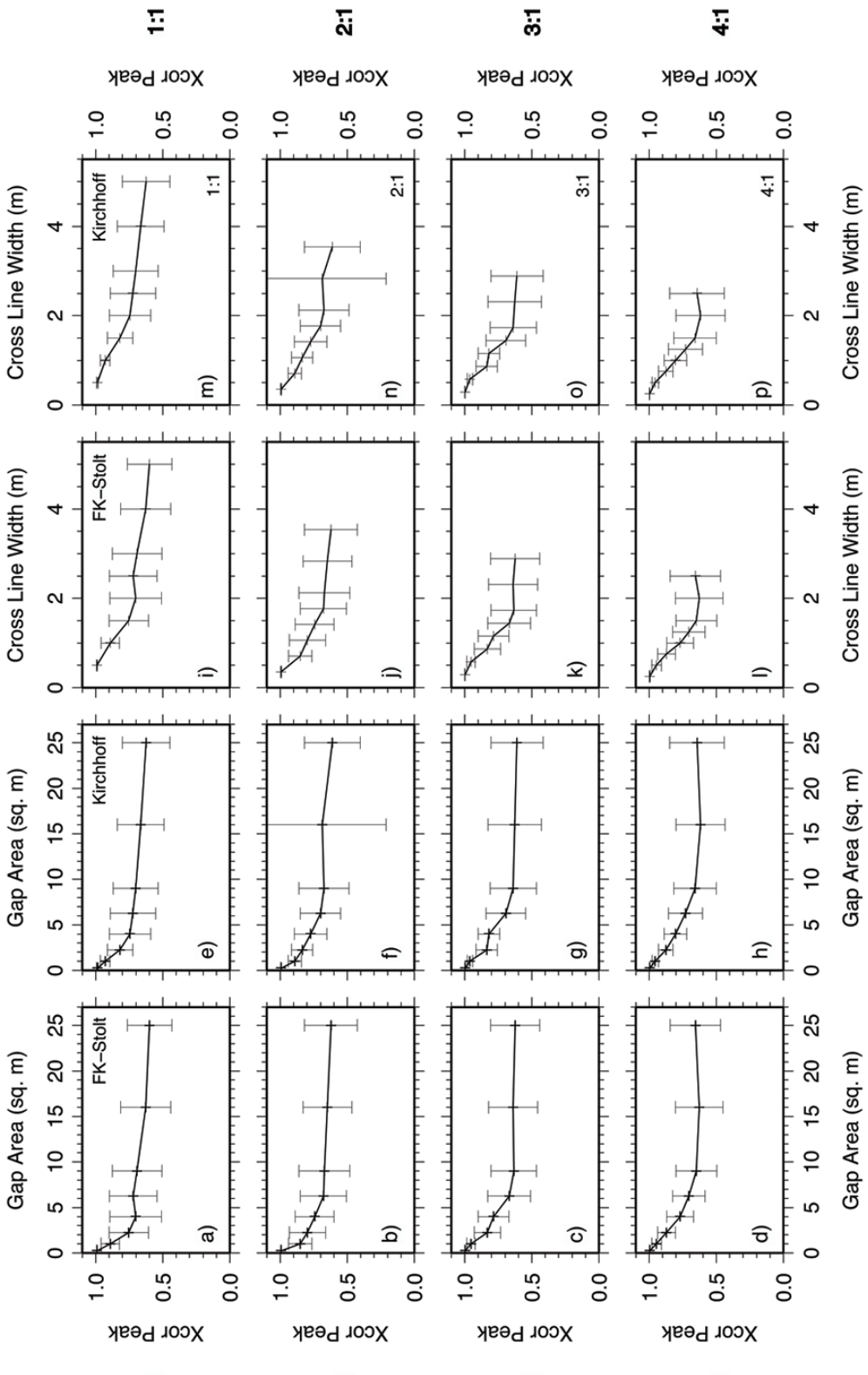

Figure 4.14: Volumetric cross–correlations calculated between fully sampled volume and gapped volumes for missing region, imaged using fk–Stolt and Kirchhoff migration. Volume contained a sinusoidal reflector of 6.0 m wavelength and 1.0 m peak–to–peak amplitude, centred around 10.0 m depth. Each row shows results for gaps of a different inline to cross–line width ratio; 1:1, 2:1, 3:1, and 4:1, respectively. While first pair of columns show results normalised to gap surface area, and second pair to cross–line width.

the CMP coverage get more asymmetrical, the maximum size of the smaller width axis must correspondingly decrease in order to preserve a similar Fresnel Zone contribution.

Statistical comparison of reflector amplitudes and volumetric cross–correlations suggest that the post–stack fk–Stolt and pre–stack Kirchhoff migration results are similar. Vertical sections through the imaged volumes (Figure 4.13), however, show a significant increase in the amount of aliased energy moved to shallower times for the post–stack imaged volume. While the reflectors in the pre–stack imaged volume remain interpretable for gap widths of 2.0 m (4.0 m^2), in the post–stack volume reflectors become increasingly dominated by incoherent energy contributions, particularly around the peak of the sinusoid, making reliable interpretation of the reflector shape difficult.

The results in this subsection suggest that, for synthetic data at least, post–stack fk–Stolt and pre–stack Kirchhoff migrations produce comparable results. There is a slight increase in uncancelled noise in the post–stack imaged volumes, but both methods demonstrate approximately the same gap reconstruction limits for both simple and complex reflectors; with complex reflector reconstruction being highly sensitive to the spatial discontinuities shape.

4.2.2 Real Data Benchmark

Although analysis of migration techniques using a series of synthetic volumes allows the effect of various parameters to be analysed independently, it does not accurately represent the irregularities in the acquisition geometry. Gaps of various shapes and sizes can be readily created by removing the appropriate subsets of the pre–stack volume, but the underlying sampling regime is consistent and regular. In real data, because of the problems with acquiring 1.0 m spaced survey lines, the sampling regime is irregular such that a gap in coverage may be bordered by a well sampled region in one direction and poorly sampled in another (e.g., see Figure 3.2), and there are likely to be

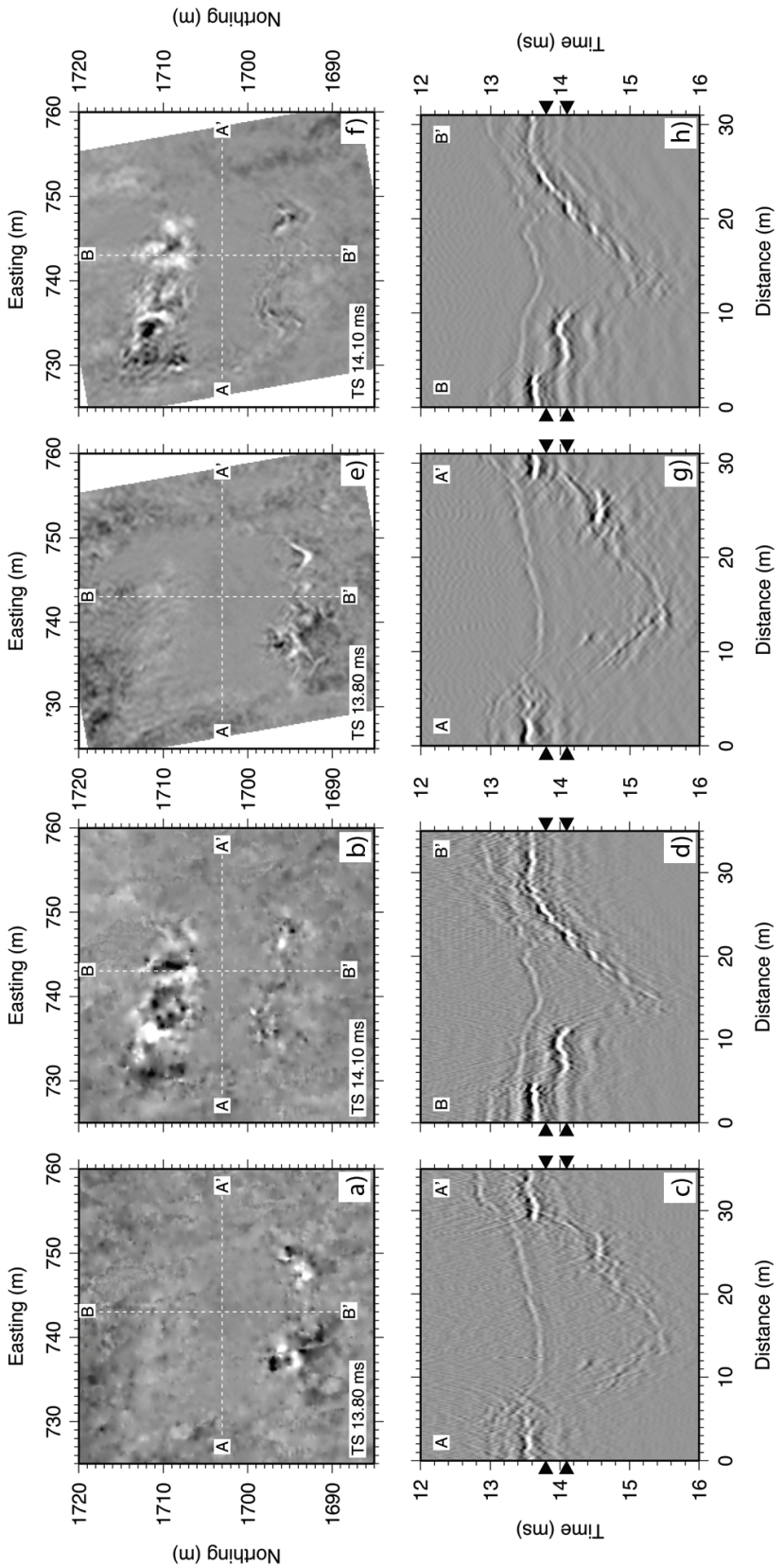

Figure 4.15: Timeslices and vertical sections through a subset volume from **Chapter 3** migrated using a two–pass, padded post–stack fk–Stolt approach, a) through d), and pre–stack Kirchhoff, e) through f), respectively.

numerous small gaps close together. Also, due to the surveying technique of strafing the study area, shot and receiver spacing are rarely regular compared to the CMP grid. Although the latter will have little effect on the pre–stack approach, where true source/receiver locations are used, this is likely have a degenerative effect on post–stack imaging (where each trace is assumed to have originated at the CMP mid–point), through a reduction in resolution and the introduction of artefacts.

Simulating these effects in synthetic data would be extremely complicated, and impossible to replicate fully. Instead, Figure 4.15 presents timeslices and vertical sections through a subset of the volume in **Chapter 3** imaged using two–pass, padded, post–stack fk–Stolt and 3D pre–stack Kirchhoff migration, respectively. Reflector reconstruction is better in the Kirchhoff volume with stronger, more continuous reflectors and less uncancelled, steeply dipping noise. Vertical sections through the fk imaged volume are contaminated by steeply dipping noise due to spatial aliasing, particularly around the crater flanks where the seabed return is almost completely overprinted. These aliasing artefacts cause stronger reflectors to become broken and discontinuous, especially where the reflector is steeper dipping. This excess of aliased noise causes timeslices through the fk imaged volume to be of lower resolution, showing less coherency between adjacent bins. While the squared crater outline is discernible in the Kirchhoff timeslices, in the fk–Stolt volume it could not be identified with any confidence. This suggests that, although post–stack fk–Stolt migration can accurately reconstruct larger gaps when the surrounding sampling is regular, if the reflected wavefield contains multiple discontinuities (as is the case for real data), pre–stack migration produces significantly improved imaging.

4.3 Conclusions

In this chapter I have considered several methods for migrating energy to the correct location within a seismic volume through deriva-

tion of their fundamental limitations. The most suitable migration algorithms, 3D Kirchhoff for the pre–stack case and two–pass padded fk–Stolt for post–stack, have been applied to several synthetic volumes and a real data subset of **Chapter 3** to compare their effectiveness in handling spatially aliased data under a number of different conditions.

The key conclusions from these results are:

- The comparison of padded post–stack fk–Stolt and pre–stack 3D Kirchhoff migration using synthetic volumes suggests similar reflector reconstruction across data gaps for simple reflector geometries. The limiting reconstructible gap width being approximately equal to twice the Fresnel zone radius.
- Although not apparent when reconstructing simple, flat reflectors, for both pre– and post–stack migration, having symmetric data gaps is preferential to elongate, asymmetrical ones where the reflector is complex. For the 6.0 m wavelength sinusoid, modelling suggests gaps $\leq$ 2.0 m in size can be filled to an interpretable level for the symmetric case. When the gaps become asymmetric, this limit decreases to $\leq$ 1.5 m, $\leq$ 1.25 m, $\leq$ 1.0 m for the smallest width axis using asymmetries of 2:1, 3:1, and 4:1, respectively.
- When the same methods are applied to real data the padded, post–stack fk–Stolt migration generates a significant number of artefacts as a result of the spatial aliasing. Vertical sections are contaminated by a large amount of steeply dipping energy, while timeslices demonstrate poor coherence between adjacent bins, resulting in a considerable reduction in resolution. In comparison, the 3D Kirchhoff imaged volume contains minimal aliased energy, although the anti–alias filtering degrades the imaging of steeper dips.

Therefore, it has been found that pre–stack 3D time migration by Kirchhoff summation results in the highest resolution imaged volume with the lowest contamination of spatial aliasing artefacts. However, applying a Kirchhoff migration, as implemented by ProMAX, to a full 3D Chirp volume is unfeasible. On an 8 Core workstation with

16 GB of RAM, the sub–volume from **Chapter 3** requires 54 hours of processing time. Scaling this up to the full volume, the processing time can be estimated as c. 23 days. Consider that this survey, although containing a large number of traces ($> 20,000,000$), only requires times between 10.0 ms and 18.0 ms to be migrated. For the shelf application thought experiment introduced in **Chapter 2**, where times between 60 ms and 100 ms would require migrating, the processing time would be substantially larger. Conversely, it is also these shelf–type applications where the requirement for migration is greatest since the larger depths lead to a higher proportion of diffracted energy content. As a result, it is necessary to think about how the Kirchhoff migration technique can be speeded up without compromising the imaging results.

"Why do you want to come into physics? All is done and understood."

Gustav Kirchhoff (1824–1887)
to Max Planck (1858–1947)

5

Frequency Approximated 3D Pre–Stack Kirchhoff Time Migration

In **Chapters 3** and **4** it has been shown that, while 3D pre–stack Kirchhoff time migration is the most effective method of accommodating the irregular spatial sampling inherent to all 3D Chirp surveys, it is also too computationally intensive for imaging whole volumes. In this Chapter I develop a different approach to 3D pre–stack Kirchhoff time migration. Correlation with a set of bandwidth limited Chirp sweeps is used to generate a series of band limited traces to be Kirchhoff migrated using coefficients determined at their central frequencies, thereby reducing the number of calculations necessary whilst maintaining the full frequency bandwidth. Combined with a traveltime correction look–up table, multi–threading, and compiler optimisation through code reorganisation and loop vectorisation, a speed increase of $> 6.5\times$ over traditional Kirchhoff approaches was

attained, without any significant image degradation. The effectiveness of this new algorithm is demonstrated through comparison using synthetic and real data sets from **Chapter 4**.

5.1 Frequency Approximated Kirchhoff Migration

As described in **Chapter 4**, the equation to be analytically solved for 3D pre–stack Kirchhoff migration is:

$$I(\xi) = \int_A W(x, y, z, t) \int_\omega i\omega P(x, y, z, \omega) e^{-i\omega t} d\omega dA; \tag{5.1}$$

where $p(x, y, z, \omega)$ is the recorded wavefield decomposed into a monochromatic trace of frequency, ω.

This frequency decomposition of the recorded time series is normally achieved using a discrete–time short–time Fourier transform (STFT):

$$X(m, \omega) = \sum_{n=-\infty}^{\infty} x(n)\omega(n - m)e^{-i\omega n}. \tag{5.2}$$

A recording sample rate of 20 μs (**Chapter 2**) in the time–domain equates to a Nyquist frequency of 25.0 kHz. Although this means we are only interested in c. half the frequencies output by the Fourier transform, when considering the shelf application thought experiment introduced in **Chapter 2**, this equates to $\geq$ 2000 frequency samples, or $\geq$ 4000 including negative frequencies. Therefore, treating the Kirchhoff integral as the sum over frequency decomposed traces increases the number of traces to be migrated by a factor of several thousand. For the shelf application this would result in the independent migration of 30 or 40 billion traces as opposed to c. 15 million, which is a considerable increase in computational expense.

This sampling regime gives a frequency–domain sample interval of 6.25 Hz. The multiplication by i in Equation 5.1 is equivalent to phase shifting the trace amplitudes by -90 degrees. Therefore, in a

1500 ms^{-1} velocity field, our frequency–domain sampling interval is equivalent to a change in the traveltime correction of 0.063 ms, which is c. half the theoretical resolution limit of the broadband Chirp sweeps (Plets, 2007). Correcting this oversampling of the frequency–domain (by at least a factor of 2) is an optimisation approach that has been used frequently for inversion algorithms (e.g., Sirgue and Pratt, 2004).

Pre–correlation, Chirp traces are already frequency decomposed due to the output sweep's linearly changing frequency content. Since time–domain correlation combines acting as a bandpass filter along with wavelet compression, correlation with a series of band limited sweeps (Figure 5.1) will result in a set of narrow band traces. These data could then be migrated according to:

$$I(\xi) = \sum_{A} W(x, y, z, t) \sum_{\omega=1}^{N_\omega} i\omega_c p_\omega(x, y, z); \tag{5.3}$$

where N_ω is the number frequency bands used, and ω_c the central frequency for each band. The validity of Equation 5.3 is dependent upon the frequency bands being narrow enough for ω_c to be representative of the band as a whole.

Now the data is not being Fourier transformed, the multiplication by i has to be approximated. This can be done as a straight -90 degree phase shift based on the central frequency, ω_c, using interpolation to accommodate $\lambda/4 \neq \Delta t$. Alternatively, taking the Hilbert transform post–correlation will also approximate the phase shift. If the traces were truly monochromatic, the Hilbert transform is exactly equivalent to a -90 degree phase shift (since, if $f(t) = sin(x)$, $H(f(t)) = -cos(x)$), but for band limited signals this relationship no longer holds exactly. With appropriately narrow bands, however, Bedrosian's Theorem shows that it will be a close approximation (Bedrosian, 1963).

Although simple linear interpolation is accurate enough to perform the phase shift, it results in a significant increase in the number of

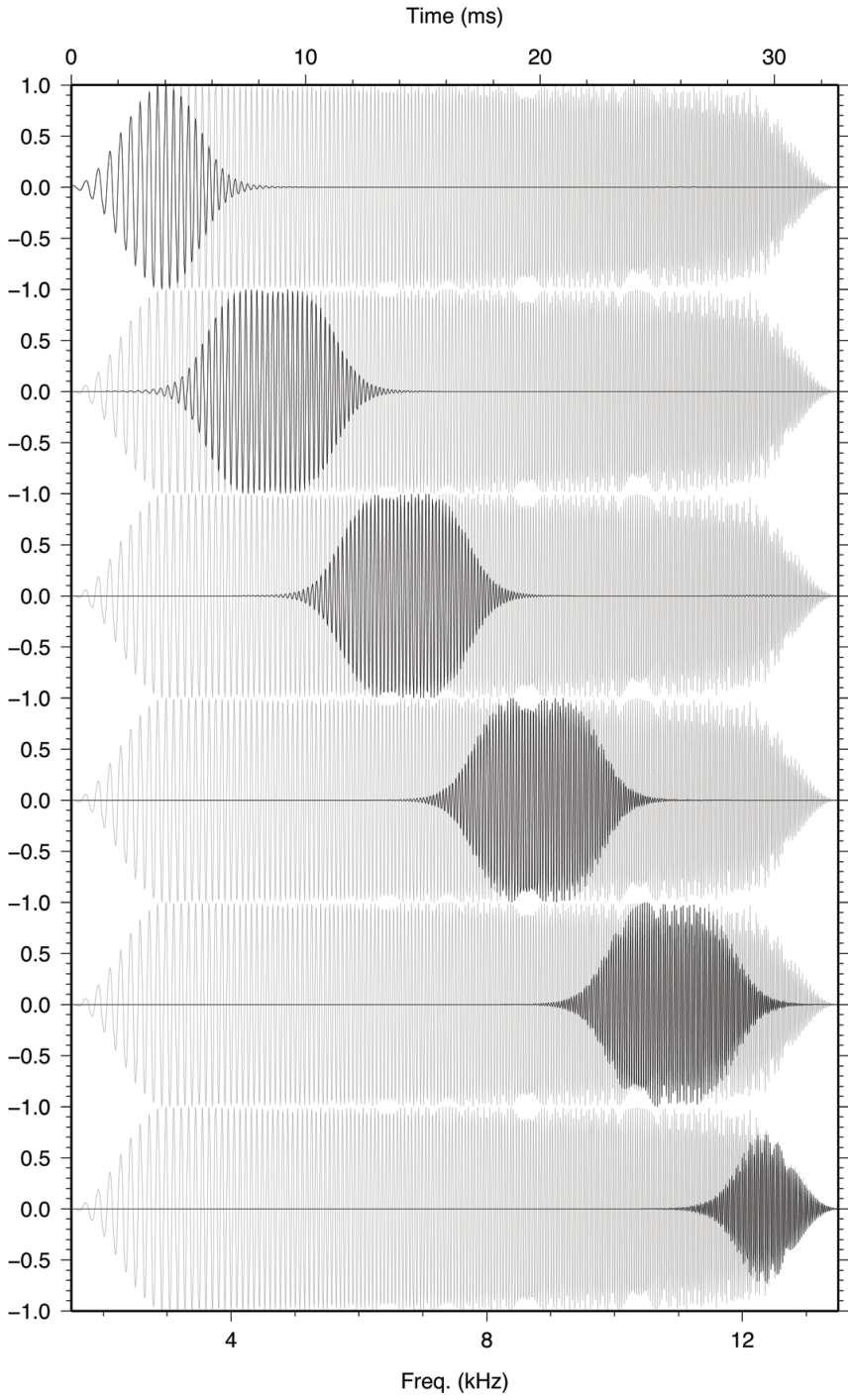

Figure 5.1: Figure showing a family of six equally spaced band limited sweeps with which the raw traces can be correlated to produce a set of six band limited traces for migration using Equation 5.3.

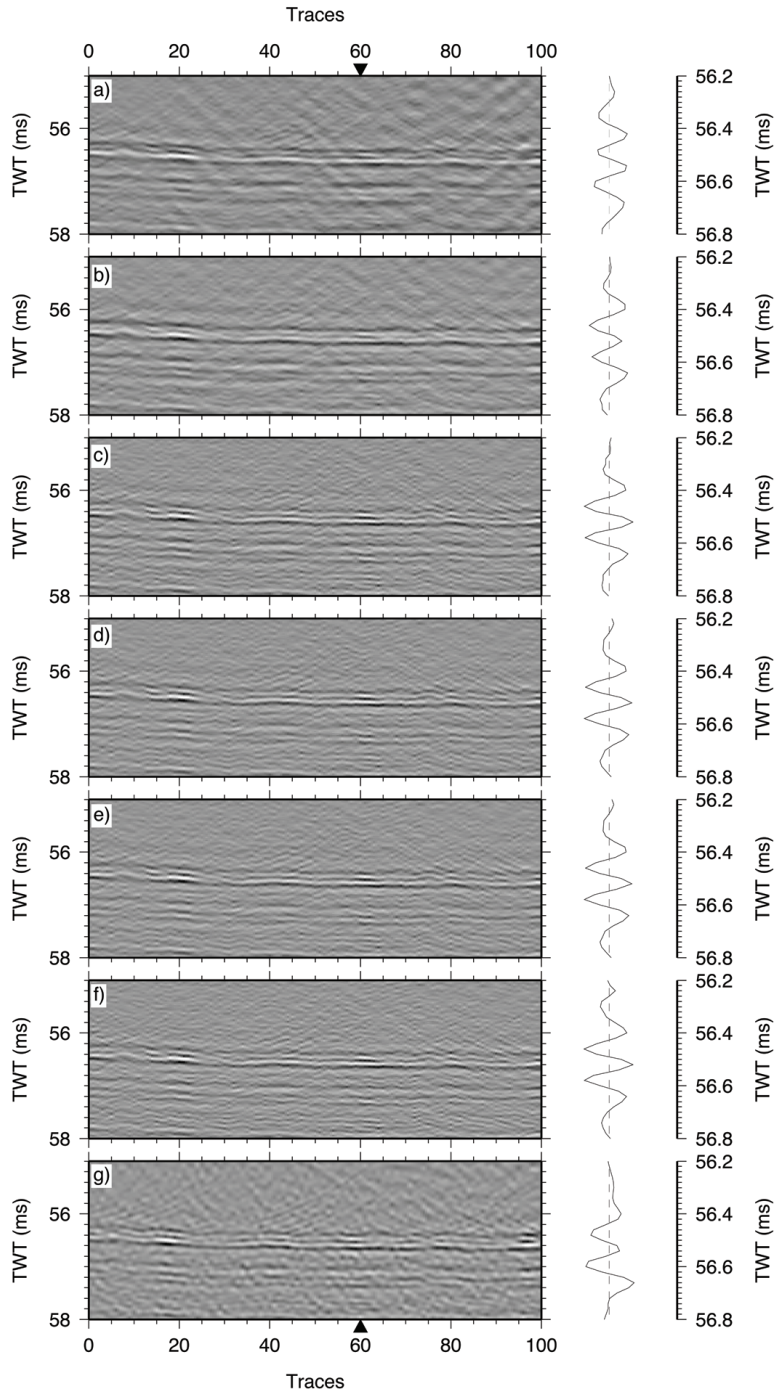

Figure 5.2: Figure showing a 2D section and seabed wavelet extracted from trace 60, imaged using (a) diffraction stack migration, together with (b–f) Kirchhoff migration using 2, 3, 4, 5, and 6 band limited sweeps. Results generated using 4, 5, and 6 band limited sweeps are almost identical, and compare well with section (g), migrated using full pre–stack Kirchhoff migration.

floating point operations required. Therefore, the Hilbert transform approach was preferred, since it can be considered as convolution with the Hilbert operator. Equation 5.3 becomes:

$$\boxed{I(\xi) = \sum_{A} W(x, y, z, t) \sum_{\omega=1}^{N_\omega} -\omega H(x, y, z, \omega);} \tag{5.4}$$

where $H(x, y, z, \omega)$ is trace $p_\omega(x, y, z)$ after Hilbert transform.

In this manner, the frequency–domain sampling can be controlled to levels more suitable to the frequency sensitivity of the final image. Figure 5.2 shows a 2D section and seabed wavelet imaged using diffraction stack migration (i.e., entire data as single frequency band), a), together with Kirchhoff migration using 2, 3, 4, 5, and 6 band limited sweeps, b) through f). Results obtained using 4, 5, and 6 band limited sweeps are almost identical, and are consistent with those obtained by a full treatment of the frequency–domain, panel g). This indicates that, within the resolution limits of the final image, for an approximately flat reflector the central frequencies become representative of the band limited traces when correlated with ≥ 4 band limited sweeps. As reflector dip increases more bands will be required to effectively describe the frequency content (particularly for higher frequencies), therefore the six equally spaced bands shown in Figure 5.1 were preferred.

5.2 Algorithm Optimisation

There are two basic approaches to writing a Kirchhoff migration algorithm: the gathering method, where each location in image space is looped through gathering contributions from the surrounding traces; and the spraying method, where each trace is loaded sequentially and contributions added to the surrounding image gather (Biondi, 2007). Although, conceptually, the gathering method is the easiest to understand, and has the advantage of resulting in a completed image trace after each iteration, given the ratio of traces pre– to post–migration

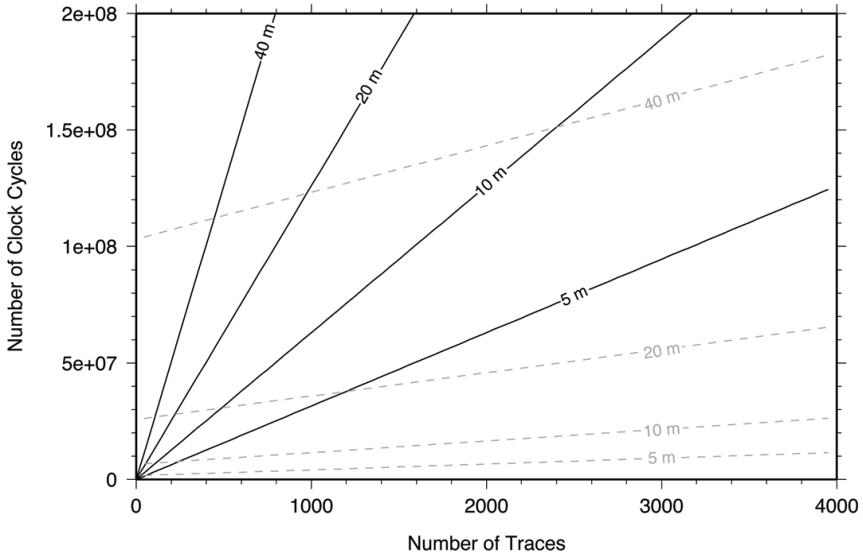

Figure 5.3: Figure showing theoretical number of clock cycles taken to process each trace for a series of aperture sizes when solving the wavefield each time (black lines), and using a traveltime lookup table (grey lines).

($\geq$ 10 million pre– to c. 0.4 million post–stack), it is not the most sensible approach from a coding perspective (Kao, 1992).

The shelf application thought experiment introduced in **Chapter 2** includes c. 15 million traces, each with 5000 time samples, of which the lower c. 3000 will be migrated. After frequency decomposition using correlation with band–limited chirp source sweeps, this 4.5×10^{10} samples becomes 2.7×10^{11} samples. Each will be stored in memory as a 4–byte float, therefore requiring 1006 GB of memory. In comparison, the post–migrated volume is effectively stacked, and a survey is unlikely to exceed 300 x 300 m, which is equivalent to 5.76 million traces using a 12.5 x 12.5 cm grid. At 3000 samples each, those 5.76 million traces becomes 1.8×10^{10} samples, or 64 GB of memory. Although, even this is more memory than is available on any of our current systems, the use of a sprayed algorithm on such a data set would require the volume to be divided into only 4 separately processed sub–volumes, as opposed to the > 40 sub–volumes required if using a gathering method.

There is a second advantage to adopting the sprayed approach, which originates in the limited velocity sensitivity of the 3D Chirp array and our constant velocity model assumption (**Chapter 4**). In a constant velocity field, the traveltime corrections across a migration aperture remain constant from trace–to–trace for common source–receiver pairs. Therefore, a look–up table of traveltime corrections can be generated once, prior to reading any trace information. The number of floating point calculations performed for a migration are then reduced from the number of sample–migration aperture location pairs multiplied by the number of input traces, to the number of sample–migration aperture location pairs multiplied by the offset–domain sampling. Theoretically, this should produce a speed advantage proportional to the ratio of traces to offset samples ($\sim 1/500,000$ for most surveys). Although, some remaining floating point operations mean this efficiency is never attained, substantial gains are made even for relatively few input traces (Figure 5.3).

5.2.1 Non Zero–Offset Wavefield

Although, prior to migration, traces are binned onto a CMP grid, the Kirchhoff operator is based upon the true source and receiver positions. In the constant velocity time migration case, the traveltime corrections can be solved as a Pythagorean triangle of recorded and horizontal TWT:

$$\tau = \sqrt{t^2 - (h_s + h_g)^2}; \tag{5.5}$$

where t and τ are the input and output TWT, while h_s and h_g are the source–to–aperture location and receiver–to–aperture location, respectively:

$$\begin{aligned} h_s &= \sqrt{(x - x_s)^2 + (y - y_s)^2}, \\ h_g &= \sqrt{(x - x_g)^2 + (y - y_g)^2}; \end{aligned} \tag{5.6}$$

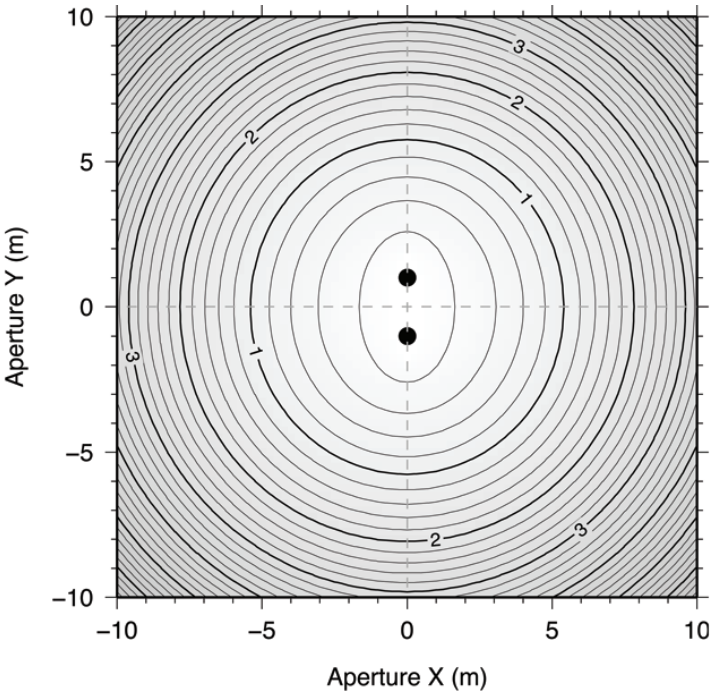

Figure 5.4: Figure showing symmetrical nature of pre–stack Kirchhoff operator. Traveltime corrections are contoured at 0.2 ms intervals, and shaded with increasing dip angle. Source and receiver locations are indicated by black circles, and dashed grey lines axes of symmetry.

where x and y are the image trace location, while x_s and y_s, and x_g and y_g are the source and receiver locations, respectively.

A look–up table of traveltime corrections calculated using Equation 5.5 and Equation Array 5.6 would be dependent upon x, y location within the migration aperture, original traveltime, and source–receiver offset. In addition, since this operator is then mapped onto a quantised grid, it also depends on the source–receiver azimuth relative to the grid $(x1, x2)$ directions. Therefore, a full travetime correction look–up table would be a 5D matrix.

A calculation using parameters for the shelf thought experiment (25 m aperture radius, 5000 time samples, 32 offset samples, and 360 azimuthal samples; **Chapter 2**), quickly demonstrates that such a look–up table is unfeasible (2.304×10^{12} samples $\equiv$ 8584 GB of memory). A better approach is to populate a 4D matrix of traveltime corrections assuming a source/receiver azimuth parallel to the y–axis, and accommodate the azimuthal dependancy as a separate translation. This translation is required once for each migration aperture location and input trace pair, so does not have a substantial effect on

algorithm efficiency. Additionally, with a constant velocity the wavefield has 2 lines of symmetry parallel to the x– and y–axes (Figure 5.4), allowing the look–up table to be only 1/4 the size of the migration aperture. The reduction in floating point operations by generating a look–up table of traveltime corrections decreases processing time of a test synthetic volume from 31 hours 3 minutes to 2 hours 40 minutes (Table 5.1).

Following this approach, the 3D pre–stack Kirchhoff algorithm takes the general form shown in Figure 5.5. Consisting of an initial generation of the traveltime correction look–up table, followed by sequentially reading each trace into memory and mapping across the migration aperture onto the output volume.

5.2.2 Multi–Threading

The Kirchhoff approach to time imaging is computationally intensive, with a large number of floating–point operations required for each trace. Lumley and Biondi (1991), Cabrera et al. (1992), and Kao (1992) have all shown that large increases in efficiency result from taking advantage of shared memory multiple CPU or multiple Core systems to perform these operations in parallel. Theoretically, the optimal parallelization, such that all parallel tasks are equally balanced, should result in a decrease in processing time proportional to the number of processors. However, this theoretical maximum is never attained due to a combination of: system overheads; cross–task dependancies; and non–complete parallelization of the algorithm (e.g., see Kao, 1992).

Kirchhoff algorithms naturally lend themselves to being parallelized, particularly when using the sprayed approach, because, within a single migration aperture, the process is non–iterative. Therefore, parallelization of the aperture–loop region of the algorithm (Figure 5.5) removes any cross–task dependencies. Since memory and core management overheads are small on modern systems, the discrepancy between

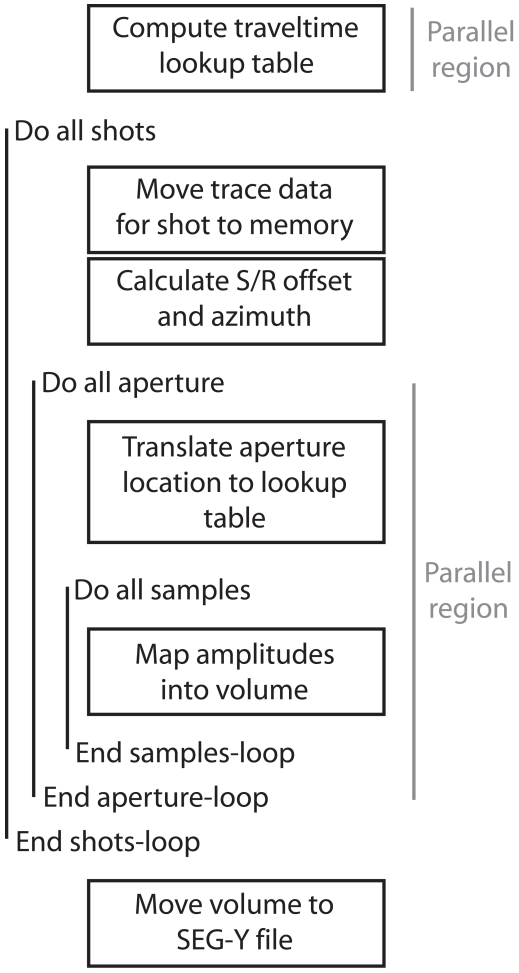

Figure 5.5: Schematic representation of pre–stack 3D Kirchhoff time migration algorithm for a constant velocity field.

theoretical and maintainable efficiency is dominated by the percentage of code running single–threaded. Parallelization of this region of the algorithm, both during look–up table generation and migration, minimises the number of single–threaded floating–point operations, leaving only data input/output and model initialisation.

When trying to parallelize non–iterative functions in C++, there are a number of different approaches that can be taken:

1. **ICC Auto–Parallelization:** Compilation using the Intel icc C++ compiler allows an auto–parallelization function to be specified using the *-parallel* flag. Although easy to implement and effective on small, simple algorithms, auto–parallelization functions struggle when dealing with more complicated code, particularly where there are embedded loops. As a result, *icc -parallel* is not suitable for parallelizing a pre–stack Kirchhoff code which naturally involves multiple embedded for–loops to move through $modl[\,]$ space ($x1$, $x2$, z).
2. **fork()/vfork():** Standard Unix function(s) to fork a parent process into multiple identical child processes. Originally, *vfork()* differed from *fork()* in that the parent process is suspended for the duration that the child process is active so that the memory addresses can be shared, thereby lowering overheads. However, in modern Unix/Linux systems the functionality of *fork()* has developed enormously, such that *vfork()*, if present, redirects to *fork*. The overheads involved with creating an entirely new process are large compared with spawning a series of sub–processes, or threads, meaning that *fork()* is generally reserved for when another process is required to help with the work–load.
3. **Pthread:** A set of procedures developed from the IEEE POSIX 1003.1c standard (1995) to spawn a series of sub–processes, or threads, which are implemented using *pthread.h*. As long as processes can be interleaved, interchanged, and/or overlapped, *Pthreads* offers a highly effective way of parallel executions since the majority of overheads of the original process are shared, with

only the minimum amount of resources required to maintain independent flow control.

4. **OpenMP:** An Application Program Interface (API) for C++ and Fortran (Simons et al., 2008), which allows multithreading and shared memory parallelization using the fork–join approach. This can be explicitly targeted at specific blocks of code using one or more of the *# pragma omp* compiler directives. Each of these directives has a series of clauses that allow it to be tailored for specific applications, making OpenMP a flexible way of optimising non–iterative loops.

Although Pthread and OpenMP are both suitable for this application and demonstrate similar efficiency increases (Barney, 1995), the latter method was chosen due to ease of implementation. With OpenMP you define regions you want to run in parallel using a compiler directive and associated clauses.

The region to be parallelized is defined using the *parallel* directive:

```
# pragma omp parallel numthreads(nthreads) \
    shared() \
    private()
    {
    Parallelized region
    }
```

Specifying the variables shared between threads, `shared()`, and those private to each thread, `private()`.

The for–loop to be parallelized is then explicitly targeted using the *for* directive:

```
# pragma omp for schedule (static)
```

The speed increase attained by multi–threading the code is substantial. For the fully sampled synthetic data set and real data sub–volume used in **Chapter 4**, Table 5.1 compares runtimes for the frequency

Change	Freq. approx. Kirchhoff	Diffraction Stack	fk–Stolt	Full Kirchhoff
Synthetic Volume				
Basic pre–stack code	31 hr 3 min	-	-	-
Look–up table	2 hr 40 min	-	-	-
Multi–thread	0 hr 21 min	-	-	-
Compiler optimisation	0 hr 19 min	-	-	-
Final	**0 hr 19 min**	**0 hr 8 min**	**0 hr 3 min**	**2 hr 39 min**
Crater				
Final	**0 hr 51 min**	**0 hr 23 min**	**0 hr 10 min**	**56 hr 0 min**

Table 5.1: Summary of migration run times for completely sampled synthetic volume of 6 m wavelength sinusoidal reflector and sub–volume from **Chapter 3**.

approximated Kirchhoff code with diffraction stack, fk–Stolt, and full Kirchhoff migration algorithms (all on an eight core workstation). For the synthetic volume with c. 274,000 input traces, a speed increase of $\geq 6.5\times$ the ProMAX full Kirchhoff algorithm is attained. For the real data sub–volume, which contains c. 2,100,000 input traces, the runtime reduces by $\geq 60\times$. This reflects the ProMAX algorithm being more efficient at initialising the look–up table, but being more sensitive to greater trace numbers by generating the look–up table multiple times.

5.2.3 Compiler Optimisation

Along with optimising algorithm efficiency through lookup tables and parallelization, there are also gains to be made using optimisation flags during compilation. These directives control how the compiler reads and rewrites the code, affecting the size and order of the final executable, along with the accuracy to which values are stored in memory or registry during calculations.

When compiling the executable using the Intel *icc* compiler, the options available are:

1. **Inlining:** Speed advantages can be gained by removing excess space from the final executable. Inlining shortens *if*, *elseif*, and

other statements, theoretically making them more efficient to process. Changing the levels of inlining using *–inline–level=<n>* and *–ip* had no appreciable effect on efficiency. The only discernible difference came when the compiler was explicitly told to inline *calloc()* calls to independent *malloc()* and *memset()* statements, *–inline–calloc*, reducing runtime by $\sim 5\%$.

2. **Machine Specific Compilation:** There are 2 options for machine specific compilation: *–mtune* which controls reordering of the executable code such that it is optimised for the specific macro–architecture, theoretically resulting in compatibility across chips with the same macro–architecture; and *–mcpu* which reorders the executable code to be CPU specific, therefore producing a code which is executable only on CPU's with the same macro– and micro–architectures. Using *–mcpu=core2* to compile for the micro–architecture resulted in a $\sim 2.5\%$ improvement in runtime efficiency.
3. **–O flag:** In the Intel icc C++ compiler, the *–O* flag controls how aggressively the compiler rearranges the human readable code. The most aggressive setting, *–O3*, was found to shorten computation time by $\sim 5\%$ compared with the default setting, *–O2*.
4. **Streamed SIMD Extensions (SSE):** Starting out as a set of eight extra 128–bit registers, along with 64 scalar and floating point instructions, first introduced by Intel in 1999, this has now expanded, through four further revisions (SSE2, SSE3, SSSE3, and SSE4), to include 16 extra 128–bit registers and a total of 291 instructions to perform mathematical transforms on data of any type (8–bit through to 16–bit). Although Kirchhoff imaging requires a large number of calculations, these calculations are relatively simplistic and performed on 32–bit data, these combine to reduce SSE optimisation to $< 2\%$.
5. **Unroll:** The opposite of inlining, this removes the end–of–loop flags and therefore loop controller overheads, but at the disadvantage of generally making the final executable larger. As with inlining, in the correct situation this can lead to a significant speed

advantage. However, neither a standard, *–unroll*, nor aggressive, *–unroll–aggressive*, heuristic approach improved runtime.

6. **Valgrind:** Is a collection of tools for debugging programs, with particular emphasis on the memory management and threading. The Memcheck utility was used to verify there were no memory leaks or badly address blocks.

By optimising the compiled executable using inlining, micro–architecture specific, and SSE4 loop vectorization, an overall speed gain of $\sim 6\%$ was attained. This reduced the migration time from c. 21 min 10 sec to c. 19 min 50 sec (Table 5.1).

5.3 Imaging Optimisation

5.3.1 Weight Function

Traditionally, Kirchhoff migration is formulated as a pure imaging process with little regard for the 'correctness' of reflector amplitudes, just that dip angle and time/depth are correct (e.g., Schneider, 1978). If, however, the contributions of each equal traveltime curve (or Green's function) is correctly weighted, the amplitudes will be proportional to the reflection strength (Docherty, 1991). From an inversion perspective, Bleistein (1987) derives a weighting function using the Wentzel–Kramers–Brillouin–Jeffreys (WKBJ) approximation and shows it to be equivalent to the geometric optics reflection coefficient.

$$W(x, y, z, t) = \frac{\Delta \boldsymbol{\tau}_G}{\pi} \frac{A_s}{A_g}; \tag{5.7}$$

where A_s and A_g are the source and receiver Green's function amplitudes respectively, and $\Delta \boldsymbol{\tau}_G$ is the wavefield directional vector at the surface.

For the constant velocity special case (and within the limit of weak single scattering), this can be rewritten as (Wiggins, 1984):

$$\boxed{W(x,y,z,t) = \frac{cos\theta}{2\pi v R};} \tag{5.8}$$

where R is the traveltime correction and θ the dip angle.

Docherty (1991) shows that, since migration is the adjoint of inversion, this amplitude weighting function is valid for Kirchhoff migration as well as inversion. Therefore, Equation 5.8 can be used for the $W(x,y,z,t)$ term in Equation 5.4.

5.3.2 Aliasing

As described in **Chapters 1**, **2**, and **3**, incomplete spatial sampling of the pre–stack wavefields will always be present due to the limiting physical dimensions of the 3D Chirp mat. This, in turn, will result in artefacts within the migrated volume, normally in the form of steeply dipping, high–frequency reflectors, and incomplete reflector reconstruction (**Chapter 4**). Although pre–migration interpolation or post–migration filtering in f–k or Tau–p domains can reduce the degenerative effect of this noise in the migrated volume, the only way of effectively removing these is to minimise spatial aliasing in the acquisition domain.

With Kirchhoff migration there is also a potential problem with under–sampling the wavefront in the migration aperture, known as operator aliasing (Yilmaz, 1987). Considering a 2–dimensional profile, for the location on a wavefront with slope dx/dy and spatial Nyquist frequency of k_N, temporal frequencies above ω will be aliased according to the criterion:

$$\omega > \frac{k_N}{dt/dx}. \tag{5.9}$$

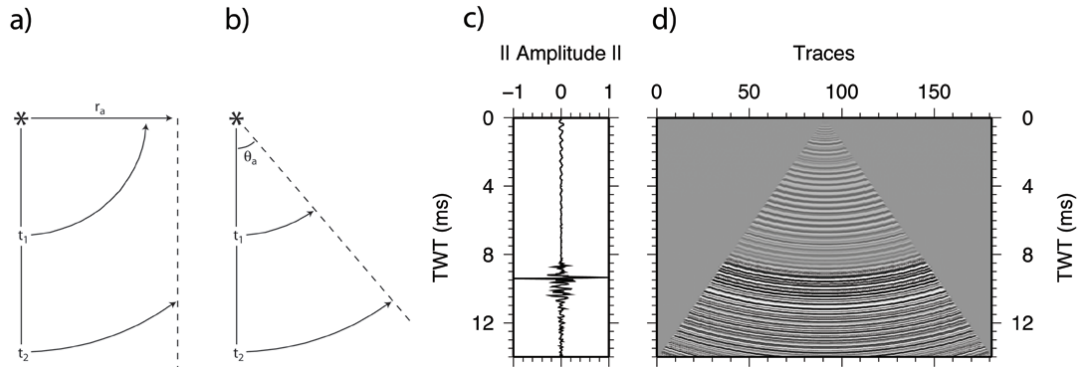

Figure 5.6: Traditional Kirchhoff imaging by migrating energy along wavefronts across an aperture of radius, r_a, leads to extremely large dip angles at shallow depths/times, a). By specifying an aperture angle, instead of radius, this energy is removed from shallow regions, b). Panel d) shows how a single input trace, c), is mapped across this angle dependent aperture.

This can be re–expressed in terms of the horizontal sampling, Δx (Bevc and Claerbout, 1997; Gray, 1992):

$$\omega > \frac{1}{2d\Delta x}; \tag{5.10}$$

where $d = dx/dy$.

Operator aliasing can occur when data is adequately spatially sampled pre–stack since, in this case, Δx is the sample interval of the migration aperture, not the acquisition sample interval. Operator aliasing is particularly prevalent at shallow depths where the dip angle of the wavefront increases rapidly with offset. This leads to $d >> \frac{1}{2\omega\Delta x}$ within a migration aperture suited to deeper targets (Figure 5.6).

As with image aliasing (**Chapter 2**), there are a number of ways to counter operator aliasing: using an array of low–pass filtered traces to approximate frequency dependent angle limiting (Gray, 1992); spatial interpolation to a higher–resolution CDP gird (Yilmaz, 1987); or various amplitude weighting functions (e.g., Bevc and Claerbout, 1997; Claerbout, 1992; Lumley et al., 1994). However, with 3D Chirp data sets, the angular variation in reflected wavefield response is limited by

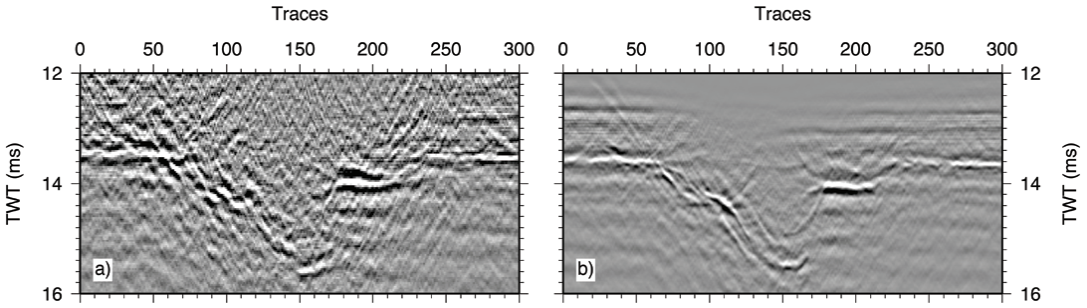

Figure 5.7: Image showing section migrated without, a), and with, b), anti–aliasing filter. By limiting the migration aperture to dip angles of 13° rather than trace location to image location distance, over migration of energy to steep dips at shallow depths is prevented. The resulting section, b), contains clean, strong reflectors, uncontaminated by steeply dipping migration artefacts.

the beam forming of the outgoing source sweep, meaning there are no real reflections from steeper dips (**Chapter 2**). This allows operator aliasing to be reduced by making the migration aperture dependant on depth (i.e., angle limited), without limiting imaging effectiveness (Figure 5.6). Since the aperture angle is measured from vertical and the reflector dip angle from horizontal, assuming normal incident reflection the two are interchangeable, making the aperture angle equivalent to the maximum reflector dip angle that will be imaged. Figure 5.7 shows how implementing this improves the interpretability of the migrated section, removing uncancelled, steeply dipping noise from deeper reflectors that overprints shallower structure.

In addition, since the solution of the seismic wavefield is being stored in memory as a 4D traveltime look–up table ($x1$, $x2$, z, h), the operator aliasing can occur in the offset domain as well as the spatial domain. Equation 2.13 can be used to express the relationship between dip angle and offset–domain sampling. From Figure 5.8 it is clear that the limiting dip angle of 15° makes direct aliasing through under–sampling of the offset–domain unlikely. Rather, the sampling interval must be sufficient to describe the source/receiver sampling intervals. It was empirically found that using offsets between 0.1 m and 1.6 m at an interval of 0.05 m was sufficient.

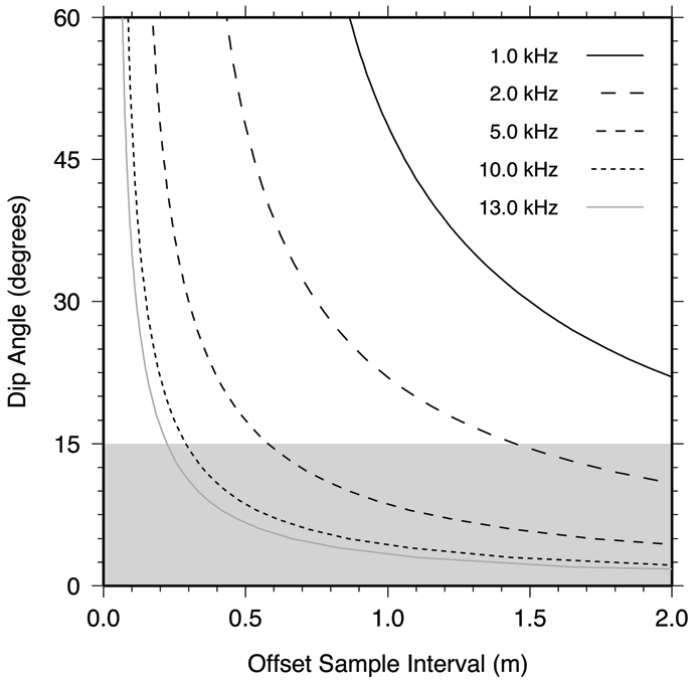

Figure 5.8: Illustration of relationship between offset sampling and dip angle aliasing, calculated using Equation 2.13. Shaded grey region are angles effectively imaged by 3D Chirp profiler.

5.4 Testing

A number of test data sets were used to verify that the frequency approximated Kirchhoff migration algorithm migrates energy in the expected manner, and does so without degenerating the interpretability of the final volume when compared to a full Fourier–transform based Kirchhoff migration. In the following section, the synthetic volume containing a sinusoidal reflector at 10.0 m depth from **Chapter 4** and a subset volume from **Chapter 3** are used for this purpose.

5.4.1 Synthetic Volume

The synthetic volume from a 6.0 m wavelength, sinusoidal reflector centred at a depth of 10.0 m (Figure 4.6) was correlated with the full Chirp sweep and a family of band limited Chirp sweeps. This allowed comparison of the imaging quality obtained by Kirchhoff migration using a full representation of the frequency bandwidth, and the simplification using six frequency bands.

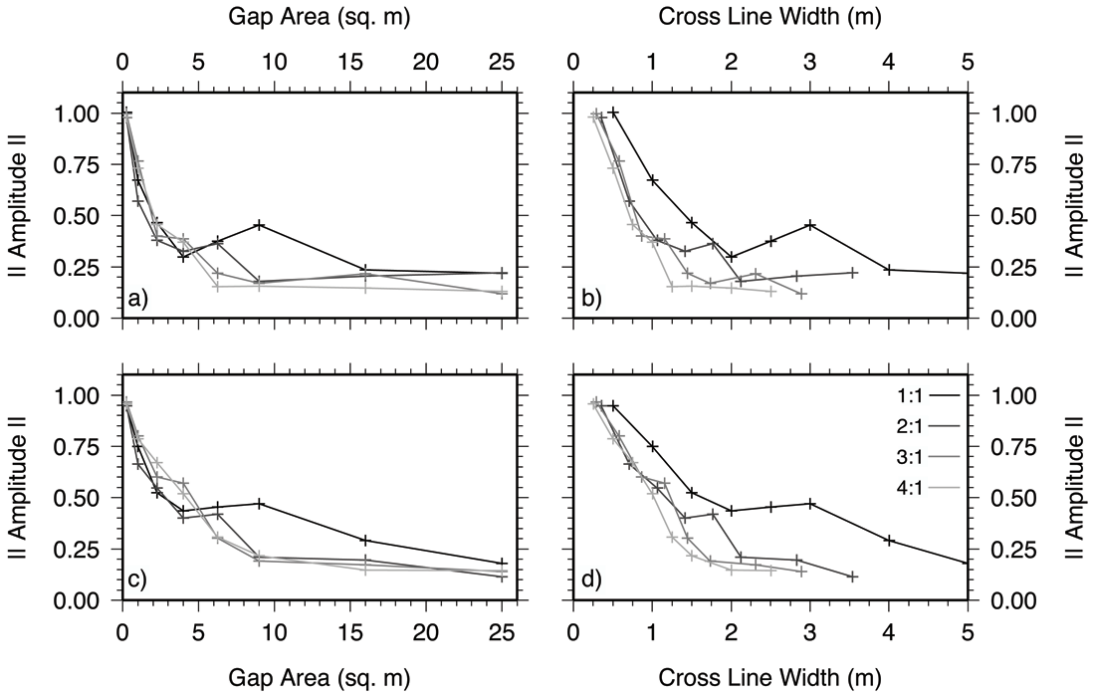

Figure 5.9: Extracted reflector amplitudes for central trace from volumes with varying gap sizes and varying gap symmetries, normalised against fully sampled volume. Panels a) and b) show results migrated using the full Kirchhoff algorithm, while c) and d) results from frequency approximated Kirchhoff migration.

Figure 5.9, compares the reflector amplitude of the central trace for a variety of gap sizes and symmetries normalised against reflector amplitude from the fully sampled volume. Panels a) and b) show results from Kirchhoff migration with complete treatment of the frequency content, while c) and d) the results from frequency approximated imaging. As explained in **Chapter 4**, amplitudes decay rapidly with increasing gap size as Fresnel zone energy contribution diminishes, until an ambient level of uncancelled noise energy dominates. Comparison of full Kirchhoff and frequency approximated results shows little difference in behaviour with varying gap size, or gap symmetry. In both cases, the reflector amplitude dips below any meaningful level with gaps > 4.0 m^2 in size, and accommodates wider (in the cross–line direction) gaps if they are symmetric.

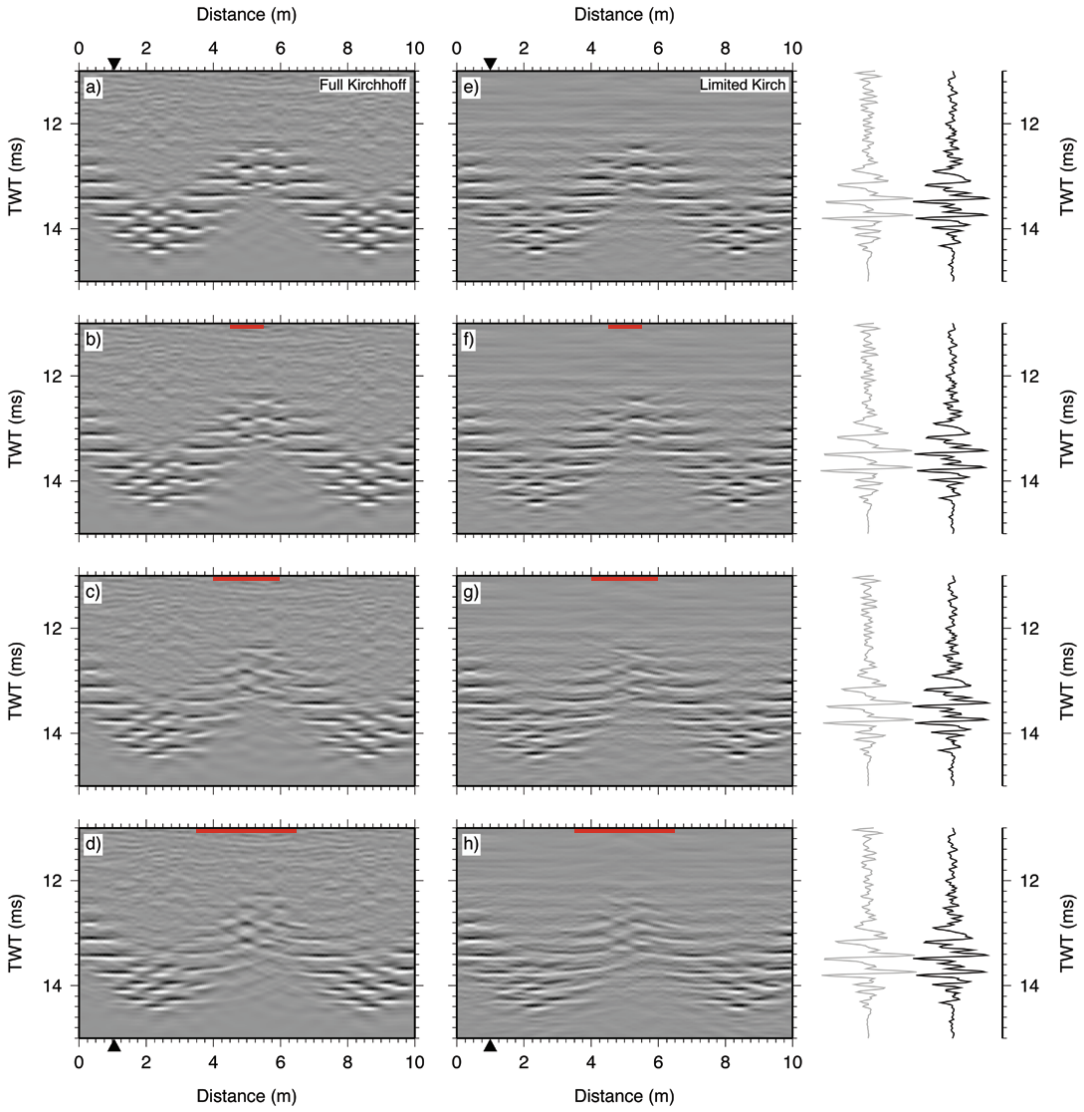

Figure 5.10: Figure showing imaged cross–line sections through full, a) through d), and band limited, e) through h), migrated volumes. Panels a) and e) are from fully sampled volumes, while b) and f), c) and g), and d) and h), contain 1.0×1.0 m, 2.0×2.0 m, and 3.0×3.0 m gaps, respectively, centred around 5.0 m into the section. Missing data indicated by red bar. Wiggle traces on right compare trace extracted 1.0 m into section from full Kirchhoff (grey line) and frequency approximated Kirchhoff (black line). Despite approximating the frequency content using only six band limited traces, there is no loss of vertical resolution and very little difference between the two traces for any of the four volumes.

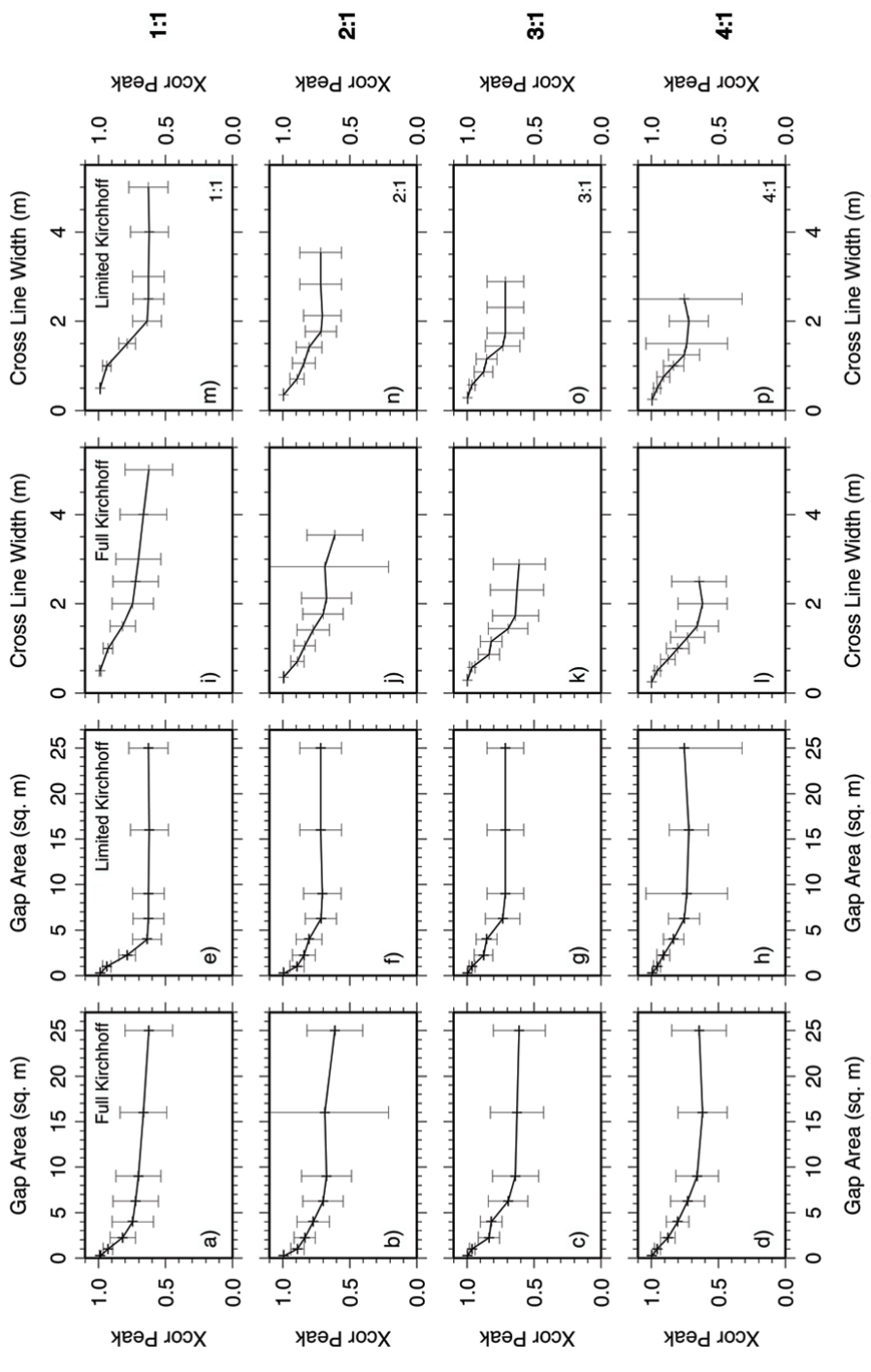

Figure 5.11: Volumetric cross–correlations calculated between fully sampled volume and gapped volumes for missing region, imaged using full and band limited Kirchhoff migration. Volume contained a sinusoidal reflector of 6.0 m wavelength and 1.0 m peak–to–peak amplitude, centred around 13.0 m depth. Each row shows results for gaps of a different inline to cross–line width ratio; 1:1, 2:1, 3:1, and 4:1, respectively. The first pair of columns show results normalised to gap surface area, and second pair to cross–line width.

This decay of reflector reconstruction is illustrated clearer in Figure 5.10, where cross–line sections through the centre of a fully sampled volume, and 3 containing 1.0×1.0 m, 2.0×2.0 m, and 3.0×3.0 m gaps are shown. For the fully sampled case, both migration methods demonstrate good reconstruction of the stepped sinusoid apart from in the peaks and troughs, where decimation of the wavefield using the phase screen method leads to anomalous internal reflections. Reconstruction of these reflections is consistent across the 1.0×1.0 m gap, and interpretable for 2.0×2.0 m gap, but becomes confused by uncancelled energy for the 3.0×3.0 m gap.

Similarly, this behaviour is seen in Figure 5.11, which compare volumetric cross–correlations (with standard deviation error bars) for the gapped regions from the full Kirchhoff and frequency approximated Kirchhoff imaged volumes. The same behaviour with differing gap sizes and symmetries is seen for both methods, although the latter appears more robust for larger gap sizes. This is likely a result of the limited amount of uncancelled diffraction energy, which is more conspicuous for full Kirchhoff imaging (Figure 5.10).

5.4.2 Real Data Benchmark

As discussed in **Chapter 4**, the irregularity of data acquired using the 3D Chirp sub–bottom profiler means that comparisons of migration methods using synthetic data sets provide only limited information. Figure 5.12 compares results from a subset volume of the data set presented in **Chapter 3** imaged using full Kirchhoff migration and frequency approximated Kirchhoff migration. For completeness, Figure 5.13 compares the same volume imaged using full Kirchhoff migration with a diffraction stack migration.

The diffraction stack migration moves energy to steeper dips, which make the timeslices crisper and easier to interpret, but the vertical sections (along with being lower resolution) are contaminated by steeply dipping, uncancelled energy. Comparison of volumes imaged using full Kirchhoff and frequency approximated Kirchhoff migrations are very

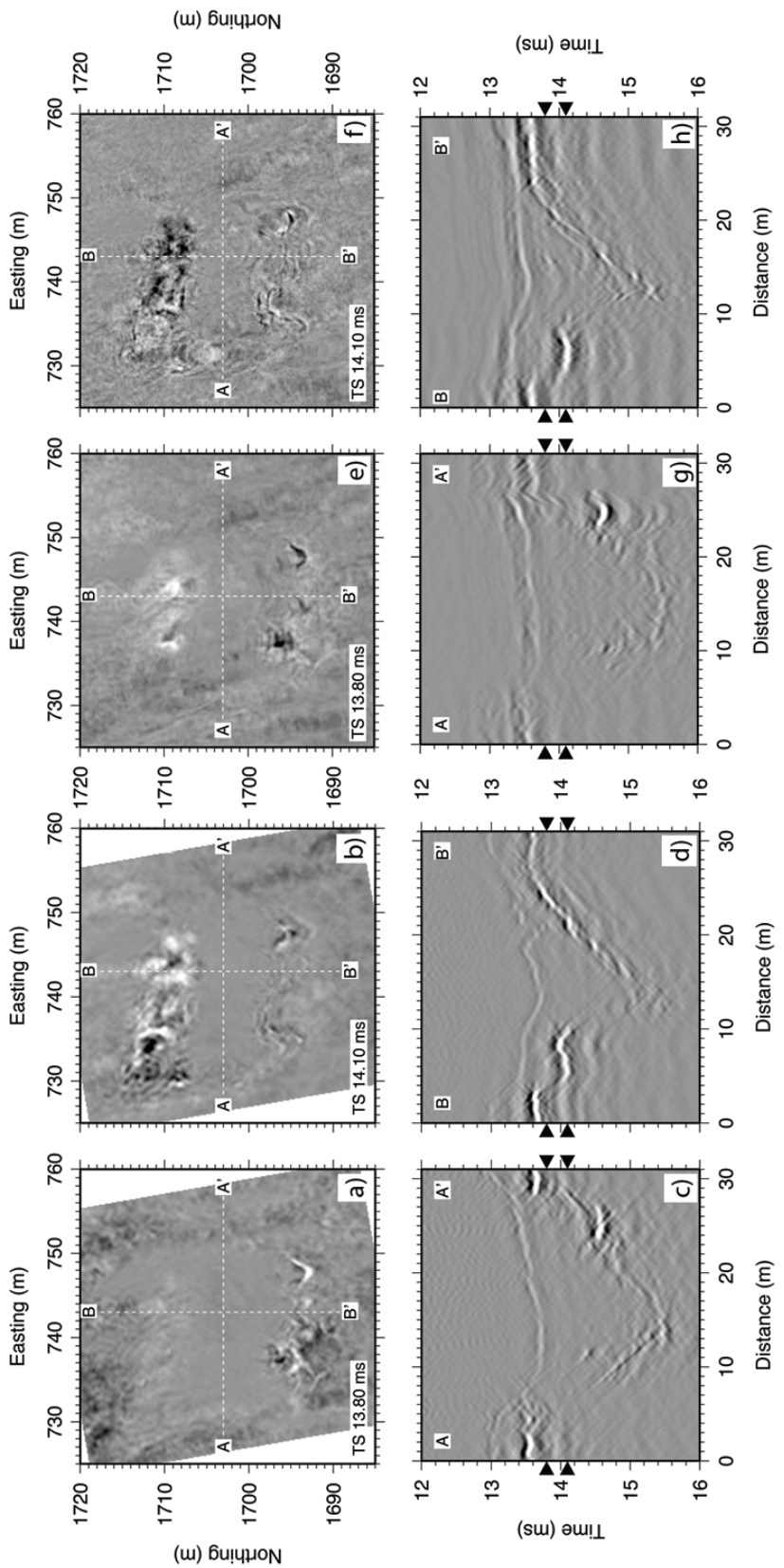

Figure 5.12: Timeslices together with inline and cross–line sections through a subset of the data presented in **Chapter 3** migrated using full Kirchhoff, panels a) through d), and frequency approximated Kirchhoff, e) through h), approaches.

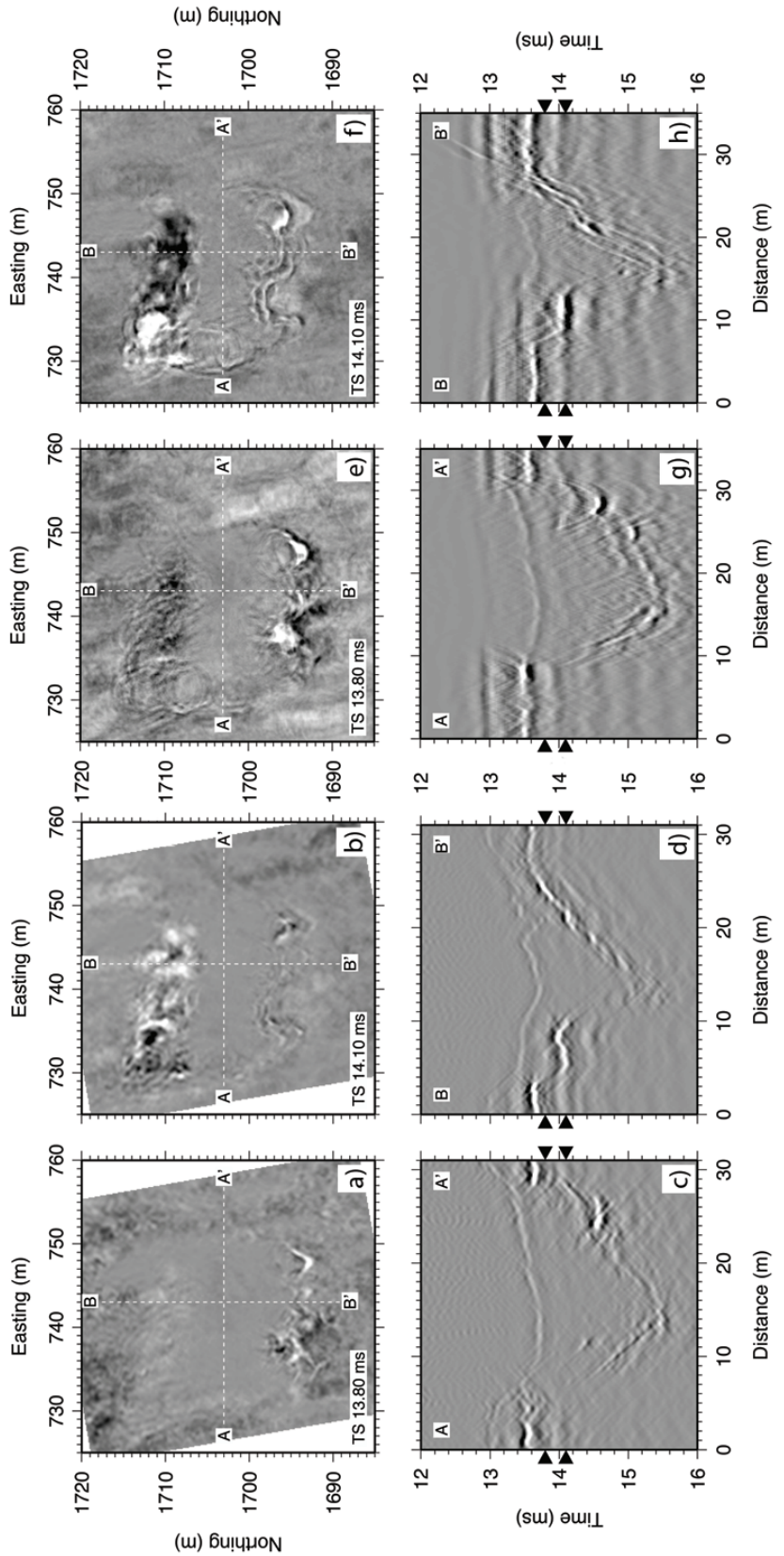

Figure 5.13: Timeslices together with inline and cross–line sections through a subset of the data presented in **Chapter 3** migrated using full Kirchhoff, panels a) through d), and diffraction stack, e) through h), approaches. Higher frequencies are clearly poorly represented by the diffraction stack method.

similar. Both demonstrate good reconstruction of the crater structure in the inline direction, and the very weak seabed reflector. However, both struggle with the cross–line direction, which is contaminated by uncancelled noise leading to the bedrock reflector being low amplitude and discontinuous. Use of the ProMAX anti–aliasing filter when migrating the full Kirchhoff volume has enabled a slightly better reconstruction of the high frequency seabed, but it appears to contain more uncancelled diffractions than the simple angle limited filtering used in the frequency approximated algorithm.

5.5 Conclusions

In this Chapter I have developed a new approach to pre–stack 3D Kirchhoff time migration using correlation with band limited Chirp sweeps to approximate the Fourier transform into monochromatic traces and a look–up table of traveltime corrections. This has resulted in vastly improved processing times without a noticeable degradation in image quality:

1. **Efficiency**: This band limited approach to Kirchhoff imaging reduces the number of traces to be migrated, while the look–up table minimises the number of floating point operations. A speed increase of $\geq 6.5-60\times$ when compared with traditional Kirchhoff methods (as implemented by ProMAX) has been obtained.
2. **Accuracy**: Comparison of imaged volumes from synthetic and real data show that appropriate frequency–domain band limiting has only small degenerative effects on the quality of the imaged volume, or reflector reconstruction where the wavefield is spatially under–sampled. Indeed, steeper dipping reflector are reconstructed better, although at the expense of a slight increase in uncancelled diffraction energy.

The increase in efficiency is such that the real data subset of **Chapter 3** used to compare traditional and band limited Kirchhoff migration

takes 51 minutes to migrate on a dual quad–core workstation. Pre–stack, this volume contains c. 2.1×10^6 traces. Assuming a pulse rate of 4 shots per second and 60 receivers, it would take 2 hours 20 minutes to acquire the same number of traces. **Therefore, the frequency approximated approach to pre–stack Kirchhoff migration derived in this Chapter could be used for real–time pre–stack 3D imaging of 3D Chirp data.**

"I wandered lonely as a cloud
That floats on high o'er vales and hills,
When all at once I saw a crowd,
A host of golden daffodils;
Beside the lake, beneath the trees,
Fluttering and dancing in the breeze."

William Wordsworth (1770–1850)

6

Decimetre–Resolution Imaging of a Buried Mass Movement Deposit: Windermere, UK

6.1 Introduction

Mass movements of partly consolidated sediments are common features in lacustrine, fjord, and marine environments, playing an important role in the redistribution of sediments from shallow to deep water (Hampton et al., 1996). Whilst initial studies were generally confined to the mapping of preserved events uplifted onshore (e.g., Farrell, 1984; Martinsen and Bakken, 1990), in recent years there has been a proliferation of studies utilising a combination of core logging and geophysical techniques. Due to their extremely high hazard risk, most of this work has concentrated on large– to medium–scale structures originating on active (e.g., Tappin et al., 2007) and passive

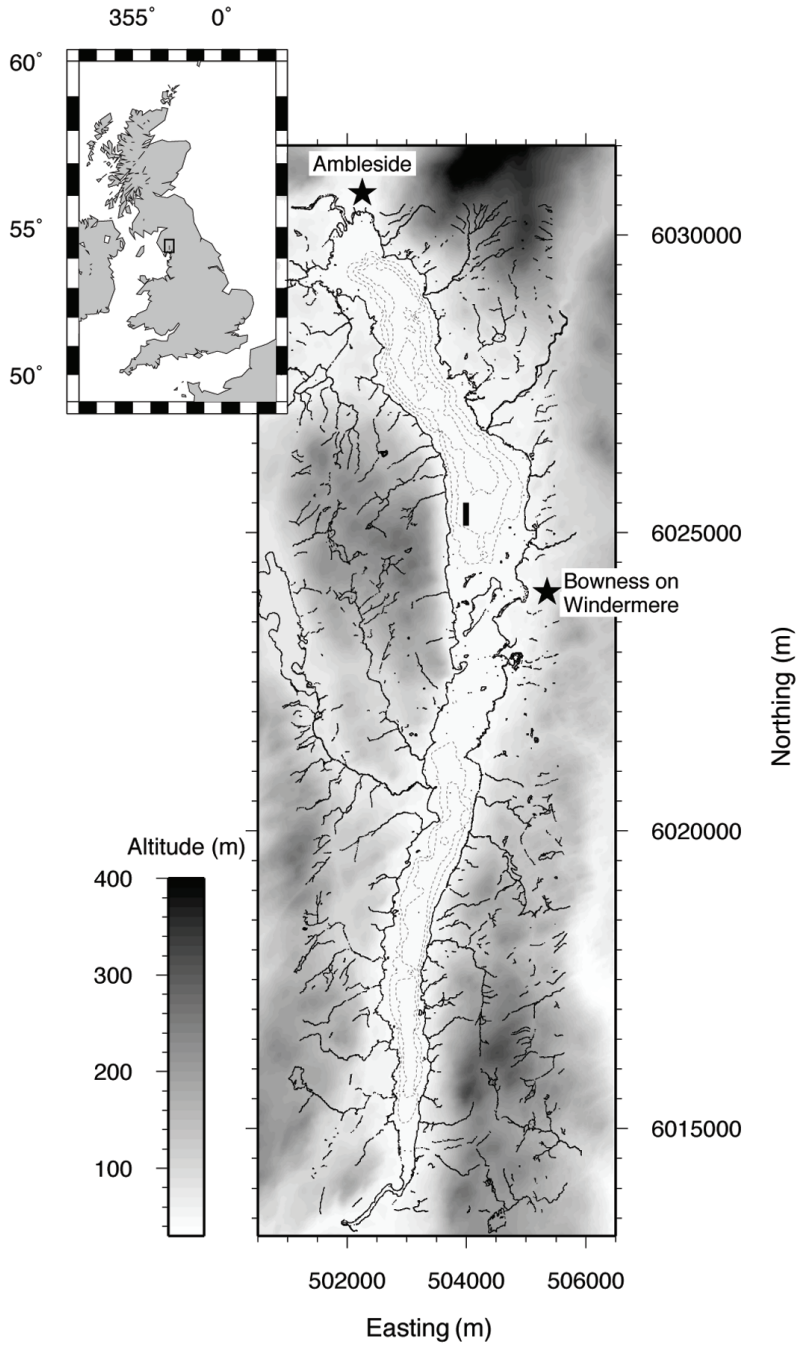

Figure 6.1: Location map showing: surrounding topography as shaded grayscale; outline of lake and surrounding waterways as black lines; lake bathymetry contours at 15, 30, and 45 m as dashed grey lines; and 2 nearby towns. Black box in the northern basin delimits location of 3D Chirp survey.

(e.g., Micallef, 2007) continental margins, and as major turbidite flows channelled down submarine canyons (e.g., Arzola et al., 2007). While several large submarine landslides have been imaged offshore using traditional 3D seismic methods (e.g., Frey-Martinez et al., 2005; Gee et al., 2006; Bull et al., 2009), studies of small– to medium–scale structures in fjord or lacustrine settings are limited to interpretation from irregularly distributed cores and/or a sparse (50 – 100 m line spacing) grid of 2D seismic lines (e.g., Schnellmann et al., 2002; Guyard et al., 2007).

Such surveys have permitted the correlation between contemporaneous mass movement events and paleoseismic records or anthropogenic influences (e.g., Schnellmann et al., 2002; Monecke et al., 2006; Schnellmann et al., 2006), but only limited interpretation of slide morphology (Schnellmann et al., 2005). In the offshore environment, 3D seismic data sets have bridged the gap between localised core stratigraphy and regional 2D seismic lines, allowing mass movement deposits to be structurally mapped in great detail (e.g., Frey-Martinez et al., 2005). From this, a well developed set of indicators for flow direction and deposition process has been developed (Bull et al., 2009). The lack of similar 3D data sets in fjord and lacustrine environments makes it unclear whether the same methods can be used in there environments or at smaller–scales.

Here we present the results of a decimetre resolution 3D seismic survey over the proximal/headwall domain of a mass movement event in the North Basin of Windermere. A high resolution seismic stratigraphic sequence is interpreted and correlated with coincident Multi–Channel Seismic (MCS) and core stratigraphy, providing sediment properties and dates for the stratigraphic facies. Within this sequence, three distinct mass movement sub–units are identified and their distributions mapped together with their associated deformation of the pre–existing sediment infill. This stratigraphic sequence allows a depositional history for the area to be outlined, illustrating the impact of regional glaciation on sedimentary regimes within the lake.

6.2 Background and Methodology

Windermere, the largest lake in the English Lake District, stretches c. 17 km in a curve running from north–north–west to south–south–west, and narrows from c. 1.5 km wide in the north to < 0.5 km at the southern tip (Figure 6.1). Forming the south–eastern spoke of a radial drainage pattern over–deepened by successive glaciations, Windermere is a classic fjord–type lake with steep valley margins and sharp lower breaks of slope. Situated c. 35 m above sea level, Windermere is dammed at the southern end by a bedrock sill 21.0 m above present lake level (Wilson, 1987), which forces the lake to drain westwards down the narrow (c. 250 m wide) and shallow (< 2.0 m below present lake level) Leven valley.

6.2.1 Regional Background

At the Last Glacial Maximum (LGM) of the British and Irish ice sheet (BIIS) (c. 30 – 25 ka BP; Bradwell et al. (2008)), snow–blown, wet–based glaciers < 500 m thick extended throughout the English Lake District (Sissons, 1979). Deglaciation of the BIIS (contemporaneous with MIS 2 Marine Isotopic Stage; Bradwell et al. (2008)) was complete, leaving a heavily eroded landscape of glacially over–deepened valleys and lakes cross–cut by a series of well preserved retreat structures and infilling finer sediments from the local Windermere Interstadial (WI). During the Younger Dryas (YD) (sometimes called the Loch Lomond Readvance in the UK; e.g., Sissons (1979)), glaciation in the English Lake District was not as extensive as in Scotland or Northern Europe, permanently maintaining only plateau icefields bordered by small valley and cirque glaciers around Sca Fell (McDougall, 2001), which did not extend as far south or east as Windermere, thereby leaving the LGM and post–LGM sedimentary stratigraphy preserved.

Over 150 km of high–resolution multichannel seismic (MCS) data, acquired using a boomer source, provide a coarse grid (50 – 200 m

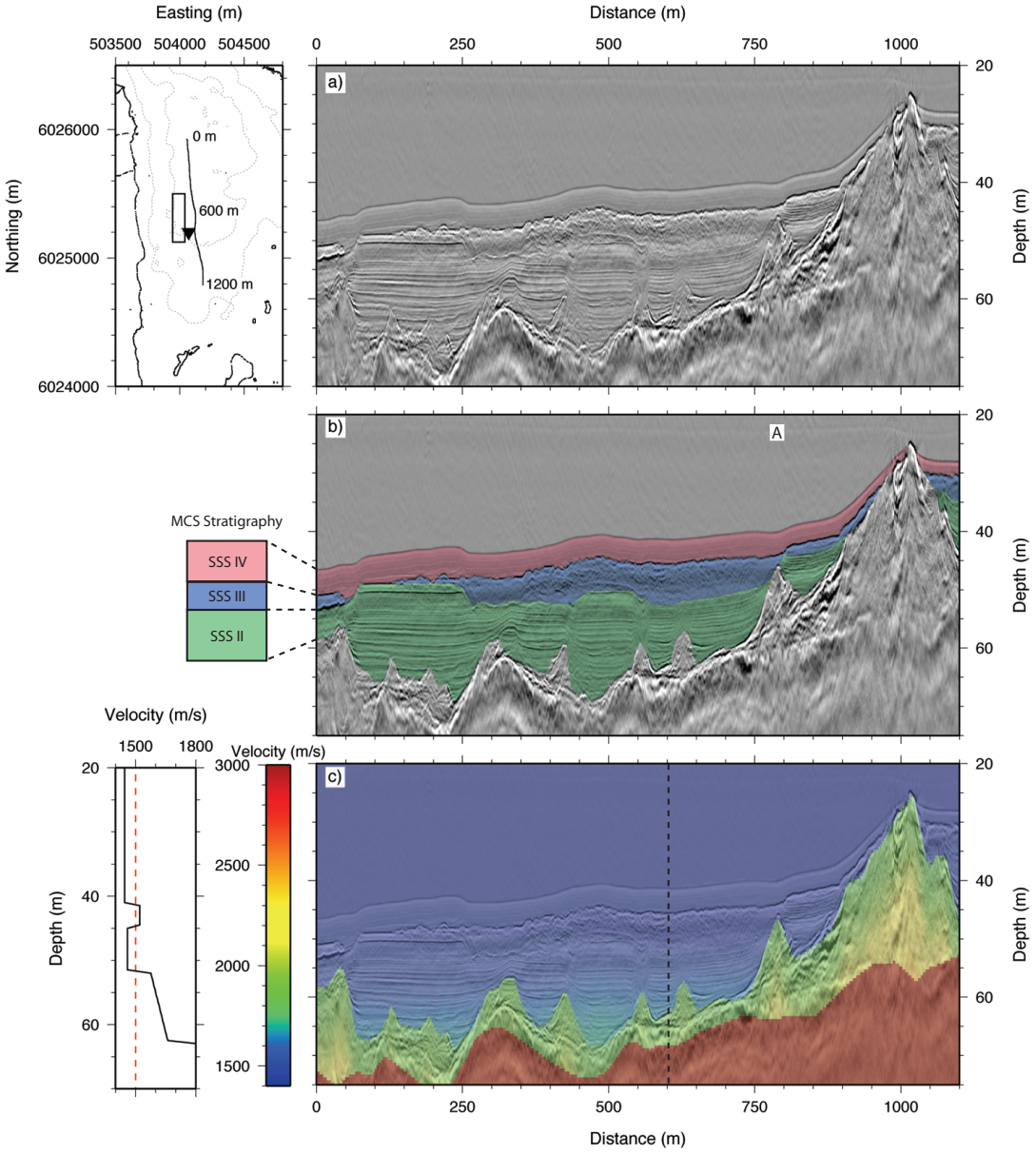

Figure 6.2: Image showing 2D Kirchhoff pre–stack depth migrated multi–channel boomer line orientated north–south, running c. 100 m east of the 3D seismic volume. Section illustrates overall structure of the basin. Panel b) overlays the interpreted seismic stratigraphic sequence, and c) the interval velocity model obtained using CRP gather velocity analysis (Pinson, 2009). The small push moraine labelled 'A', is the same east–west orientated till high observed in the 3D seismic volume.

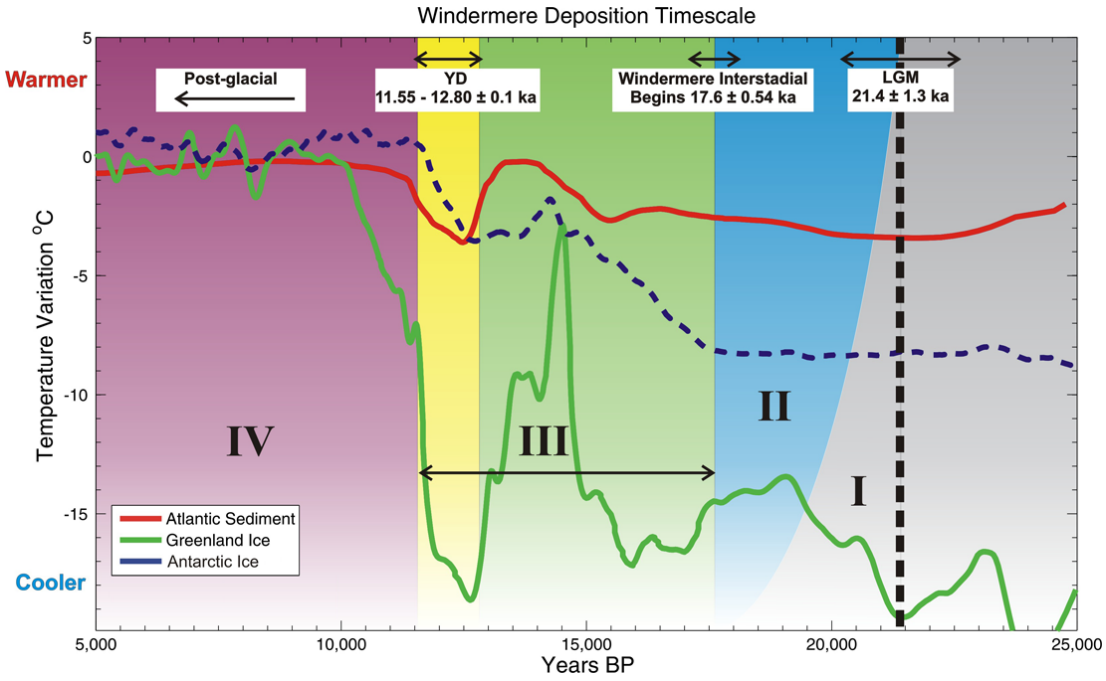

Figure 6.3: Diagram relating global and regional climatic variation over the last 25.0 ka with major sedimentary depositional units (I through IV) in Windermere. Data for: Atlantic sediment from Lea et al. (2003); Greenland ice from Alley (2000); and Antarctic ice Jouzel et al. (2007). Figure courtesy Pinson (2009).

spacing) of regional lines from which the LGM and post–LGM history could be reconstructed (Pinson, 2009). Correlation of these data (Figure 6.2) with the extensive record of pre–existing shallow cores (e.g., Pennington, 1943, 1975) allowed the definition of four main facies (Pinson, 2009):

SSS I: Outwash and lodgement till, which covers the ice–gouged valley floor and exhibits a distinct surface morphology of LGM retreat moraines. It is characterised by high amplitude top and bottom reflectors, along with internal reflections that are largely incoherent. In shallow water cores (concentrated around the lakeside), this unit appears as unsorted pebbles and cobbles in a clay matrix (Pennington, 1975).

SSS II: Thick (up to 50 m in the South and 30 m in the North Basins)

unit of Late Glacial infill, identified as finely varved (2.0 cm fining up to 0.3 cm; Pennington (1978)) with low organic content and a consistent remnant magnetisation (implying rapid deposition) (Mackereth, 1971). Acoustic properties permit this unit to be divided into two further subunits: SSS IIa, a deeper, older unit characterised by cyclical, horizontal internal reflections, occasionally interrupted by chaotic reflections at the base; and, in the South Basin only, an overlying, thinner unit (5.0 – 10.0 m) showing little or no coherent internal reflections, SSS IIb. The graded boundary between these sub–units is interpreted as the retreat of the LGM ice sheet into the North Basin, thereby limiting the sediment input into south basin to suspended fine clays (glacial flour) as the intervening bedrock high around Belle Isle prevented the transport of coarser fractions further south.

SSS III: Chaotic or chaotic–to–transparent seismic facies of varying thickness ($<$ 1.0 up to 10.0 m), bounded by high amplitude top and, in places, bottom reflectors. Where the base reflector is strong, the overall unit morphology is indicative of this being the erosional lower surface of a mass movement event cutting down into pre–existing strata, and pinching out further from the shore. Cores find the facies to be a transitional unit of organic silts and minerogrenic clay layers demonstrating significant folding/overturning (Smith, 1959). Pollen analysis has dated this unit as contemporaneous or pre–YD (Pennington, 1943), leading it to be interpreted as the result of deposition during the WI (from 17.6 ± 0.54 ka (^{14}C) (Coope et al., 1977; Lowe et al., 2008) to 12.8 ± 0.1 ka (^{14}C) (Lea et al., 2003)) and YD, that has then been locally reworked by slope failure, probably around or shortly following climate amelioration after the YD.

SSS IV: Thin (1.0 – 3.5 m), uniform drape of detrital Gyitta with 20–25 % (dry weight) organic content (Pennington, 1975), dated by ^{14}C and pollen analysis as post YD Holocene sediments (from 11.55 ± 0.1 ka (^{14}C) until present (Lea et al., 2003)).

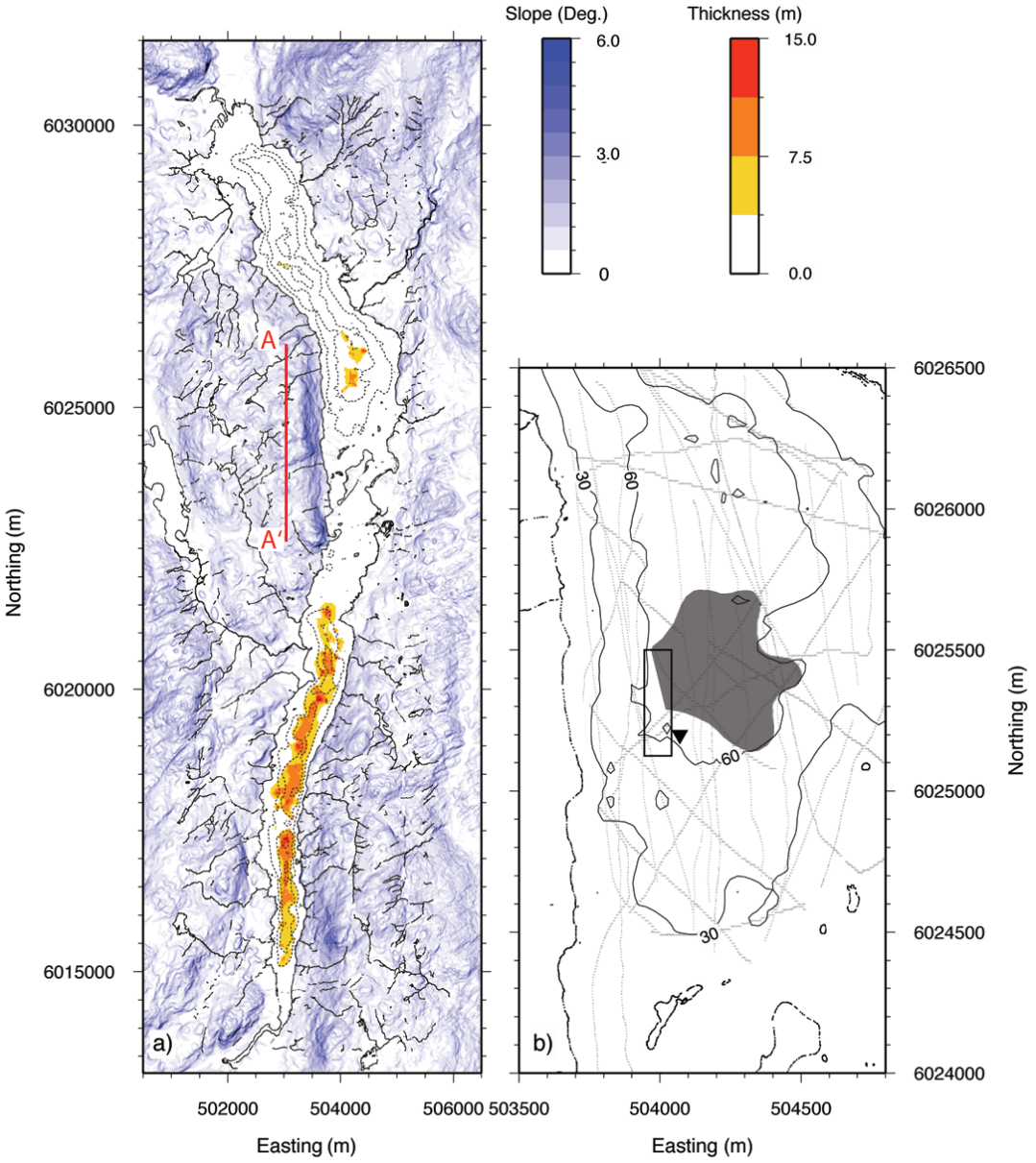

Figure 6.4: Panel a) shows distribution map of reworked YD deposit (SSS III) across the lake, overlain by depth to sediment–till boundary contoured at 30, 60, and 90 m. Surrounding topography is shaded by gradient of slope. Panel b) is a tighter plot of area in North Basin targeted by 3D Chirp survey. Dotted grey lines denote 2D MCS tracklines, inverted triangle marks location of shallow core site, and black rectangle the decimetre resolution 3D seismic volume. Shaded grey region indicates limit of target mass movement deposit mapped using regional MCS lines.

Survey Dates	Sweep	Trace Length	Sample Rate	Pulse Rate	Base Station Location
29/01/08	w32	128 ms	50 kHz	4 s^{-1}	54° 21' 09.0" N
to	(1.5 – 13.0 kHz)	(6400 samples)			2° 56' 21.49" W
01/02/08	(32.74 ms)				56.445 m

Table 6.1: Seismic survey details and acquisition parameters for 3D Chirp Windermere case study.

This sequence of facies illustrates a stratigraphy and morphology dominated by glacial processes. Glacial scouring left two over–deepened bedrock basins, subdivided into a series of sedimentary depo–centres by retreat moraines. These depo–centres are infilled by thick ($\geq$ 30 m) fining upwards deposits of outwash fines and overlain by WI deposits after climate amelioration. When glaciers re–advanced in the higher catchment during the YD, these organic–rich deposits were buried beneath a layer of minerogenic laminated clays, which shows evidence of subsequent localised mechanical reworking by mass movement events at the end of the YD. This has been followed by Holocene deposition of a thin ($<$ 3.5 m) layer of post–glacial mud, which drapes over the late glacial stratigraphy. Of the total sedimentary infill, $<$ 20 % by volume was deposited during the interstadial periods which lasted c. 16.0 kyr (Figure 6.3). Rather, it is dominated by the short time period ($<$ 5.0 kyr; Bowen et al. (2002), Coope et al. (1977), Lea et al. (2003)) of high deposition rates during retreat from the LGM and the YD.

Although, during this latter period of re–advancement, the maximum glacial extent was several kilometres north–west of Windermere, deglaciation has affected the sedimentary stratigraphy through localised reworking. Figure 6.4 shows thickness of SSS III mapped throughout the lake, surrounded by the slope of the regional topography. In the North Basin, two discrete areas thicker than 3.75 m correlate with flows associated with the steep sided western lake shore between 6,024,000 m and 6,026,500 m northing (A to A', Figure 6.4). The South Basin, however, has steep slopes on both lake shores along

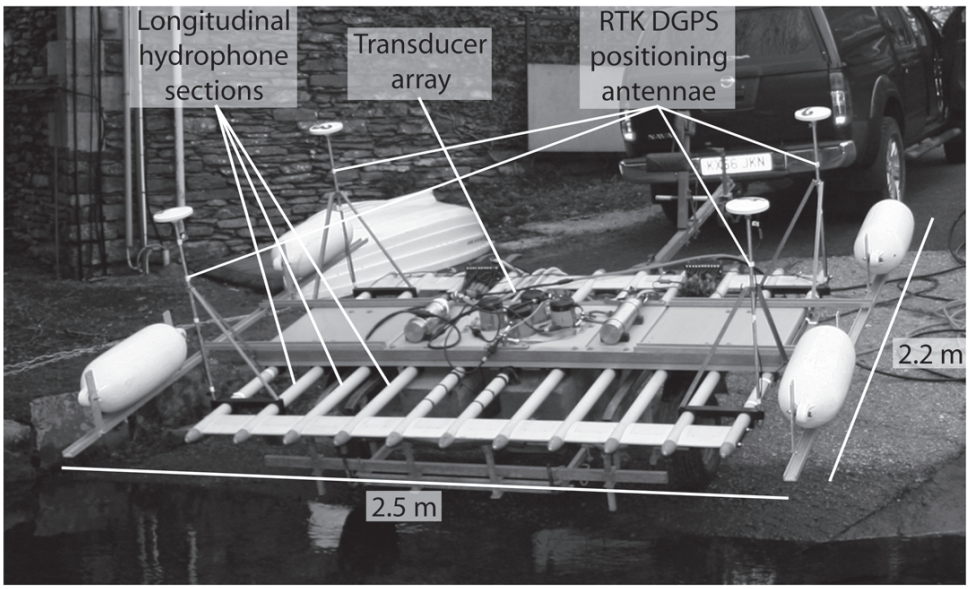

Figure 6.5: Annotated photograph of 3D Chirp sub–bottom profiler. The 60 hydrophone groups, housed in 11 longitudinal sections, are arranged in a 0.25 m by 0.25 m grid around four central transducers. RTK–GPS positioning of each source–receiver pair permits accurate trace binning onto a 12.5 cm by 12.5 cm CMP grid.

almost the full length and correspondingly contains a large number of slope failure deposits, with thicknesses > 15.0 m in some locations. Although the line spacing in the South Basin is coarse, the stratigraphy suggests that SSS III comprises several independent mass movement deposits, indicating multiple events/sources rather than a single cataclysmic event. This is taken to infer localised gravitational slope failure due to overloading and/or terrestrial derived run–off as the likely source.

6.2.2 Methodology

In January 2008 a decimetre–resolution 3D seismic volume over the more southerly flow deposit in the North Basin was acquired using the 3D Chirp sub–bottom profiler (Figure 6.4b) (Table 6.1). A 100 m by 400 m area situated 200 m from the western lake shore was

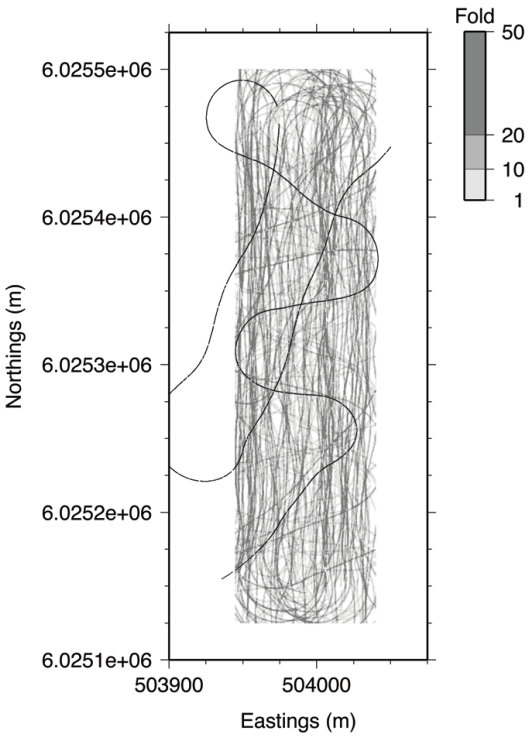

Figure 6.6: CMP fold coverage plot, darker colours being indicative of greater number of traces in the CMP bin. The superimposed black line shows a 15 minute subset of GPS locations, highlighting how the acquisition methodology involves strafing the area repeatedly at various sail angles. Gaps in the line are caused by drop outs in RTK–GPS quality.

surveyed to cover the truncation of the deposit against the till valley side. The 3D Chirp profiler is a rigid–framed, high–resolution sub–bottom profiler comprising 60 hydrophone groups arranged in a 25 x 25 cm grid around a central group of four chirp transducers (Figure 6.5). Navigation is obtained using four RTK DGPS antennae, which provide positioning accurate to $X = \pm 0.46$ cm, $Y = \pm 0.70$ cm, and $Z = \pm 1.82$ cm (Bull et al. (2005), **Chapter 2**). The reflected waveforms are recorded at a sampling interval of 0.02 ms and horizontal resolution of 12.5 x 12.5 cm (Vardy et al., 2008).

Pulsing four times per second, more than 12 million traces were acquired over three survey days at a tow distance of 15.0 m behind a small, slow moving (3 knots) survey vessel with a single outboard motor. Acquiring lines at 1.0 m line spacing provided 83 % ground coverage within the target volume, leaving no gaps larger than 5 x 9 m (Figure 6.6), which is small enough to be recovered during migration for reflectors at these depths (30 – 60 m) (**Chapter 4**). The average fold obtained was 14 traces per bin, but this rose to > 50 where the same area of lakefloor was repeatedly covered.

The data was recorded in raw, uncorrelated format, allowing for a later, more flexible processing strategy. A correlation of these raw data with the theoretical chirp waveform demonstrated good S/N ratios (Figure 6.7). As a result, a simple processing flow concentrating on optimising the resolution through migration of the diffracted energy to the correct location was used:

i) Clean the data by removing any traces with anomalously low S/N caused by bubbles in the water column and/or flotsam caught on system. Using amplitudes extracted from a TWT window centred on the lakebed horizon, it was possible to automatically scan through the volume removing poor quality traces. In total approximately 18 % of the original data volume was removed, mostly due to scattering off bubbles injected into the water column by the outboard motor.

ii) Correlation of the raw data with a family of band limited source sweeps (**Chapter 5**), thereby compressing the reflected waveform back to the Klauder wavelet, and producing a series of band limited traces for migration using a frequency approximated pre–stack Kirchhoff migration.

iii) A 3D pre–stack frequency approximated Kirchhoff time migration (see, **Chapter 5**) was used to move energy back to the correct locations using a constant velocity of 1500 ms^{-1} (average velocity for sedimentary fill estimated by CMP gather velocity analysis of MCS data; see, Figure 6.2). The S/N ratio was improved through the constructive summation of coherent reflectors, and the horizontal resolution was optimised by collapsing the Fresnel zone. Use of a Kirchhoff algorithm resampled the irregularly positioned pre–stack data onto a regular 0.25×0.25 m grid (**Chapter 4**). This larger grid spacing than the theoretical minimum was chosen empirically based on the low S/N of deeper structures due to signal attenuation within the sediment overburden.

Traditional processing of chirp sub–bottom profiler data involves applying an envelope function as the last processing stage. Such a pro-

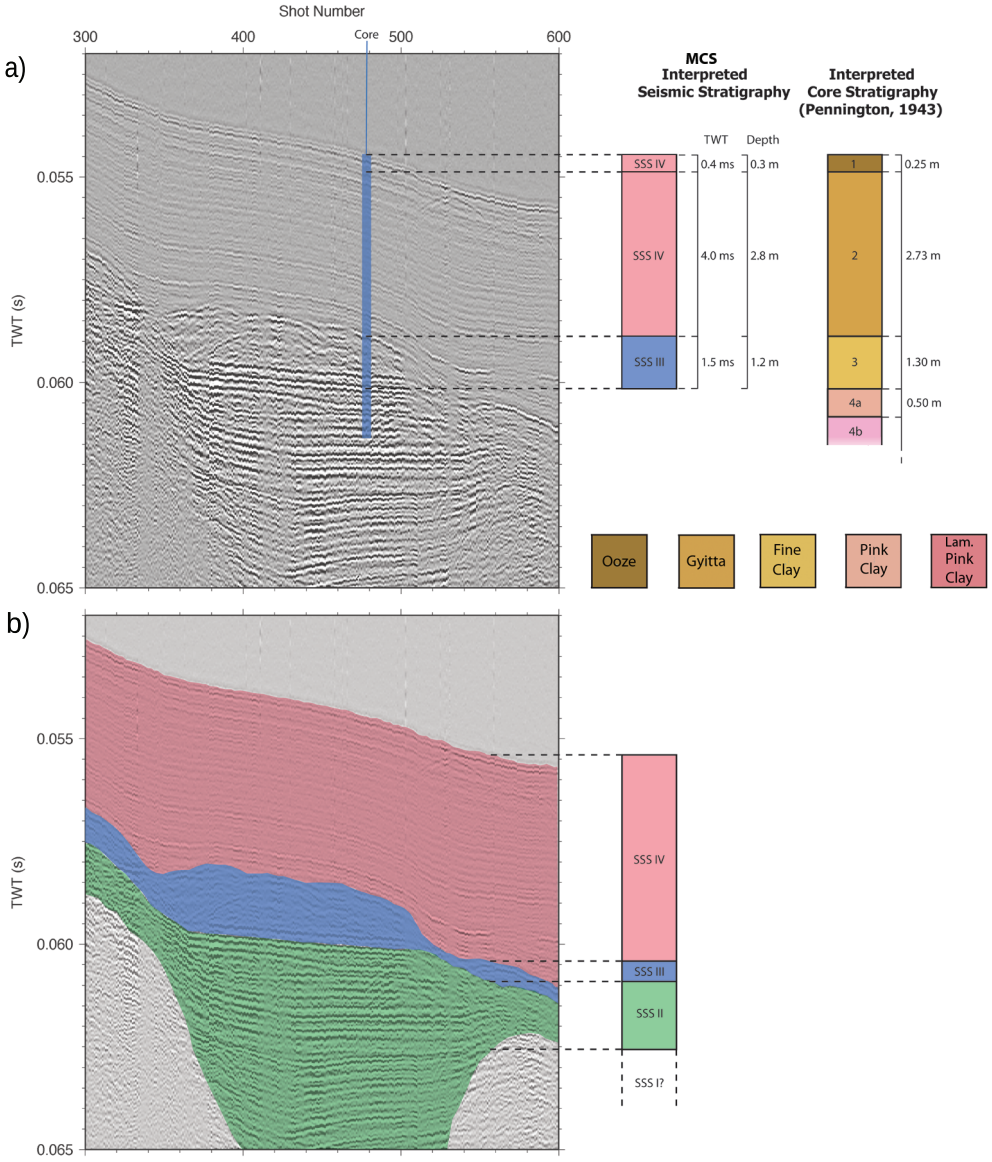

Figure 6.7: Panel a) compares a correlated section of data acquired using a single channel against the co–incident core stratigraphy. Depth conversion of reflectors using a constant velocity of 1500 ms^{-1} (Figure 6.2) demonstrates an extremely high level of correlation with the core derived stratigraphic facies. Panel b) illustrates how the same stratigraphy as defined using the regional MCS lines is observed in the high–resolution Chirp data. The positions of till highs A and B are indicated.

cess improves S/N, especially for weaker horizons, but at the expense of all polarity and phase information, as well as significant vertical/temporal smearing. Although this was implemented on a stacked volume for mapping the poorly imaged sediment/till interface, for the vast majority of interpretation this was not used as S/N was already high.

6.3 Results

6.3.1 Stratigraphic Context

The reduction in S/N with depth and large dip angles (15 – 20° in regional morphology) compared to the source directivity (**Chapter 2**), means imaging of the sediment/till boundary is incoherent. This is compounded by the coarseness of the underlying till material relative to the source wavelength, causing heavy scattering of the downgoing wavefield. However, the same gross stratigraphic framework interpreted from regional 2D lines can be identified within the decimetre resolution 3D seismic volume (Figure 6.8).

The sediment/till interface (top of SSS I and bottom of SSS II) is inferred by changes in the acoustic character and reflector termination, mapped using a combination of stacked and migrated volumes. Overlaying this, the cyclical internal reflectors of the Late Glacial SSS II can be identified, extending beyond the bottom of the migrated volume (60.0 m depth below present lake level) at the western and northern extents of the area, attaining maximum thicknesses of > 13.0 m. The base of this unit shows a general southward and westward shallowing trend, along with a number of localised highs. The east–west oriented push moraine at c. 6,025,230 m northing observed in the MCS data (labelled A; Figures 6.2 and 6.9) defines the limit of a smaller (c. 80 m wide) depo–centre in the southern third of the volume. While, a further till high (B; Figure 6.9), rising to c. 47.5 m below present lake level, c. 100 m north (c. 6,025,340 m northing) further divides the rest of the survey area into two depo–centres (Figure

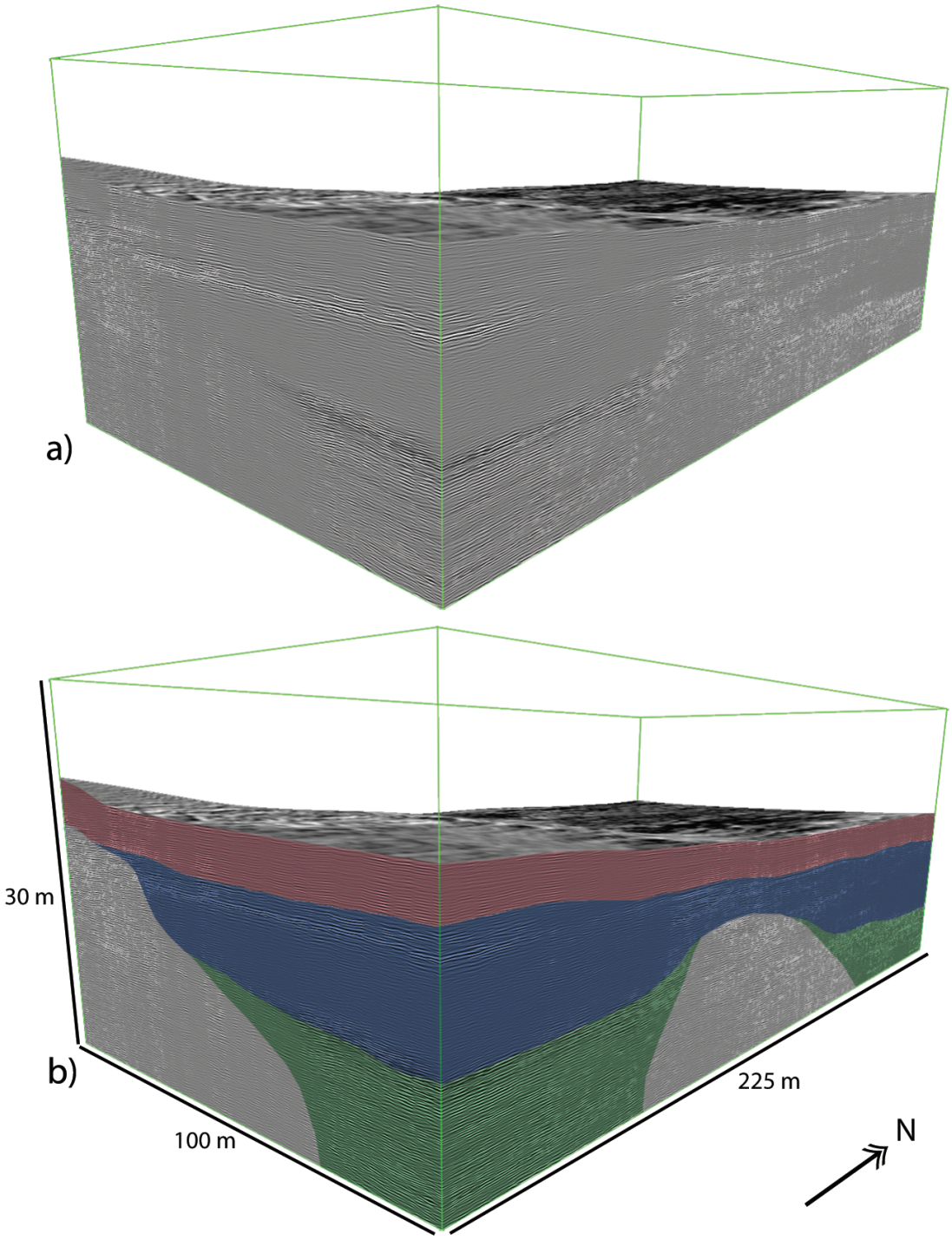

Figure 6.8: Rendered cut–away voxel volume of decimetre–resolution 3D seismic volume. Panels a) and b) show uninterpreted and interpreted versions, respectively. Colours used are the same as Figure 6.7: green being SSS II; blue SSS III and red SSS IV.

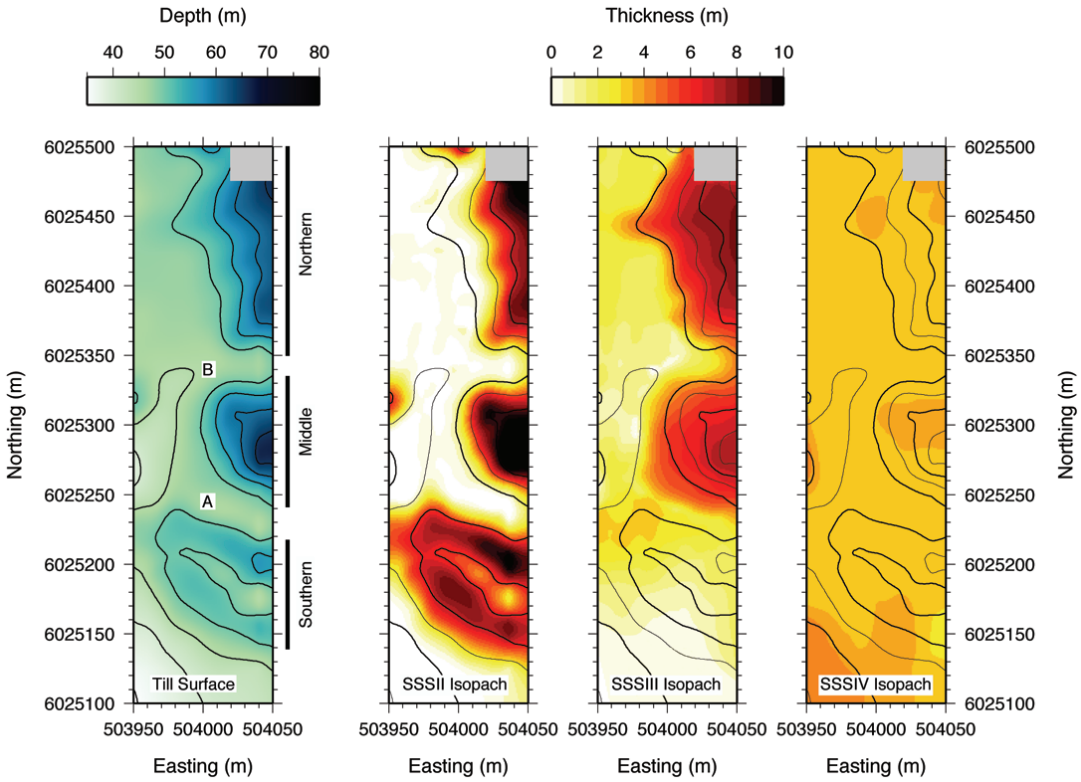

Figure 6.9: Figure showing till surface morphology together with isopachs for main seismic facies (SSS II, III, and IV, respectively) overlain by 5.0 m contours of till morphology. Constant velocity of 1500 ms^{-1} was used for depth conversion.

6.9). This till high is not observed further out in the basin, suggesting that east of the study area these two depo–centres merge into the main North Basin depo–centre.

This divides the study area into three geographically separate depo–centres (hitherto referred to as southern, middle, and northern; Figure 6.9), each of which is infilled by SSS II with no evidence for extensive Late Glacial deposition on top of the till highs. All three SSS II deposits are overlain by an eastward and north–eastward thickening (up to c. 8.0 m) unit consistent with the regionally identified YD slope failure deposit, SSS III. Over the northern two depo–centres, the facies is thickest (c. 8.0 m in the north and c. 7.0 m in the middle), and demonstrates the chaotic–to–transparent seismic facies

with high amplitude base reflections, characteristic of sub–aqueous mass movement deposition (Mulder and Cochonat, 1996; Schnellmann et al., 2005). The unit thins rapidly to the south and west at dip angles beyond the imaging limits of the 3D Chirp sub–bottom profiler (c. 16° inferred using package termination) (**Chapter 2**). It also pinches out completely to the south, with maximum southward extent of c. 6,025,186 m northing. While the unit thickness is controlled by underlying till morphology, the upper boundary of the facies shows little structure; deepening from 39.5 m to 47.0 m at a shallow angle (c. 1.5°) to the north and north–east.

Covering the whole volume is a thin (c. 3.5 m) drape consistent with the Holocene deposited SSS IV. The top of this facies forms the lakebed, which dips at a consistently shallow angle of c. 1.5° to the north and north–east, deepening from c. 36.0 m to c. 43.5 m. Across the entire survey area the thickness of this package is highly uniform, varying less that 0.2 m, and demonstrates a consistent sequence of seven sub–parallel internal reflectors. These reflectors remain coherent throughout the volume, only varying where fold coverage leads to discontinuous reflector reconstruction during migration.

6.3.2 SSS III

The primary target of the volume was the imaging of the mass movement deposits identified as being contemporaneous with the YD; SSS III (Pinson, 2009). The higher vertical resolution and 3D structural interpretation afforded by the 3D Chirp sub–bottom profiler allows several distinct sub–units to be identified within this facies (Plate 1 and Figure 6.10). Remaining consistent to the existing stratigraphic sequence definitions, these are defined below and summarised in Table 6.2.

SSS IIIa: A small (c. 1500 m^3), thin (< 1.0 m) deposit only observed in the southern depo–centre and south–western slope of the middle depo–centre. Has very high amplitude, incoherent top and

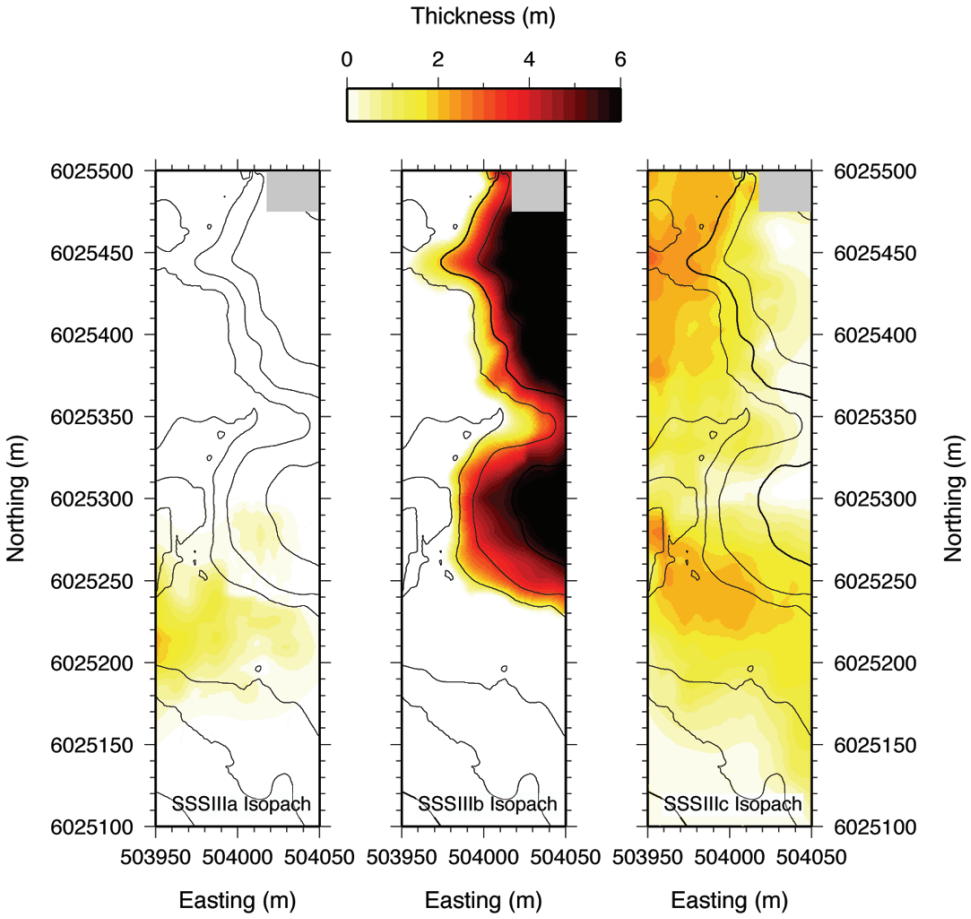

Figure 6.10: Figure showing isopach maps for 3 slide facies, SSS IIIa through IIIc, overlain by SSS III facies base morphology contoured at 2.0 m depth intervals. Constant velocity of 1500 ms^{-1} was used for depth conversion.

internal reflectors. Where it overlies SSSII in the southern depo–centre, it has a high amplitude base reflector that is interpreted as being an erosional interface. In the middle depo–centre it sits directly on the till surface and demonstrates no clear basal reflector.

SSS IIIb: A large volume, chaotic–to–transparent seismic facies that overlays the northern and middle depo–centres. Where the unit is not incised by overlying slide deposits, the upper reflector is weak and chaotic, while the base reflector is high amplitude but irregular. It is split by the till high B at c. 6,025,340 m northing, creat-

Facies	Volume in Study Area (m^3)	Estimated Total Volume (m^3)	Internal Seismic Structure	Deposition Regime
IIIc	43,000	60,000	Chaotic	Debris Flow
IIIb	54,000	500,000	Transparent	Mass Flow
IIIa	1,500	-	Chaotic	Debris Flow

Table 6.2: Overview of properties for slide deposits SSS IIIa through IIIc. Basic physical properties are provided, along with details of internal seismic structure, and interpreted deposition regime.

ing two thicker deposits of c. 8.0 m and c. 6.5 m (northern and middle depo–centres, respectively), joined by a thin drape (up to 2.5 m). The facies thins rapidly to the south and west, pinching out against the (inferred) sediment/till interface at dip angles of c. 16°. The total volume of this sub–unit is c. 54,000 m^3, thickening to the north and north–east, extending beyond the limits of the survey area.

SSS IIIc: A chaotic seismic facies (c. 43,000 m^3) with similar appearance to SSS IIIa, bounded by a high amplitude base reflector, and a discontinuous, low amplitude upper. Similar to SSS IIIb, the unit is concentrated in the middle and northern depo–centres, with maximum thicknesses of c. 3.1 m and c. 2.4 m (north and middle, respectively), but also extends as a thin (< 1.5 m) layer further south and west. Covering c. 75 % of the survey area, this facies pinches out to the south at c. 6,025,186 m northing.

6.4 Discussion

The underlying glacial till surface comprises a complex morphology of retreat structures that divide the study area into three distinct depo–centres (Figure 6.9). Despite damping of this morphology by infilling glacial fines (SSS II), this underlying structure exerts a strong controlling influence on the distribution of the subsequent mass movement units, SSS IIIa through IIIc (Figure 6.10).

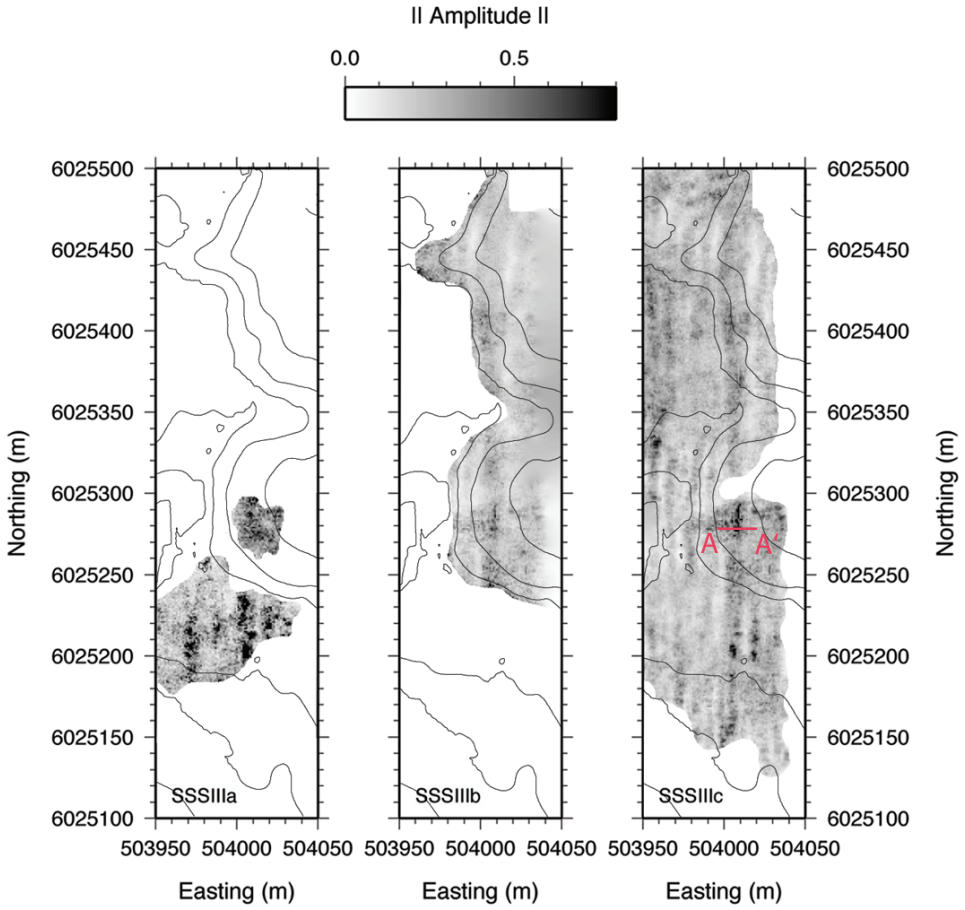

Figure 6.11: Figure showing RMS amplitude extracted between upper and lower reflectors for three slide facies, SSS IIIa through IIIc, overlain by SSS III facies base morphology contoured at 2.0 m depth intervals. The mid–amplitude, north–south streaking is a fold coverage artefact, but high amplitude anomalies in SSS IIIa and IIIc are real. Profile A to A' is showing in Figure 6.14.

6.4.1 SSS IIIa

The package is of limited extent, with only the distal part of the flow imaged in the 3D seismic area (Figure 6.10). This is observed to be two distinct deposits (in the southern and middle depo–centres; Figure 6.10) that thin rapidly north–eastward. Although not directly connected, their geographic distribution suggest they may be part of the same flow deposit, which infers a north-eastward dominant flow

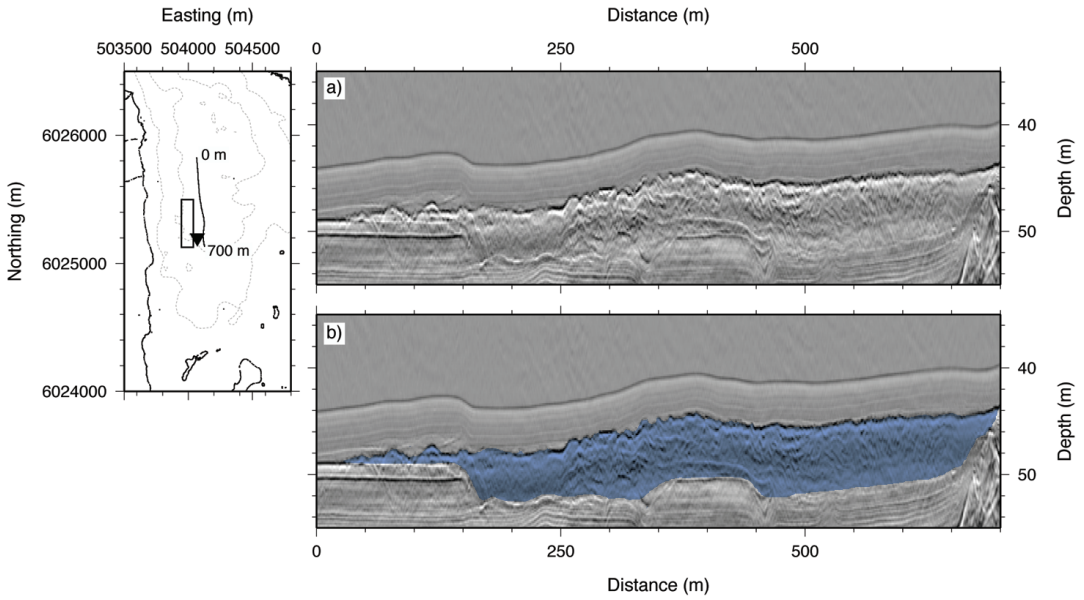

Figure 6.12: Section of pre–stack Kirchhoff depth migrated MCS line showing SSS IIIb facies (highlighted blue in panel b)).

direction (agreeing with the package thinning).

Internal RMS amplitudes extracted from the package (Figure 6.11) show a high degree of variability, with several distinct high amplitude anomalies. These correspond to localised, continuous reflectors c. 0.5 m above the package base. Similar structures are found in SSS IIIc (Figure 6.14), which appear very similar (although on a completely different scale) to the deformed translated blocks observed in the Tampen slide (Bull et al., 2009); coherent blocks of material, transported downslope with the main debris flow or slide body (Frey-Martinez et al., 2005; Gee et al., 2006). Combined with the low incision of pre–existing strata, this suggests SSS IIIa was deposited as part of a debris flow.

6.4.2 SSS IIIb

SSS IIIb has been cored in a more distal setting (Pennington, 1943), identified as being minerogenic clays deposited during the YD. As a re-

sult, these facies are interpreted as being formed by the remobilisation of YD material, probably during or shortly after climate amelioration, triggered either by gravitational failure of unstable slope material due to a change in sedimentation regime or overloading by increased land derived run–off.

SSS IIIb would require the failure of a large amount of material to form the observed stratigraphic package. Within the survey area it is a thick deposit (up to c. 8.0 m) and has a volume of c. 54,000 m^3. In addition, the same facies can be tracked a large distance into the North Basin using the regional MCS lines (Figure 6.4), covering an estimated area of c. 130,300 m^2 with a total volume of c. 500,000 m^3. Throughout 3D survey area it demonstrates a consistent flow fabric with no change in the internal seismic structure (Figure 6.11), suggesting a single cataclysmic deposition event rather than multiple smaller flows. Using the broad bandwidth of the Chirp source sweep to estimate a seismic Quality Factor (Q) (Pinson et al., 2008) supports this assertion, finding all of the material to be a homogenous and extremely fine grained, clay based sediment ($Q = 300 \pm 38$; equivalent to grain size of c. 8 Phi) throughout the unit, even in the proximal region covered by the 3D seismic volume.

With the high amplitude but irregular base reflector and rough top, this unit is thought to represent a mass flow deposit (Mulder and Cochonat, 1996; Schnellmann et al., 2005); indicating a high level of remoulding and no preservation of the pre–existing internal structure. The depth of erosion (c. 4.0 m) and distinct lateral package termination observed further into the basin (Figure 6.2) suggests a higher density, more laminar flow regime, rather than a turbidity current (Mulder and Cochonat, 1996).

The deposition of this unit involves the remobilisation of a large volume of homogeneous, fine grained sediment. A possible model for the formation of SSS IIIb might therefore be the gravitational slope failure of a fine outwash drape deposited throughout the lake during glacial retreat at the end of YD. In the northern part of the North Basin, where SSS III shows no evidence of mechanical reworking, package

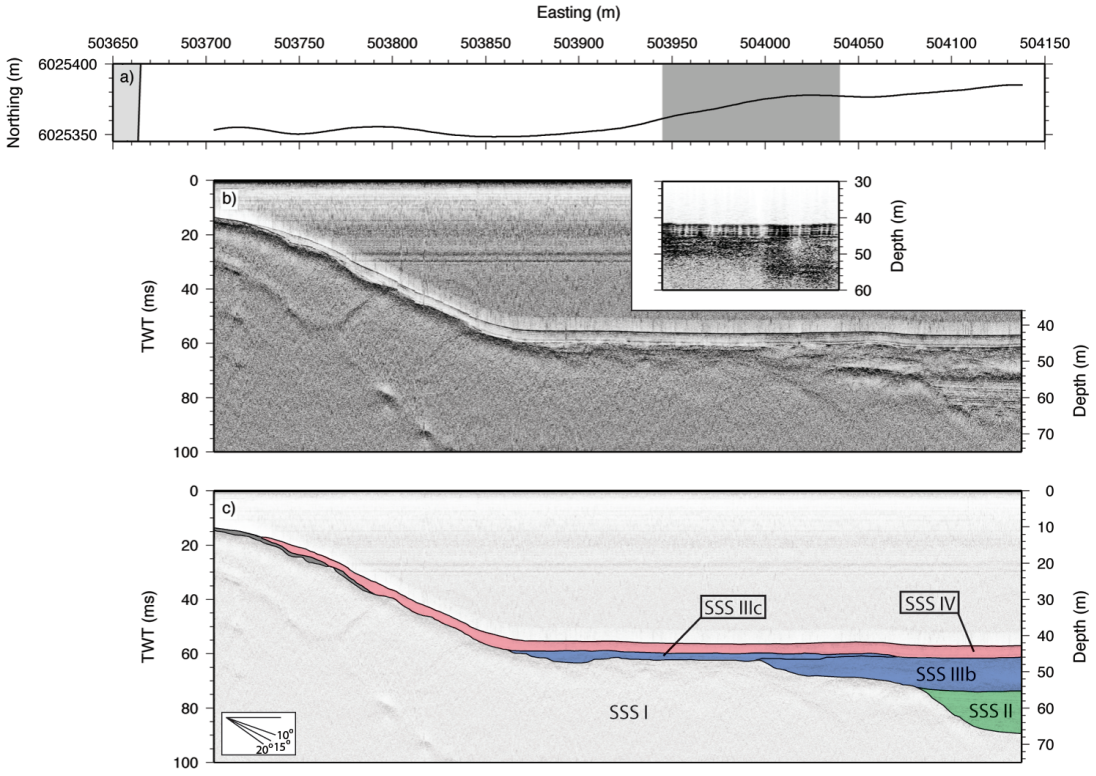

Figure 6.13: Single channel seismic line running perpendicular from western shoreline through 3D survey area, panel a). Panel b) shows section with instantaneous amplitude applied (for easier interpretation at this scale), together with coincident line extracted from migrated 3D volume. Panel c) shows interpretation.

thicknesses of c. 1.5 m are taken to be representative of this drape thickness (in keeping with outwash deposits observed in modern analogues; e.g., c. 0.3 m yr^{-1} 10.0 km from glacier (Gilbert and Crookshanks, 2008)). Given the rapid climate amelioration at the end of the YD (< 100 years; Rochon et al. (1998)), this would have been highly unconsolidated, and unstable on the steep (c. 16°; Figure 6.13) lake slopes. Figure 6.13 shows a 440 m long tie line running perpendicular to the western shore, through the 3D survey area. Pre–Holocene deposits above the LGM till (SSS I) have been completely evacuated from the lake marginal slope, with only a small amount remaining very high up near the shore (shaded dark grey; Figure 6.13), which

is consistent with gravitational slope failure as a source. This slope region (c. 200,000 m^2 bounded by moraine A to the south and further till highs to the north) can account for c. 300,000 m^3 of material, which, when combined with material remobilised from the present flow location, is consistent with the 500,000 m^3 volume for SSS IIIb. This source also agrees with the overall deposit distribution, which suggests a north–eastward transport direction, bounded at its eastern limit by further till highs (Figures 6.4b and 6.10).

6.4.3 SSS IIIc

Pennington (1943), who samples SSS IIIc in the core due east of the survey area (Figure 6.7), describes it as a heavily deformed transition deposit. The heavy deformation supports classification of the unit as a debris flow based on seismic characteristics of a high amplitude, shear surface base reflector and discontinuous, chaotic internal structure (Mulder and Cochonat, 1996). The package is typically lens shaped, thinning gradually northward and eastward with very little relief on the top and bottom reflectors ($< 2°$), although there are localised discontinuities in the top. Total volume of the facies within the 3D survey area (c. 43,000 m^3) is similar to SSS IIIa because, although thinner, it covers a greater area. However, this facies does not appear as far out into the basin; extending only a short distance to the east where it is sampled in the core (Pennington, 1943) and MCS line (Pinson, 2009), before pinching out. This suggests a much smaller total volume of c. 60,000 m^3 for the deposit.

Within this unit a number of high amplitude, discrete reflectors (Figure 6.11) show similar properties to those observed in SSS IIIa. Figure 6.14 shows a cross–line section together with a timeslice from the migrated volume through one of these reflectors. Although the timeslice is contaminated by uncancelled diffraction noise (from the sediment–till boundary) to the north–west, there is a coherent c. 3.0 m by 8.0 m polygonal high amplitude region, which shows up as a laterally coherent reflector c. 0.4 m above the facies base in the vertical section. This

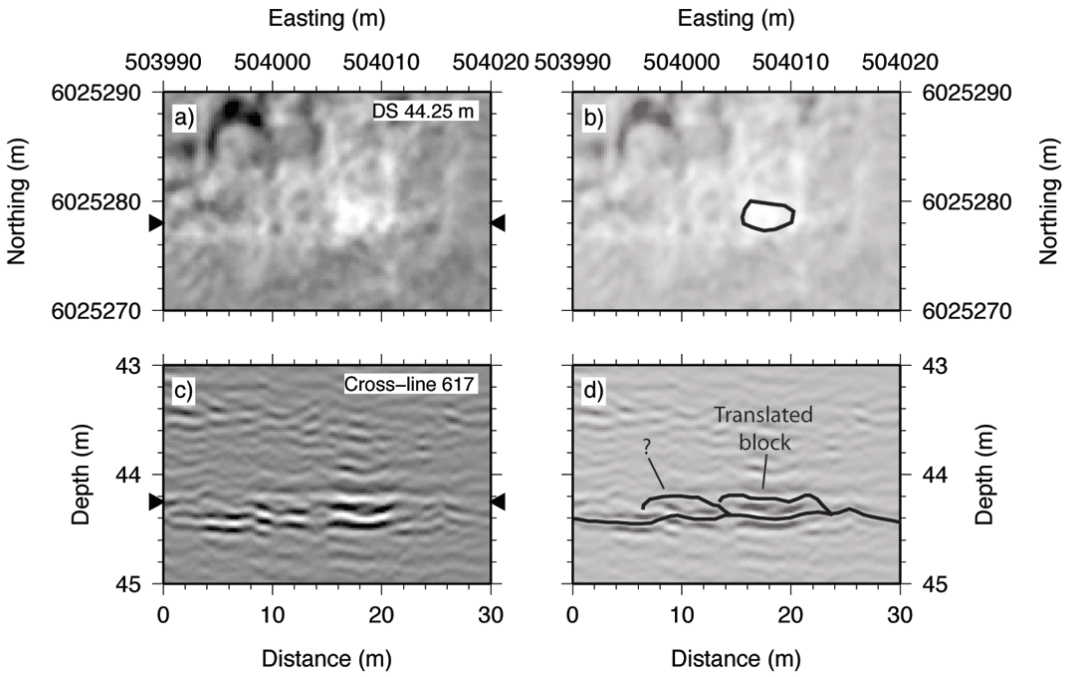

Figure 6.14: Uninterpreted, a) and c), and interpreted, b) and d), cross–line and timeslice through the 3D seismic volume, identifying at least one deformed translated block in SSS IIIc. Similar structures are also seen in SSS IIIa. Depth conversion performed using velocity of 1500 ms^{-1}.

discrete region of coherency is in complete contrast to the surrounding chaotic reflectors of the facies. The block long–axis orientation can be used to infer flow direction (Bull et al., 2009); implying an eastward or westward direction of motion (Figure 6.14). The agrees with the general eastward thinning of the unit (Figure 6.10) and downslope direction, an suggesting eastward flow direction.

6.4.4 Holocene Drape

Draped over these complex facies are the organic–rich Holocene deposits. These demonstrate a constant thickness (c. 3.5 m), and a coherent set of internal reflectors throughout the survey area. The shallowest of these corresponds to the ooze/Gyitta transition at 0.25

m depth, and the deepest a Chlorite band from the Borrowdale volcanic unit 0.20 m above the facies base (Figure 6.7 and Pennington (1943)). Pennington (1943, 1991) mention other Chlorite bands and possible flood deposits visible in the Holocene layer, but no depth information is explicitly given meaning the other internal reflectors cannot be correlated with stratigraphic events. The thin and constant thickness of this facies supports recent estimates of the sedimentary rate since climate amelioration after the YD using core data (c. 0.36 mm yr^{-1}; (Chiverrell, 2006)), suggesting an average deposition of c. 0.38 mm yr^{-1}.

6.5 Summary

By acquiring a decimetre–resolution 3D seismic volume through the headwall domain of a buried mass wasting deposit, I have been able to map the complicated interaction between a number of mass movement units with the pre–existing and overlying sedimentary facies. This has enabled the reconstruction of a depositional history for the stratigraphic units identified in the seismic volume (Figure 6.15):

1. During retreat from LGM, the till material (SSS I) deposited at or near ice contact was overlain by a thick (> 13.0 m) deposit of glacial outwash fines (SSS II) that form a seismic facies with cyclical, high amplitude internal reflectors. As the site became more proximal this deposit fines upwards, showing gradually increased organic content during the transition into the Windermere interstadial, when deposition rates are likely to have been low.
2. A thin chaotic unit was formed either during this climate amelioration or the subsequent flora retreat at the beginning of the YD (c. 1500 m^3; SSS IIIa).
3. The fast transition from stadial to interstadial conditions at the end of the YD resulted in the rapid deposition of fine, unconsolidated glacial outwash. Gravitation instability or overloading by

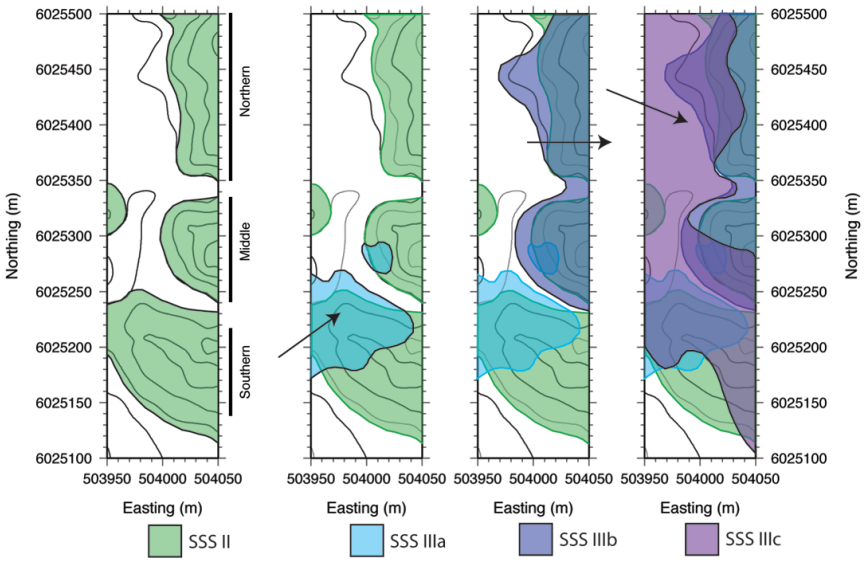

Figure 6.15: Figure illustrating the local depositional history. Panel a) shows sedimentary structure after deglaciation from LGM with contours of till surface, overlain by gravitationally deposited fines. Sometime between this climate amelioration and glacial readvance during the LLR/YD, SSS IIIa was deposited, panel b). During climate amelioration from the LLR/YD the large volume of fine outwash was reworked in a series of mass movements events, panel c). Firstly producing the mass flow deposit SSS IIIb, and then the debris flow, SSS IIIc, panel d). Subsequently, a detrital drape has been deposited throughout the Holocene, which covers this entire sedimentary sequence with a 3.5 m thick drape. Arrows indicate interpreted dominant flow direction.

terrestrial derived material caused two translational mass wasting events (SSS IIIb and IIIc) of this clay drape. The earliest (SSS IIIb) is likely a result of gravitational instability, causing the mass flow deposition of large volumes (c. 54,000 m^3 in survey area; c. 500,000 m^3 in whole deposit) of material, observed as a transparent seismic facies that covers c. 130,000 m^2. This is then overlain and incised into by a smaller (c. 43,000 m^3) debris flow deposit (SSS IIIc), characterised by a lens shaped, more chaotic seismic facies.

4. After climate amelioration, the sedimentary influx became more

organic, depositing a c. 3.5 m thick drape at an average sedimentation rate of 0.36 – 0.38 mm yr^{-1}.

6.6 Conclusions

This data set illustrates how using the frequency approximated pre–stack Kirchhoff migration algorithm (**Chapter 5**) allows the migration of a large 3D seismic data set acquired using the 3D Chirp sub–bottom profiler. Migration of a 40.0 ms window of data centred around the slide facies took 84 hours to migrate on the eight core workstation used in previous chapters (**Chapters 4** and **5**). A similar migration using the full Kirchhoff migration (as implemented by ProMAX) is estimated to take c. 2 months (c. 1500 hours). Even with a very high data loss rate (18 % of original traces were removed during cleaning), it resulted in coherent volume with interpretable reflectors $>$ 35 ms below the lakebed.

Interpretation of this decimetre–resolution 3D seismic volume over one of the YD mass movement deposits has allowed the internal structure and interaction with pre–existing and overlying packages of the mass movement facies to be examined in unprecedented detail. Three distinct flow events are identified and mapped throughout the 3D survey area. Analysis of package structures and seismic attributes allows their classification as: a small (c. 1500 m^3), pre–YD debris flow; a large (c. 500,000 m^3), consistently fine–grained mass flow deposit post–YD; and a smaller (c. 60,000 m^3), post–YD debris flow containing small (c. 8.0 m by 2.0 m) deformed translated blocks. This stratigraphy indicates heavy, localised periodic reworking of the sediments at various times, notably shortly after YD climate amelioration when there appears to have been complete evacuation of unconsolidated sediments from the lake marginal slopes.

"In theory, theory and practice are the same. In practice, they are not."

Albert Einstein (1879–1955)

7 Conclusions

While previous authors (e.g., Bull et al., 2005; Gutowski et al., 2008) have demonstrated the possibility of acquiring 3D seismic volumes in shallow water, major questions still remained regarding the acquisition and processing methods. In particular, there was a poor understanding regarding both: the effect of irregularities in the acquisition coverage on the final data volume; and the total processing time–scales were very long ($\geq 50\times$ acquisition time; i.e., c. 1 year).

In this thesis I have approached the acquisition and processing of decimetre resolution 3D seismic volumes from first principles. The basic parameters of source/receiver positioning, shot–to–shot repeatability, and aliasing were discussed in **Chapter 2**, defining the limitations of the 3D Chirp sub–bottom profiler. In **Chapter 3** a combination of standard Chirp/Vibroseis and industry processing methods were used on a case study in small object detection, illustrating the effectiveness of acquiring decimetre–resolution 3D seismic volumes for engineering and homeland defence applications. **Chapters 4** and **5**

explore the imaging of 3D Chirp data volumes, developing an understanding of the effects of acquisition irregularities on imaged volume quality (**Chapter 4**), together with a more efficient approach to pre–stack 3D Kirchhoff time migration that reduces processing times to c. real–time (**Chapter 5**). These methods are then applied to a geological case–study in Windermere, UK Lake District, imaging a series of mass movement events for which deposition regimes and flow directions are derived (**Chapter 6**).

There are four principle outcomes from this work:

i) In shallow–water ($\leq$ 15.0 m) environments the 3D Chirp sub–bottom profiler permits the acquisition of a true 3D seismic volume with vertical and horizontal resolutions approaching the theoretical limits (centimetric and decimetric, respectively). This affords unparalleled imaging of buried engineering, archaeological, and homeland defence targets, successfully identifying objects down to 30 cm by 30 cm in size.

ii) It is possible to use the 3D Chirp sub–bottom profiler to image larger–scale (c. 200,000 m^2) geological targets. The mapping of such features in 3D and at such resolutions enables detailed, fundamental questions about their distribution and formation to be answered. The complex interaction between packages, along with reflector and facies internal attributes have been used to infer deposition regimes, and reconstruct the depositional history for an area.

iii) Significantly sized gaps in coverage (up to 2.0 m by 2.0 m for a reflector at 10.0 m depth) can be reconstructed during migration if the gaps are symmetric. As the gaps become increasingly asymmetric, the width over which a reflector can be successfully reconstructed rapidly decreases. As such, future acquisition methods should involve strafing the survey area using two perpendicularly oriented sets of track–lines to minimise gap sizes and asymmetries.

iv) Frequency decomposition of traces can be accomplished by correlation with a series of bandwidth limited Chirp sweeps. Pre–stack

3D Kirchhoff time migration of the resulting traces using coefficients determined at the central frequencies produces comparable results to a full Kirchhoff time migration (implemented using ProMAX), whilst reducing the computational time for a full data volume from ≥ 1 month to c. two to three days (i.e., approximately equal to acquisition time). A real–time implementation of this algorithm will afford a significantly better assessment of volume quality during acquisition, while in post–processing it makes the migration of entire data volumes feasible on a time–scale suitable for both industrial and academic applications.

During the course of this thesis I have shown that by treating 3D Chirp data sets on a trace–by–trace basis it is possible to correct irregularities in the spatial sampling during migration, reconstructing coherent reflectors across data gaps several metres in size. This affords detailed interpretation of reflector and facies morphology on a broad range of scales (e.g., see **Chapters 3** and **6**). However, there remain several limitations in the acquisition and processing methods, most notably: the source directivity, which dramatically limits reflector imaging of geologically complicated targets (e.g., **Chapter 6**); and the approach to anti–aliasing during imaging, which does not effectively image steeply dipping reflectors (e.g., **Chapter 5**).

Future developments of the 3D Chirp sub–bottom profiler should look to address these system limitations, thereby broadening the scope of targets that can be effectively imaged. Redesigning the transducer array to produce an azimuthally isotropic source with a -3 dB level at c. 30° dip angle both along and across track would greatly enhance the system's ability to image complex geological targets, while taking a more complex approach to aliasing (such as a frequency dependent maximum aperture angle) will more effectively reconstruct steeper dipping reflectors. In addition, future survey data should be corroborated with newly acquired coincident cores to ground–truth the observed seismic structure. An important factor in proving the effectiveness of this technology beyond anecdotal academic applications.

Bibliography

R. B. Alley. The Younger Dryas cold interval as viewed from central Greenland. *Quaternary Science Reviews*, 19:213–226, 2000.

S.H.L. Arnott, J. Dix, A.I. Best, and D.J. Gregory. Imaging of buried archaeological materials: The reflection properties of archaeological wood. *Marine Geophysical Researches*, 26(2-4):135–144, 2005.

R. G. Arzola, R. B. Wynn, D. G. Masson, P. P. E. Weaver, and G. Lastras. Landslide and gravity flow features and processes in the Nazarae and Setubal Canyons, west Iberian margin. In V. Lykousis, D. Sakellariou, and J. Locat, editors, *Submarine mass movements and their consequences:3rd International Synposium*, volume 27 of *Advances in Natural and Technological Hazards*, pages 89–98. Springer, Dordrecht, Netherlands, 2007.

C. Bagaini and U. Spagnolini. 2-D continuation operators and their applications. *Geophysics*, 61(6):1846–1858, 1996.

B. Barney. POSIX Threads Programming, 1995. URL `http://standards.ieee.org/reading/ieee/interp/1003-1c-95_int/index.html`.

E. Baysal, D. D. Kosloff, and J. W. C. Sherwood. Reverse time migration. *Geophysics*, 48:1514–1524, 1983.

E. Baysal, D. D. Kosloff, and J. W. C. Sherwood. A two-way nonreflecting wave equation. *Geophysics*, 49:131–141, 1984.

E. Bedrosian. A product theorem for Hilbert Transforms. *Proc. IEEE (Coresp.)*, 51:868–869, May 1963.

J. R. Berryhill. Diffraction response for nonzero separation of source and receiver. *Geophysics*, 42(6):1158–1176, October 1977.

D. Bevc and J. Claerbout. Fast anti-aliased Kirchhoff migration and modelling. *Stanford Exploration Project*, Report 75:97–103, 1997.

B. L. Biondi. *3D Seismic Imaging*. SEG, 2006.

B. L. Biondi, S. Fomel, and N. Chemingui. Azimuthal moveout for 3-D prestack imaging. *Geophysics*, 63(2):574–588, 1998.

B.L. Biondi. Kirchhoff imaging beyond aliasing. *Geophysics*, 66(2): 654–666, 2001.

B.L. Biondi. *Concepts and Appplications in 3D Seismic Imaging*. Number 10 in SEG Distinguished Instructor Short Course. SEG, Tulsa, Oklahoma, USA, 2007.

N. Bleistein. *Mathematical methods for wave phenomena*. Academic Press Inc., 1984.

N. Bleistein. On the imaging of reflectors in the earth. *Geophysics*, 52(7):931–942, 1987.

N. Bleistein and S. H. Gray. From the Hagedoorn imaging technique to Kirchhoff migration and inversion. *Geophysical Prospecting*, 49: 629–643, 2001.

T. Bohlen, C. Muller, and B. Milkereit. Elastic Seismic-Wave Scattering from Massive Sulfide Orebodies: On the Role of Composition and Shape. In *Hardrock Seismic Exploration*, pages 70–89. Tulsa: SEG, 2003.

D. Q. Bowen, F. M. Phillips, A. M. McCabe, P. C. Knutz, and G. A. Sykes. New data for the Last Glacial Maximum in Great Britain and Ireland. *Quaternary Science Reviews*, 21:89–101, 2002.

T. Bradwell, M. S. Stoker, N. R. Golledge, C. K. Wilson, J. W. Merritt, D. Long, J. D. Everest, O. B. Hestvik, A. G. Stevenson, A. L. Hubbard, A. G. Finlayson, and H. E. Mathers. The northern sector of the last British Ice Sheet: Maximum extent and demise. *Earth Science Reviews*, 88:207–226, 2008.

R.A. Broding, J.M. Hess, and R.E. Wanous. A high-power computer-controlled marine Vibroseis system. *IEEE Transactions on Geoscience Electronics*, GE-9:90–95, 1971.

R. Buckley. Diffractionby a random phase-changing screen: A numerical experiment. *J. Atmos. Terr. Phys.*, 37:1431–1446, 1975.

J. M. Bull, R. Quinn, and J. Dix. Reflection coefficient calculation from marine high-resolution seismic reflection (Chirp) data and application to an archaeological case study. *Marine Geophysical Researches*, 20:1–11, 1998.

J. M. Bull, M. Gutowski, J. Dix, T. Henstock, P. Hogarth, T. Leighton, and P. White. Design of a 3D Chirp sub-bottom imaging system. *Marine Geophysical Researches*, 26:157–169, 2005.

S. Bull, J. Cartwright, and M. Huuse. A review of kinematic indicator from mass-transport complexes using 3D seismic data. *Mar. Petrol. Geol.*, 26:1132–1151, 2009.

J. Cabrera, W. Perkins, T. Hagen, G. Tensor, and D. W. Ratcliffe. 3-D Prestack Depth Migration: Implementation and Case History. *SEG Expanded Abstracts*, 11:948–951, 1992.

J. Cartwright and M. Huuse. 3D seismic technology: the geological 'Hubble'. *Basin Research*, 17:1–20, 2005.

N. Chemingui. *Imaging Irregularly Sampled 3D Prestack Data*. PhD thesis, Department of Geosciences, Stanford University, 2001.

R. C. Chiverrell. Past and future perspectives upon landscape instability in Cumbria, northwest England. *Regional Environmental Change*, 6:101–114, 2006.

J. Claerbout. Basic Earth Imaging. Technical report, Stanford Exploration Project, 2005. URL `http://sepwww.stanford.edu/public/docs/bei/toc_html/index.html`.

J. F. Claerbout. Coarse grid calculations of waves in inhomogeneous media with application to delineation of complicated seismic structure. *Geophysics*, 35(3):407–418, June 1970.

J. F. Claerbout. Toward a Unified Theory of Reflector Mapping. *Geophysics*, 36(3):467–481, 1971.

J. F. Claerbout. Anti aliasing. *Stanford Exploration Project*, 73(371-390), 1992.

J.F. Claerbout and S.M. Doherty. Downward Continuation of Moveout-Corrected Seismograms. *Geophysics*, 37(5):741–768, 1972.

G. R. Coope, W. Pennington, G. F. Mitchell, R. G. West, A. V. Morgan, and J. D. Peacock. Fossil Coleopteran Assemblages as Sensitive Indicators of Climatic Changes During theDevensian (Last) Cold Stage [and Discussion]. *Philosophical Transactions of the Royal Society of London. Series B, Biological Sciences*, 280:313–340, 1977.

S. Crawley. *Seismic Trace Interpolation with Non–Stationary Prediction–Error Filters*. PhD thesis, Department of Geosciences, Stanford University, 2001.

R.J. Davies, S.A. Stewart, J.A. Cartwright, M. Lappin, R. Johnston, S.I. Fraser, and A.R. Brown. 3D seismic technology: are we realising its full potential? In R.J. Davies, J.A. Cartwright, S.A. Stewart, M. Lappin, and J.R. Underhill, editors, *3D Seismic Technology: Application to the Exploration of Sedimentary Basins*, number 29 in Geological Society, London, Memoirs. The Geological Society of London, 2004.

S. M. Deregowski and F. Rocca. Geometrical optics and wave theory of constant offset sections in layered media. *Geophysical Prospecting*, 29:374–406, 1981.

J. A. Dickinson. Evaluation of two-pass three-dimensional migration. *Geophysics*, 53(1):32–49, 1988.

P. Docherty. A brief comparison of some Kirchhoff integration formulas for migration and inversion. *Geophysics*, 56(8):1164–1169, 1991.

B. Dragoset. A historical reflection on reflections. *The Leading Edge*, 24(51):S46–S70, October 2005.

B. J. Drummond, R. W. Hobbs, and B. R. Goleby. The effects of out-of-plane energy on reflections in crustal-scale 2D seismic sections. *Tectonophysics*, 388:213–224, 2004.

A. J. W. Duijndam and M. A. Schonewille. Nonuniform fast Fourier transform. *Geophysics*, 64(2):539–551, 1998.

A. J. W. Duijndam, M. A. Schonewille, and C. O. H. Hindriks. Reconstruction of band–limited signals, irregularly sampled along one spatial direction. *Geophysics*, 64(2):524–538, 1999.

B. Duquet, P. Lailly, and A. Ehinger. 3D plane wave migration of streamer data. In *71st Annual International Meeting, SEG, Expanded Abstracts*, pages 1033–1036, 2001.

H. Edwards. The North Sea Mega Mergers. In A. Dore and B. Vining, editors, *Petroleum Geology of Northwest Europe: Proceedings of the 6th Conference*, 2005.

N. Eyles and H. T. Mullins. Seismic Stratigraphy of Shuswap Lake, British Columbia, Canada. *Sediment Geology*, 109:283–303, 1997.

S. G. Farrell. A dislocated model applied to slump structures, Ainsa Basin, South Central Pyrenees. *J. Struct. Geol.*, 6:727–736, 1984.

S. Fomel and B. L. Biondi. The time and space formation of azimuthal moveout. *SEG Expanded Abstracts*, 15:1449–1453, 1996.

D. Forel and G. H. F. Gardner. A three-dimensional perspective on two-dimensional dip moveout. *Geophysics*, 53:604–610, 1988.

J. Frey-Martinez, J. Cartwright, and B. Hall. 3D seismic interpretation of slump complexes: examples from the continental margin of Israel. *Basin Research*, 17:83–108, 2005.

J. Gazdag. Wave equation migration with the phase-shift method. *Geophysics*, 43(7):1342–1351, 1978.

M. J. R. Gee, R. L. Gawthorpe, and S. J. Friedmann. Triggering and evolution of a giant landslide, offshore Angola revealed by 3D seismic stratigraphy and geomorphology. *J. Sedimentary Research*, 76:9–19, 2006.

R. Gilbert and S. Crookshanks. Sediment waves in a modern high-energy glacilacustrine environment. *Sedimentology*, 56:645–659, 2008.

S.H. Gray. Frequency-selective design of the Kirchhoff migration operator. *Geophysical Prospecting*, 40:565–572, 1992.

M. Gutowski. *Development and Application of a High–Resolution 3D Chirp Sub–Bottom Profiling System*. PhD thesis, School of Ocean and Earth Science, University of Southampon, December 2004.

M. Gutowski, J. M. Bull, J. Dix, T. Henstock, P. Hogarth, P. White, and T. Leighton. Chirp sub-bottom profiler source signature design and field testing. *Marine Geophysical Researches*, 23:481–492, 2002.

M. Gutowski, J. M. Bull, J.K. Dix, T. J. Henstock, P. Hogarth, T. Hiller, T.G. Leighton, and P.R. White. 3D high-resolution acoustic imaging of the sub-seabed. *Applied Acoustics*, 69(5):412–421, 2008.

H. Guyard, E. Chapron, G. St-Ogne, F. S. Anselmetti, F. Arnaud, O. Magand, P. Francus, and M.-A. Melieres. High-altitude varve records of abrupt environmental changes and mining activity over the last 4000 years in the Western French Alps (Lake Bramant, Grandes Rousses Massif). *Quaternary Science Reviews*, 26:2644–2660, 2007.

J. G. Hagedoorn. A process of seismic reflection interpretation. *Geophysical Prospecting*, 2:85–127, 1954.

D. Hammami and F. Marillier. AVO analysis for the study of lacustrine sediments, in Lake Geneva, Switzerland. In L. Sambuelli and M.J. Tokarev, editors, *High Resolution Geophysics for Shallow Water*, 69th EAGE Conference and Exhibition. EAGE, 2007.

M. A. Hampton, H. J. Lee, and J. Locat. Submarine landslides. *Reviews of Geophysics*, 34:33–59, 1996.

J.-P. Henriet, M. Verschuren, and W. Versteeg. Very high resolution 3D seismic reflection imaging of small–scale structural deformation. *First Break*, 10(3):81–88, 1992.

F. J. Hilterman. Three-dimensional seismic modeling. *Geophysics*, 35 (6):1020–1037, 1970.

F. J. Hilterman. Amplitudes of seismic waves – A quick look. *Geophysics*, 40(5):745–762, October 1975.

K. Hindriks and A. J. W. Duijndam. Reconstruction of 3-D seismic signals irregularly sampled along two spatial coordinates. *Geophysics*, 65(1):253–263, 2000.

R. W. Hobbs, B. J. Drummond, and B. R. Goleby. The effects of three-dimensional structure on two-dimensional images of crustal seismic sections and on the interpretation of shear zone morphology. *Geophys. J. Int.*, 164:490–500, 2006.

R.W. Hobbs. 3-D modelling of of seismic wave propagation using complex elastic screens with application to mineral exploration. In *Hardrock Seismic Exploration*, pages 59–69. Tulsa: SEG, 2003.

P. Hubral. Time Migration – Some Ray Theoretical Aspects. *Geophysical Prospecting*, 25:738–345, 1977.

J. Jouzel, V. Masson-Delmotte, O. Cattani, G. Dreyfus, S.Falourd, G. Hoffmann, B. Minster, J. Nouet, J. M. Barnola, J. Chappellaz, H. Fischer, J. C. Gallet, S. Johnsen M. Leuenberger, L. Loulergue, D. Luethi, H. Oerter, F. Parrenin, G. Raisbeck, D. Raynaud, A. Schilt, J. S. Schwander, E. Selmo, R. Souchez, R. Spakni, B. Stauffer, J. P. Steffensen, B. Stenni, T. F. Stocker, J. L. Tison, M. Werner, and E. W. Wolff. Orbital and Millennial Antarctic Climate Variability over the Past 800,000 Years. *Science*, 307:793–796, 2007.

D. R. Judson, P. S. Schultz, and J. W. C. Sherwood. Equalizing the stacking velocities of dipping events via Devilish. In *48th Annual International Meeting Socety Exploration Geophysics*, 1978.

D. R. Judson, J. Lin, P. S. Schultz, and J. W. C. Sherwood. Depth migration after stack. *Geophysics*, 45(3):361–375, 1980.

J. C. Kao. Multitasked Computations of 3-D Prestack Kirchhoff Time Migration of the Cray Y-MP C90. *SEG Expanded Abstracts*, 11: 311–313, 1992.

K. R. Kelly, R. W. Ward, S. Trietel, and R. M. Alford. Synthetic Seismograms: A Finite-Difference Approach. *Geophysics*, 41(1): 2–27, 1976.

D. W. Lea, D. K. Pak, , L. K. Peterson, and K. A. Hughen. Temperatures over the Last Glacial TerminationSynchroneity of Tropical and High-Latitude Atlantic. *Science*, 301:1361–1364, 2003.

F. K. Levin. Apparent velocity from dipping interface reflections. *Geophysics*, 36:510–516, 1971.

H. Loseth, L. Wensaas, B. Arntsen, N. Hanken, C. Basire, and K. Graue. 100m long gas blow-out pipes. In *63rd EAGE Conference and Exhibition Extended Abstracts*, page P524. EAGE, 2001.

A.E.H. Love. *Some Problems of Geodynamics*. Cambridge University Press, 1927.

J. J. Lowe, S. O. Rasmussen, S. Bjorck, W. Z. Hoek, J. P. Steffensen, M. J. C. Walker, and Z. C. Yu. Synchronisation of palaeoenvironmental events in the North Atlantic region during the Last Termination: a revised protocol recommended by the INTIMATE group. *Quaternary Science Reviews*, 27(1-2):6–17, 2008.

D. Lumley and B. L. Biondi. Kirchhoff 3-D prestack time migration on the Connection Machine. *Stanford Exploration Project*, 72:125–136, 1991.

D.E. Lumley, J. Claerbout, and D. Bevc. Anti-aliased Kirchhoff 3-D migration. In *64th Annual International Meeting, SEG, Expanded Abstracts*, pages 1282–1285, 1994.

F . J. H. Mackereth. On the variation in direction of the horizontal component of remnant magnetisation in lake sediments. *Earth and Planetary Science Letters*, 12:332–338, 1971.

R. Mallet. On the dynamics of earthquakes: being an attempt to reduce their observed phenomena to the known laws of wave motion in solids and fluids. *Trans. Roy. Irish Acad.*, 21:50–106, 1848.

R. Mallet. Second report on the facts of earthquake phenomena. *BAAS*, 21:272–320, 1851.

R. Mallet and J.W. Mallet. Fourth Report upon the Facts and Theory of Earthquake Phenomena. In *Report of the twenty-eigth meeting of the British Association for the Advancement of Science*, September 1859.

B. Marsset. VHR3D: Very high-resolution marine 3D seismic method for detailed site investigations. Technical report, IFREMER, 2000.

B. Marsset, T. Missiaen, Y.-H. De Roeck, M. Noble, W. Versteeg, and J.-P. Henriet. Very high resolution 3D marine seismic data processing for geotechnical applications. *Geophysical Prospecting*, 46:105–120, 1998.

O. J. Martinsen and B. Bakken. Extensional and compressional zones in slumps and slides in the Namurian of County Clare, Ireland. *Journal of the Geological Society of London*, 147:153–164, 1990.

W.H. Mayne. Common Reflection Point Horizontal Data Stacking Techniques. *Geophysics*, 27(6):927–938, 1962.

D. A. McDougall. The geomorphological impact of Loch Lomond (Younger Dryas) Stadial plateau icefields in the central Lake District, northwest England. *Journal of Quaternary Science*, 16(6): 531–543, 2001.

A. Micallef. *Failure processes in submarine landslides: A geomorphological approach.* PhD thesis, University of Southampon, School of Ocean and Earth Sciences, European Way, Southampton, SO14 3ZH, July 2007.

T. Missiaen. VHR marine 3D seismics for shallow water investigations: Some practical guidelines. *Marine Geophysical Researches*, 26:145–155, 2005.

T. Missiaen, W. Versteeg, and J.-P. Henriet. A new 3D seismic acquisition system for very high and ultra high resolution shallow water studies. *First Break*, 20(4):227–232, 2002.

K. Monecke, F. S. Anselmetti, A. Becker, M. Schnellmann, M. Sturm, and D. Giardini. Eatherquake-induced deformation structures in lake deposits: A late Pleistocene to Holocene paleoseismic record for central Switzerland. *Eclogae Geologicae Helvetiae*, 99(3):343–362, 2006.

P. M. Morse and H. Feshback. *Methods of theoretical physics, Parts I and II.* New York, McGraw–Hill Book co, Inc., 1953.

T. Mulder and P. Cochonat. Classification of Offshore Mass Movements. *J. Sedimentary Research*, 66(1):43–57, 1996.

W. A. Mulder and R.-E. Plessix. One-way and two-way wave equation migration. In *73rd Annual International Meeting, SEG, Expanded Abstracts*, pages 881–884, 2003.

C. Muller, B. Mikereit, T. Bohlen, and F. Theilen. Towards high-resolution 3D marine seismic surveying using Boomer sources. *Geophysical Prospecting*, 50:517–526, 2002.

C. Muller, S. Woelz, Y. Ersoy, G. Wendt, and W. Rabbel. UHR Marine 3D Seismic Investigation of the Limantepe/Caratina Island Archaeological Sites (Urla/Turkey). In L. Sambuelli and M.J. Tokarev, editors, *High Resolution Geophysics for Shallow Water*, 69th EAGE Conference and Exhibition. EAGE, 2007.

T. Nemeth, C. Wu, and G. T. Schuster. Least-squares migration of incomplete reflection data. *Geophysics*, 64(1):208–221, 1999.

T. Padhi and T.K. Holley. Wide azimuths - why not? *The Leading Edge*, 1997.

W. Pennington. Lake Sediments: The Bottom Deposits of the North Basin of Windermere, with Special Reference to the Diatom Succession. *New Phytologist*, 42(1):1–27, 1943.

W. Pennington. Climatic changes in Britain, as interpreted from lake sediments, between 15,000 and 10,000 years ago. In S. Horie, editor, *Paleolimnology of Lake Biwa and the Japanese Pleistocene*, volume 3, pages 536–569. Otsu, Japan, 1975.

W. Pennington. The origin of pollen in lake sediments: An enclosed lake compared with one receiving inflow streams. *New Phytologist*, 83:189–213, 1978.

W. Pennington. Palaeolimnology in the English Lakes - some questions and answers over fifty years. *Hydrobiologia*, 214:9–24, 1991.

C. Pierce, M. Sinha, S. Topping, and C. Gill. Morphology and genesis of slow-spreading ridges - seabed scattering and seismic imaging within the oceanic crust. *Geophys. J. Int.*, 168(1):59–89, 2007.

L. J. W. Pinson. *Remote Classification of Sediment Properties using High-Resolution Marine Seismic Data*. PhD thesis, School of Ocean and Earth Science, National Oceanography Centre, Southampton, 2009.

L. J. W. Pinson, T. J. Henstock, J. Dix, and J. M. Bull. Estimating quality factor and mean grain size of sediments from high-resolution marine seismic data. *Geophysics*, 73(4):G19–G28, 2008.

S. Planke, P. Symonds, E. Alvestad, and J. Skogseid. Seismic volcanostratigraphy of large-volume basaltic extrusive complexes on rifted margins. *J. Geophys. Res.*, 105:19335–19351, 2000.

R.M.K. Plets. *Acoustic Imaging, Reconstruction, and Characterization of Buried Archaeological Material*. PhD thesis, School of Ocean and Earth Science, National Oceanography Centre, Southampton, 2007.

R.M.K. Plets, J.K. Dix, J.R. Adams, and A.I. Best. 3D Reconstruction of a Shallow Archaeological Site from High-Resolution Acoustic Imagery: the Grace Dieu. *Applied Acoustics*, In Press, 2007.

R. Quinn. *Marine high-resolution reflection seismology: acquisition, processing, and applications*. PhD thesis, School of Ocean and Earth Science, National Oceanography Centre, Southampton, 1997.

R. Quinn, J. M. Bull, and J. Dix. Imaging Wooden Artefacts using Chirp Sources. *Archaeological Prospection*, 4:25–35, 1997a.

R. Quinn, J. M. Bull, and J. Dix. The Mary rose site - geophysical evidence for paleo-scour marks. *The International Journal of Nautical Archaeology*, 26(1):3–16, 1997b.

R. Quinn, J. M. Bull, and J. Dix. Optimal Processing of Marine High–Resolution Seismic Reflection (Chirp) Data. *Marine Geophysical Researches*, 20:13–20, 1998.

R. Quinn, W. Forsythe, C. Breen, M. Dean, M. Lawrence, and S. Liscoe. Comparison of the Maritime Sites and Monuments Record with Side-Scan Sonar and Diver Surveys: A Case Study from Rathlin Island, Ireland. *Geoarchaeology: An International Journal*, 17(5): 441–451, 2002.

Lord. Rayleigh. On waves propagated along the plane surface of an elastic solid. *Proc. London. Math. Soc.*, 17:4–11, 1885.

E.A. Robinson and T.S. Durrani. *Geophysical Signal Processing*. Prentice/Hall International, London, UK, 1986.

I. S. Robinson. *Measuring the Oceans from Space*. Springer, London, UK, 2003.

A. Rochon, A. de Vernal, H.-P. Sejrup, and H. Haflidason. Palynological Evidence of Climatic and Oceanographic Changes in the North Sea during the Last Deglaciation. *Quaternary Research*, 49: 197–207, 1998.

J. Ronen. Wave equation trace interpolation. *Geophysics*, 52:1166–1177, 1987.

M.G. Rowan, B.S. Hart, S. Nelson, P.B. Flemmings, and B.D. Trudgill. Three-dimensional geometry and evolution of a salt-related growth-fault array. *Mar. Petrol. Geol.*, 15:309–328, 1998.

M Scheidhauer, D. Dupuy, F. Marillier, and M. Beres. Development of a 3D VHR seismic reflection system for lacustrine settings - A case study in Lake Geneva, Switzerland. *Geophysical Research Abstracts*, 5:14022, 2003.

M. Scheidhauer, F. Marillier, and P. Thierry. Detailed 3D seismic imaging of a fault zone beneath Lake Geneva, Switzerland. *Basin Research*, 17:155–169, 2005.

W. A. Schneider. Integral formulation for the migration in two and three dimensions. *Geophysics*, 43(1):49–76, February 1978.

W.A. Schneider. 3-D Seismic: A historical note. *The Leading Edge*, Nov. 1998.

W.A. Schneider. 3-D Seismic: A historical note. In R.J. Graebner, R.A. Hardage, and W.A. Schneider, editors, *3-D Seismic Exploration*, volume 22 of *Geophysical Reprint Series*, chapter 1, pages 69–74. SEG, 2001.

M. Schnellmann, F. S. Anselmetti, D. Giardini, J. A. McKenzie, and S. N. Ward. Prehistoric earthquake history revealed by lacustrine slump depostis. *Geology*, 30(12):1131–1134, December 2002.

M. Schnellmann, F. S. Anselmetti, D. Giardini, and J. A. McKenzie. Mass movement-induced fold- and thrust-belt structures in unconsolidated sediments in Lake Lucerne (Switzerland). *Sedimentology*, 52(271-289), 2005.

M. Schnellmann, F. S. Anselmetti, D. Giardini, and J. A. McKenzie. 15,000 Years of mass-movement history in Lake Lucerne: Implications for seismic and tsunami hazards. *Eclogae Geologicae Helvetiae*, 99(3):409–428, 2006.

S.G. Schock and L.R. LeBlanc. Chirp Sonar: New Technology For Sub-Bottom Profiling. *Sea Technology*, 31(9):35–43, 1990.

S.G. Schock and J. Wulf. Buried Object Scanning Sonar for AUVs. In *MTS/IEEE Oceans Conference*, 2003.

S.G. Schock, L.R. LeBlanc, and L.A. Mayer. Chirp subbottom profiler for quantitative sediment analysis. *Geophysics*, 54(4):445–450, 1989.

S.G. Schock, A. Tellier, J. Wulf, J. Sara, and M. Ericksen. Buried object scanning sonar. *IEEE Journal of Ocean Engineering*, 26(4): 677–689, 2001.

S.G. Schock, J. Wulf, G. Quentin, and J. Sara. Synthetic Aperture Processing of Buried Object Scanning Sonar Data. In *Proceedings IEEE Oceans 2005*, 2005.

P. S. Schultz and J. W. C. Sherwood. Depth migration before stack. *Geophysics*, 45(3):376–393, 1980.

C.E. Shannon. *The Mathematical Theory of Communication*. University of Illinois Press, Urbana, USA, 1948.

R.E. Sheriff. *A First Course in Geophysical Exploration and Interpretation*, page 313. International Human Resources Development Corp., Boston, 1978.

R.E. Sheriff. Processing and Interpretation of Seismic Reflection Data: An Historical Precis. *The Leading Edge*, 7(1):40–42, January 1988.

J. E. Simms and P. E. Albertson. Multidisciplined Investigation to Locate the Kentucky Shipwreck. *Geoarchaeology: An International Journal*, 15(5):441–468, 2000.

J. Simons, R. Biswas, S. Shah, K. Hotta, and R. Achambault. OpenMP, 2008. URL `http://openmp.org/wp/`.

L. Sirgue and R. G. Pratt. Efficient waveform inversion and imaging: A strategy for selecting temporal frequencies. *Geophysics*, 69(1): 231–248, 2004.

J. B. Sissons. Palaeoclimatic inferences from former glaciers in Scotland and the Lake District. *Nature*, 278:518–520, 1979.

A. J. Smith. Structures in the stratified late-glacial clays of Windermere, England. *Journal of Sedimentary Petrology*, 29:447–453, 1959.

U. Spagnolini and S. Opreni. 3-D Shot continuation operator. *SEG Expanded Abstracts*, 15:439–442, 1996.

S. Spitz. Seismic trace interpolation in the F–X domain. *Geophysics*, 56(6):785–791, 1991.

R. H. Stolt. Migration by Fourier Transform. *Geophysics*, 43(1):23–48, 1978.

R. Stoneley. Elastic waves at the surface of separation of two solids. *Proc. Roy. Soc.*, A-106:416–428, 1924.

M. T. Taner and F. Koeler. Velocity spectra – Digital computer derivation and applications of velocity functions. *Geophysics*, 34: 859–881, 1969.

D. R. Tappin, L. C. McNeill, T. J. Henstock, and D. Mosher. Mass wasting processes - offshore Sumatra. In V. Lykousis, D. Sakellariou, and J. Locat, editors, *Submarine mass movements and their consequences:3rd International Synposium*, volume 27 of *Advances in Natural and Technological Hazards*, pages 327–336. Springer, Dordrecht, Netherlands, 2007.

Thales Navigation. *Ashtech Sagitta Series: User Manual*. Thales Navigation, Santa Clara, USA, July 2002.

D. J. Thompson and N. R. Chapman. A wide-angle split-step algorithm for the parabolic equation. *J. Acoustic. Soc. Amer.*, 74: 1848–1854, 1983.

J. R. Thorson and J. Claerbout. Velocity-stack and slant-stack inversion. *Geophysics*, 50(12):2727–2741, 1985.

A. W. Trorey. A simple theory for seismic diffractions. *Geophysics*, 35(5):762–784, October 1970.

J. van Trier and W. W. Symes. Upwind finite–difference calculation of travel times. *Geophysics*, 56:812–821, 1991.

M.E. Vardy, J.K. Dix, T.J. Henstock, J.M. Bull, and M. Gutowski. Decimetre-Resolution 3D Seismic Volume in Shallow Water; A Case Sudy in Small Object Detection. *Geophysics*, 73(2):B33–B40, 2008.

Červeny and Pšenčík. Gaussian beam and paraxial ray approximation in three–dimensional inhomogeneous media. *Bulletin of the Seismological Society of America*, 70:47–77, 1983.

N.H. Verbeek and T.M. McGee. Characteristics of high-resolution marine reflection profiling sources. *Journal of Applied Geophysics*, 33:251–269, 1995.

G.J.O. Vermeer. *Seismic Wavefield Sampling*. SEG, 1990.

G.J.O. Vermeer. *3–D Seismic Survey Design*. Number 12 in Geophysical Reference Series. SEG, 2002.

W. Versteeg, M. Verschuren, J.-P. Henriet, and M. De Batist. High-resolution 3D and pseudo-3D seismic investigations in shallow water envionments. In M. Weydert, editor, *European Conference in Underwater Accoustics*, pages 497–500, 1992.

N. Wardell, P. Diviacco, and R. Sinceri. 3D pre-processing techniques for marine VHR seismic data. *First Break*, 20(7), 2002.

N. D. Whitmore. Iterative depth migration by backward time propagation. *53rd Annual International Meeting, Society of Exploration Geophysicists, Expanded Abstracts*, pages 382–385, 1983.

M. B. Widess. How Thin is a Thin Bed? *Geophysics*, 6:1176–1180, 1973.

N. Wiener. *Extrapolation, Interpolation, and Smoothing of Stationary Time Series*. Technology Press of MIT and John Wiley & Sons, New York, USA, 1950.

J. W. Wiggins. Kirchhoff integral extrapolation and migration of nonplanar data. *Geophysics*, 49(8):1239–1248, 1984.

A. J. Wild and J. A. Hudson. A geometrical approach to the elastic complex screen. *Journal of Geophysical Research*, 103(B1):707–725, January 1998.

A.J. Wild, R.W. Hobbs, and L. Frenje. Modelling complex media: an introduction to the phase-screen method. *Earth and Planetary Science Letters*, 120:219–225, 2000.

C. D. V. Wilson. The outflow of Windermere, Cumbria: a re-appraisal. *Geological Journal*, 22:219–224, 1987.

R.-S. Wu. Wide-angle elastic wave one-way propagation in heterogeneous media and an elastic wave complex-screen method. *J. Geophys. Res.*, 99:751–766, 1994.

O. Yilmaz. *Seismic Data Processing*, volume 2 of *Investigations in Geophysics*. SEG, Tulsa, USA, 1 edition, 1987.

Y. Zhang and J. Sun. Practical issues in revese time migration: True amplitude gathers, noise removal and harmonic source encoding. *First Break*, 27(1):53–59, 2009.

Y. Zhang, J. Sun, S. H. Gray, and J. Young. Delayed-shot 3-D prestack depth migration. *Geophysics*, 70(1):E21–E28, 2005.

"The sciences do not try to explain, they hardly ever try to interpret, they mainly make models."

John von Neumann (1903–1957)

A

Phase Screen 3D Forward Modelling

In this Appendix I introduce the phase screen approach to generating synthetic 3D seismic volumes. The appropriateness of this method for simulating 3D Chirp data is discussed. Following this, I develop the synthetic model of a sinusoidal reflector used in Chapter 4 for assessing the effect of large spatial discontinuities on the effectiveness of a series of pre– and post–stack migration algorithms.

A.1 The Phase Screen Method

Traditional finite difference approaches to forward modelling divide the subsurface into nx, ny, nz, cells of size dx, dy, dz, through which downgoing and upgoing wavefields are propagated (e.g., Kelly et al., 1976). With a good approximation of the wave equation, these techniques provide accurate synthetic seismic volumes within the resolu-

tion limits of the cell dimensions. They are also simple to code, and readily provide true amplitudes, as well as accommodating diffracting events, turning rays, phase changes, surface waves and multiples. However, the computational cost of this approach is high, particularly for the 3–dimensional case.

An alternative, that has been used extensively for atmospheric (e.g., Buckley, 1975) and oceanic (e.g., Thompson and Chapman, 1983) modelling, is the phase screen method. For this approach, the model medium is simplified down to a series of diffracting screens, with a homogeneous medium in between (Wild and Hudson, 1998). In this manner, propagation of the wavefields between screens can be done using the plane wave approximation of Claerbout (1970) as long as each frequency component is passed through the model independently. Propagation between phase screen j and $j+1$ in the Fourier–domain is therefore accomplished by multiplication with a propagation function, Equation 4.14.

Since, for the seismic wavefield case, there is a need to include non–vertically propagating plane waves (e.g., diffractions) between screens, the propagation function must account for the transverse component of the wavefield. Therefore, propagation between screens is performed using the equation:

$$U_{j+1}(k_x, k_y, z_{j+1}, \omega) = e^{i\sqrt{k^2+k_T^2}\Delta z} P_j(k_x, k_y, z_j, \omega); \qquad \text{(A.1)}$$

where k is the magnitude of the total wave vector, and k_T the magnitude of the transverse wave vector (Wild and Hudson, 1998).

This wavefield, $U_{j+1}(k_x, k_y, z_{j+1}, \omega)$, is the wavefield incident upon screen $j+1$, while $P_j(k_x, k_y, z_j, \omega)$ is the wavefield transmitted by screen j. The relationship between the wavefield incident upon a screen and that transmitted by it is, in the spatial–domain, a function of the incident wavefield and a phase screen function. For screen j, this screen function, $J_j(x, y)$, is dependant upon the known distribution of

heterogeneities across the screen. Equation A.1 is, therefore, rewritten as:

$$U_{j+1}(k_x, k_y, z_{j+1}, \omega) = e^{i\sqrt{k^2+k_T^2}\Delta z} \times \mathfrak{F}\left[J_j(x,y)u_j(x,y,z_j,\omega)\right]; \quad \text{(A.2)}$$

where $\mathfrak{F}$ denotes the Fourier transform.

For elastic waves propagating through the Earth's subsurface, the screen function is complex as it must account for P– to S–wave conversions (Wu, 1994). The single screen function above becomes a set of four functions that cover P–waves, S–waves, and conversions between the two:

$$J_j^{PP}(x,y), \quad J_j^{SS}(x,y), \quad J_j^{PS}(x,y), \quad J_j^{SP}(x,y). \qquad \text{(A.3)}$$

This also leads to two waves being propagated between screen j and $j+1$, meaning that Equation A.1 becomes a pair of equations (see, Wild and Hudson, 1998). To generate synthetic 3D Chirp volumes we are only interested in P–waves, so it is only necessary to consider the P–wave equation, along with the J_j^{PP} screen function.

$$\begin{aligned} U_{j+1}^P(k_x, k_y, z_{j+1}, \omega) &= e^{i\sqrt{k^2+k_T^2}\Delta z} \\ &\quad \times \mathfrak{F}\left[J_j^{PP}(x,y)u_j^P(x,y,z_j,\omega)\right]. \quad \text{(A.4)} \end{aligned}$$

Equation A.4 describes the model as the propagation of a wavefield through the model volume from one screen to the next; $j-1$ to j to $j+1$, etc. However, to model the passage of a seismic wavefield through the Earth's subsurface, the screen function $J_j^{PP}(x,y)$ which governs interaction between the wavefield $u_j^P(x,y,z_j,\omega)$ and screen j has to be thought of in two parts: the transmitted component, $J_{j,trans}^{PP}(x,y)$; and the reflected component, $J_{j,ref}^{PP}(x,y)$.

Since the medium between the screens is homogeneous, the model space can be thought of as a series of thin lenses as long as we are only interested in near–normal incident reflections (Wild et al., 2000).

A first–order approximation for P–waves, as derived by Wild and Hudson (1998), takes the form:

$$J^{PP}_{j,trans}(x,y) = e^{ik_\alpha \Delta z \frac{\delta\alpha}{\alpha_0}}; \tag{A.5}$$

Similarly, the reflected component can be calculated from the first–order (small angle) approximations of the Zoeppritz formulae. Wild and Hudson (1998) show that for P–waves, the reflected part of the wavefield is given by the function:

$$J^{PP}_{j,ref}(x,y) = \frac{1}{2}\left(\frac{\delta\rho}{\delta\rho_0} + \frac{\delta\alpha}{\alpha_0}\right); \tag{A.6}$$

where ρ is density.

This leads to the interaction between a wavefield and screen j being described by a pair of equations that describe the energy transmitted through to become incident upon screen $j+1$ and the energy reflected to screen $j-1$.

$$\begin{aligned} U^P_{j+1}(k_x,k_y,z_{j+1},\omega) &= e^{i\sqrt{k^2+k_T^2}\Delta z}\hat{\mathbf{k}}_\alpha\hat{\mathbf{k}}_\alpha \\ &\quad \times\mathfrak{F}\left[e^{ik_\alpha\Delta z\frac{\delta\alpha}{\alpha_0}}u^P_j(x,y,z_j,\omega)\right], \\ U^P_{j-1}(k_x,k_y,z_{j-1},\omega) &= e^{i\sqrt{k^2+k_T^2}\Delta z}\hat{\mathbf{k}}_\alpha\hat{\mathbf{k}}_\alpha \\ &\quad \times\mathfrak{F}\left[\frac{1}{2}\left(\frac{\delta\rho}{\delta\rho_0}+\frac{\delta\alpha}{\alpha_0}\right)u^P_j(x,y,z_j,\omega)\right]. \end{aligned} \tag{A.7}$$

The pair of equations given in Equation Array A.7 can be used to model the interaction between a wavefield and diffracting screen. Resulting in transmitted and reflected wavefields, which can then be used to model the further propagation of the original wavefield.

The speed advantage of this method emerges because, to propagate the wavefield through a phase screen model, the Equation Array A.7 requires solving for each node on each screen. Under a finite difference regime, an equivalent set of wave propagation equations require

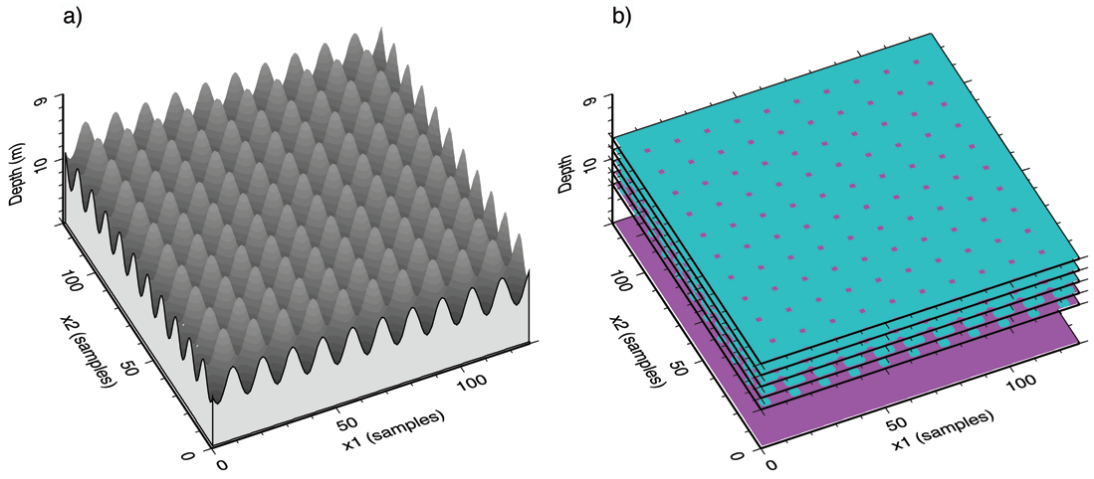

Figure A.1: Figure showing a map of the sinusoidal interface used for migration simulations, panel a), together with horizontally sliced screens through the velocity model, panel b). Here screens are sliced at 0.2 m intervals from 9.6 m to 10.4 m to indicate changing structure. For modelling, the velocity field was sliced at 0.1 m intervals from 9.3 m to 10.8 m.

solving for each nx, ny, nz cells. This has a particular advantage for marine data, where as much as a third of the model space is composed of the homogeneous water layer. In this manner, the careful positioning of screens only in regions of interest, vast speed improvements can be gained.

A.2 Decimetre–Scale Application

The phase screen code of Wild and Hudson (1998) has been used for a variety of crustal–scale application: P– and S–wave returns from massive sulphide ore–bodies (Hobbs, 2003; Bohlen et al., 2003); the modelling of out–of–plane effects on 2D MCS data (Drummond et al., 2004; Hobbs et al., 2006); and the seismic morphology of oceanic ridges (Pierce et al., 2007). These applications, however, are on a completely different scale from 3–D Chirp. Profiles/volumes are several km or 10s km in length, and reflections are recorded to several

seconds TWT. The source wavelets used for wavefield $u_0^P(x, y, z_0, \omega)$ have a central frequency in the range 1 Hz to 50 Hz, and therefore allow a vertical resolution of 50 m to 100 m. As discussed further in **Chapter 2**, seismic volumes acquired using 3D Chirp are never more than two or three hundred metres in extent (**Chapters 3** and **6**), have a maximum recording time of c. 100 ms for geologically interesting targets (see, **Chapter 6**), and centimetric vertical resolution afforded by the 1.5 kHz to 13.0 kHz source frequency (see, **Chapter 3**).

In generating synthetic volumes on this scale there was no problem with decreasing the horizontal sampling intervals to the 12.5 cm suitable for 3D Chirp simulation, but rounding limitations meant that phase screens could not slice through the model closer than 10 cm apart. When constructing a complex reflector, such as the egg–box interface shown in Figure A.1, this means smoothly dipping reflectors become stepped reflectors. For the purposes of **Chapters 4** and **5** this was not a problem, as migrating the reflections such that the response form individual phase screens proved to be a good test of the migration algorithms.